UNIVERSITY OF LIVERPOOL

The Stability of Single Crystal Pt and Pt_3Ni Surfaces During Electro-Oxidation

by

Michael James David Darlington

A thesis submitted in partial fulfillment for the
degree of Doctor of Philosophy

in the
Faculty of Science and Engineering
Department of Physics

September 2014

Declaration

The Cyclic Voltammery, Scanning Tunnelling Microscopy and ICP-MS experiments contained in this thesis were performed by Nenad Markovic's group, our collaborators at the Material Sciences Division of the Argonne National Lab, Chicago. He has kindly allowed use of the data in this thesis.

"Study hard what interests you the most in the most undisciplined, irreverent and original manner possible."

Richard P. Feynman

UNIVERSITY OF LIVERPOOL

Abstract

Faculty of Science and Engineering
Department of Physics

Doctor of Philosophy

by Michael James David Darlington

In an effort to gain a fundamental understanding of the link between catalyst surface structure, reactivity and stability, experiments have been performed on Pt(111), Pt_3Ni(111) and Pt(100) single crystal electrode surfaces via a combination of *in-situ* structural probes and electrochemical (cyclic voltammetry) measurements. Pt(111), which is the least active of the low index surface for the Oxygen Reduction Reaction (ORR), showed morphological changes after oxidation reduction cycles, with the formation of stable platinum adislands. The more active Pt(100) surface undergoes a drastic roughening of the surface during oxidation/reduction cycles, which is due to the fact that the surface is unlikely to recrystallise into the more open (100) surface structure. In essence, although the Pt surfaces with a more open atomic geometry, e.g. (100) and (110), are more reactive than the close-packed (111) surface, they are intrinsically less stable. The bimetallic alloy Pt_3Ni(111) surface has been shown to be over 10 times more active for the ORR than pure Pt(111) and exhibits a compositional oscillation at the surface which is formed of Pure Pt. Upon repetitive cycling the Pt_3Ni(111) surface undergoes a similar morphological change to that of Pt(111), where the formation of adislands was seen in STM measurements. These adislands retain some of the active segregated surface structure, preserving the electronic modification due to the Ni-rich subsurface. This leads to a stable surface that remains more active than the pure Pt(111) electrode after prolonged cycling of the potential into the region of oxidation/reduction. Perhaps the key insight that can be obtained from these experiments is that electrode activity towards the ORR is intrinsically linked to surface stability, i.e. the more active the surface, the less stable it is. This, in fact, may be a general effect in electrocatalysis.

Acknowledgements

First and foremost I'd like to thank my supervisor Chris for all the time, honest advice and beer he has given me over the past few years, without which I would never have finished this thesis. I'd also like to thank Mick and Alex for teaching me how to be a PhD student, and Naomi for not learning how to be a PhD student from me. In all seriousness, I could not have asked for friendlier or harder working colleagues. Next I'd like to thank all the beamline staff who helped with all the experiments I have worked on, especially Paul who worked tirelessly to make sure the they were successful. Thanks must also go to Nenad Markovic for allowing the use of the Cyclic Voltammery, Scanning Tunnelling Microscopy and ICP-MS data.

A special thanks must go to my parents and brother Andy for all the cups of tea and emotional support, especially during the thesis writing stage. I'd like to thank all of my friends for still being my friends now, despite me being a miserable git for the last two years. Especially Lee and Simon for forcing me to have a social life; as well as Emma and my dog Theo, who got me through my first couple of years. Finally I'd like to thank Annette, my girlfriend, for sticking with me and being awesome in every way.

Contents

List of Figures

List of Tables

Chapter 1

Introduction

To develop a real understanding of electrocatalytic reactions occurring at the solid/liquid interface, it is essential to characterise model catalyst surfaces on the atomic scale. Electrocatalytic reactions involve a charge transfer between a dissolved chemical species and the electrode surface; therefore the composition and surface atomic structure have a great impact on the reaction kinetics. Cyclic Voltammetry (CV) is the basic measurement employed in many electrochemical studies of such reactions and involves the measurement of the current as a function of the applied potential across an interface. As CV measures current flow it gives a rich source of information regarding the potential dependence of certain electrochemical reactions. However, there is a lack of structural or chemical sensitivity in electrochemical measurements, which are key to understanding the processes that occur.

Structural or chemical information can be gathered using surface science techniques, which are the study of the interface between two phases, e.g. liquid-solid or vacuum-solid, focusing on the chemical and physical effects taking place. The field of surface science was preceded by the development of the Ultra High Vacuum (UHV) environment in the 1950's. Within UHV, electron probe techniques, such as Low Energy Electron Diffraction (LEED) and X-ray Photoelectron Spectroscopy

(XPS), were utilised *ex-situ* in combination with electrochemical measurements, such as CV, for atomic scale characterisation of electrochemical systems. In the case of an *ex-situ* experiment the sample must be transferred from the liquid environment into UHV following the electrochemical measurement and visa versa. This is not ideal as the surface is exposed to the atmosphere in addition to the absence of potential control during transfer, possibly causing alteration to the surface.

A number of experimental methods can be used to investigate the surface through the liquid overlayer, including optical spectroscopy, scanning probe microscopy and diffraction techniques, all of which are summarised in reference [1]. The primary technique employed in this thesis is surface x-ray diffraction, for a detailed description of this technique see references[2–7]. X-rays are more penetrative than electrons, giving a much higher signal to noise ratio after passing through a given thickness of material. Before *in-situ* Surface X-ray Scattering (SXS) could be employed to study the solid/liquid interface, two important developments had to occur. Firstly, the use of synchrotron radiation as an intense source of x-rays, essential for penetrating the liquid overlayer, had to be realised. Secondly, the development of an *in-situ* x-ray electrochemical cell that operates with a thin layer geometry was required[8]. This cell traps a thin layer of electrolyte overlayer permitting the transmission of x-rays while maintaining the potential control of the interface[9].*In-situ* SXS and CV measurements allow for the correlation of the observed current in CVs with the atomic structure of the electrode surface, under reaction conditions.

Pt single crystal surfaces have been studied in detail using SXS over the past two decades. They began with the study of platinum in alkaline and acidic solution [10] where an expansion of the top monolayer of platinum in the hydrogen dissociation region was seen. This was followed by a study of halide anion adsorption; e.g. Iodide[11][12], bromide[13][14][12] and chloride [12].

Metal deposition on platinum was studied as thin metal films change the chemical and electronic properties of the surface. Initial studies of metal deposition focussed on the interplay between the metal cations and the anions present in the supporting electrolyte in terms of cooperative and competitive adsorption phenomena. For example, lead Under Potential Deposition (UPD) on Pt(100) (in the presence of bromide) was modified; the surface coverage of Pb decreased from 0.62 monolayers to approximately one half of a monolayer, in addition to shifting the formation of this layer to a more negative potential [15] with the Pb forming a strongly bonded c(2 x 2) adlayer[16]. In the case of Pt(111) a similar competitive process occurs, where the surface coverage of Pb decreases from 0.63 to 0.51 monolayers[17]. This decrease stops the formation of a close-packed monolayer; however in the potential region where the ratio of co-adsorbed metal and anion species is close to one a slow formation of an ordered surface alloy was seen with a (2 x 2) unit cell[17].

Another metal UPD and halide system which has been studied is copper on platinum in the presence of halide anions. In this case Br^- is displaced from adsorption sites by Cu during UPD, forming a Cu-Br bilayer. For Pt(100) the strong Pt-Br interaction broadens the potential region of the Cu UPD[18] and Br forms an ordered c(2 x 2) structure on a p(1 x 1) pseudomorphic layer of copper[19]. Cu UPD on Pt(111) in the presence of Br is slightly different than the Pt(100) system in that it occurs in two steps where the Cu and Br undergo a turnover process [16][20]. During the transition to the intermediate stage the Cu exchanges places with the Br initially on the surface, until the coverage of both Cu and Br are approximately 0.5 of a monolayer in an ordered structure with an incommensurate hexagonal unit cell. In the final stage of UPD the copper plane is completed as a pseudomorphic (1 x 1) Cu monolayer and the Br remains on the surface as a disordered adlayer with a coverage of 0.4 monolayers[16][20]. A similar process has also been observed in a solution where Cl is present [21][22][23]. Like halides (bi)sulphate anions also modify the liquid-solid interface, altering the UPD of copper into a two step process, where initially a single monolayer of copper is deposited into the surface preceded by the formation of a ($\sqrt{3}$ x $\sqrt{3}$) R30^o structure consisting of both copper and (bi)sulphate anions[24]. It can clearly be seen that UPD of metal onto Pt(111) and Pt(100) can lead to a variety of structural effects[25][26].

In tandem to the study of metal UPD, irreversibly adsorbed metals where also studied. As the surface metals are irreversibly adsorbed, a range of potential dependent surface reactions could be studied without stripping the metal deposit. Measurements of an electro deposited Pd film with a coverage of 1 ML on Pt(111) have shown that the rate of the hydrogen evolution/oxidation reactions are much faster on the Pt(111)-Pd system than Pt(111) [27]. In addition, it was found that the expansion of the surface caused by the hydrogen bonding seen in the Pt(111) system was greatly reduced in the Pt(111)-Pd system; this is likely caused by strong bonding between the Pd and Pt atoms [27]. The deposition of thicker Pd films onto Pt(111) exhibited a Stranski-Krastanov growth mode, i.e. where island growth begins after the initial monolayer is formed [28]. In the case of Pt(001)-Pd, a similar Stranski-Krastanov growth was observed, with island growth beginning once the first Pd layer had reached an occupation of 0.8 ML. CO adsorption on this surface causes surface normal expansion and in-plane distortion of the Pd lattice in the hydrogen evolution region, and it was proposed that this was due to the enhanced adsorption of hydrogen[29]. On Pt(111), the CO can be removed from the surface by oxidation and the resulting surface oxide is incommensurate with the Pt lattice. The surface oxidation is fully reversible[30]. Bismuth deposition on platinum was then studied, where Bi adsorbs onto the Pt surface without an overpotential. On the Pt(111) surface irriversible Bi adsorption (Bi_{ir}) continues to a coverage of approximately one third of a monolayer, with no discernible long range structure, and is stable over a wide potential range [31]. The Bi_{ir} changes the electronic structure of the surface, causing the nearby platinum atoms to have a positive charge. This decreases the number of sites on the surface which are available for dissociative adsorption of H_2. Furthermore, the chemisorption of CO displaces the bismuth layer [31].

One of the greatest advantages of *in-situ* techniques is the ability to relate microscopic details, such as surface structure, with macroscopic measurements, for example kinetic rates of reactions. For the case of CO adsorption onto Pt(111) it was possible to measure the adsorbate structure directly as CO formed a compact p(2 x 2)-3CO structure at negative potentials [32]. On oxidation of the CO a remarkable difference between alkaline and acidic solutions was seen, where oxidation occurred at a much lower potential in alkaline solution [33]. On the other hand, acidic solutions containing Br^- dramatically increased the stability and domain size of the p(2 x 2)-3CO structure[33]. The discovery of this link between domain size and stability was made possible by *in-situ* SXS and similar experiments performed on various low index platinum surfaces[34][35][36][37]. More recently, the effects of temperature have also been studied, which is important due to many relevant electrochemical processes occurring at non-ambient temperatures in practical applications [38]. In the specific case of CO adsorption on Pt(111) a strong temperature effect was observed on the ordering in the CO adlayer, indicating a change in the kinetics of oxide formation, water activation and adsorption of the oxygenated species[38].

Bifunctional effects in electrolyte were explored by studying Pt based binary alloys. For example research on UHV prepared Pt_3Sn(111) showed a p(2 x 2) alloy surface which was stable on transfer to a sulphuric acid electrolyte as well as during subsequent potential cycling [39]. As with Pt(111) the alloy undergoes a surface expansion, in this case 2%, in the reversible hydrogen region. Above 0.55 V vs. RHE (Reversible Hydrogen Electrode) the Sn buckles with a 6% expansion which precedes the Sn dissolution at 1.0 V[39]. The results indicated that Pt_3Sn could be a candidate for a CO-tolerant catalyst material due to the onset potential for CO oxidation. In particular it may be suitable as the anode catalyst in a Polymer Electrolyte Membrane Fuel Cell (PEMFC), a device that converts the chemical energy of hydrogen and oxygen directly into electrical energy. The PEMFC can be described by focusing on its three main components, the anode, the polymer electrolyte membrane and the cathode. During operation hydrogen gas is introduced to the anode catalyst, upon which the hydrogen molecules are dissociated and split into protons and electrons. The protons then permeate through the polymer electrolyte membrane while the electrons pass through an external circuit, creating the current output. The protons and electrons arrive at the cathode, at which point they react catalytically with a stream of oxygen gas. The reaction at the cathode is known as the Oxygen Reduction Reaction (ORR) (defined as the difference between the measured electrode potential, E, and the reversible potential for the reaction $O_2 + 4H^+ + 4e^- = H_2O$; E = 1.23 V).

Many problems still need to be resolved in order for a PEMFC to fully reach its commercial implementation, such as in automotive propulsion. Although early attention focussed on the anode catalyst (for example in the search for CO-tolerant catalysts, such as Pt_3Sn) one of the major hindrances to full commercialisation is the sluggish kinetics of the ORR on the cathode side of the fuel cell. The key difficulty is the development of materials that are simultaneously able to reduce the significant overpotential for the OOR and provide long-term stability of the catalyst material in the hostile electrochemical environment. A very large number of materials have been tested for the ORR in acidic media, including noble metals, metal alloys and even non-precious metal catalysts. At present, the most active catalyst is a $Pt_3Ni(111)$ single crystal, being 3-5 times more active than the two other $Pt_3Ni(hkl)$ low-index single crystal surfaces; 10-times more active than the corresponding Pt(111) surface and 90-fold more active than state-of-the-art Pt/C catalysts. It is remarkable that the $Pt_3Ni(111)$ surface is so much more active than $Pt_3Ni(110)$ in perchloric acid solution (the electrolyte that most closely mimics the PEM environment), given that in the same solution it is well established that Pt(110) is slightly more active than Pt(111). Understanding the origin of the differences in surface activity is one important step towards the design of real nanoparticle catalysts for the ORR that combine both high activity and long term stability. The second consideration concerns the stability of the nanosegregated composition profile at potentials above 1V, a potential excursion that often occurs under PEM operating conditions.

Given that catalyst stability is an integral part of any materials design process, establishing the potential window of stability of nanosegregated structures is a major challenge. This requires an understanding of the interplay between oxide-induced changes in surface morphology and activity for the ORR. A typical probe of bimetallic cathode catalyst stability is to take a nanoparticle high surface area catalyst and subject it to extensive potential cycling (up to 20000 cycles!) deep into the region of oxide formation and monitor the deactivation in catalyst reactivity, typically assigned to dealloying of the non-noble metal component. Based on this experimental approach, however, it is impossible to derive a fundamental understanding of the mechanism of surface dealloying, yet this is crucial for catalyst design. One way to overcome this is to utilise a surface science approach. Such an approach is described in this thesis.

Chapter 2 describes the theoretical principles underpinning the work presented in this thesis. This begins with a short discussion on electrode reactions, followed by an overview of the development, over the past 150 years, of a model of the solid-liquid interface, and a basic description of the CV technique used to study the interface. A description of the x-ray diffraction techniques used to characterise the electrode surfaces is then given, beginning with elastic scattering from a single electron and building to the case of diffraction from a large 3D crystal; with a focus on the scattered intensity due to the surface, e.g. Crystal Truncation Rods (CTRs). Finally there is a brief description of X-ray Voltammetry (XRV), an extremely useful technique in which x-ray diffraction techniques are combined with CV measurements.

Chapter 3, describes the experimental considerations required to complete an *in-situ* SXS experiment. A brief overview of the preparation and sample transfer to the *in-situ* experimental set-up are given, along with a description of the instrumentation required. Following this is a description of the data acquisition procedure and the necessary correction factors.

Chapter 4 details the characterisation of a Pt(111) surface at various potentials. XRV measurements inside the window of stability were taken at surface sensitive positions. A full set of CTR data at the negative limit was taken in addition to the irreversible oxide region, which showed a markedly different structure to that seen in the reversible oxide region. CTRs of the reduced surface clearly show irreversible roughening. After re-preparation the crystal was then cycled multiple times into the oxide region after which Scanning Tunnelling Microscopy (STM) measurements showed the formation of ordered platinum islands appearing as "fish scales".

In chapter 5 the Pt(100) surface is characterised for the first time at various potentials. XRV measurements were taken at surface sensitive positions and a full set of CTR data at the negative and positive limits were taken. Afterwards the sample was oxidised and the oxidised surface was then characterised. The oxide was reduced and CTR measurements of the reduced surface show irreversible roughening which could be modelled with a beta factor. After re-preparation the crystal was cycled multiple times into the oxide region which, unlike Pt(111), caused a high degree of roughening rather than the formation of platinum islands.

In chapter 6 the $Pt_3Ni(111)$ surface is characterised, including the surface segregation. XRV measurements were taken within the window of stability at surface sensitive positions. Specular CTRs measurements were taken at increasingly positive potentials to allow comparison of the surface segregation. Complimentary *ex-situ* STM measurements were performed, both on the clean surface and after cycling into the oxide region.

The results detailed in the Pt(111) and Pt(100) chapters show a clear trend: the more active the catalyst surface is initially the less stable it is. After cycling multiple times into the oxide region the more active Pt(100) surface roughens, decreasing activity, whereas the stable Pt(111) surface shows little change in activity. $Pt_3Ni(111)$ defies this trend in part as it shares the same morphological changes as Pt(111) after cycling, while retaining its Ni rich sublayer and thus its increased activity.

Chapter 2

Theoretical Principles

2.1 Surface Electrochemistry

2.1.1 Electrode Reactions

All electrode reactions involve a transfer of electrons and it is this charge transfer which is measured in potential sweep experiments, such as Cyclic Voltammetry. Anodic processes occur when electrons are lost by a reactant to the electrode. In potential sweep experiments the charge transfer for anodic processes is positive. The opposite case, cathodic processes, occur when electrons are transferred from the electrode to a reactant and the charge transfer is negative. In this thesis both anodic and cathodic reactions play important roles. The oxidation of an electrode is an anodic reaction whist the reduction is cathodic.

For a reaction to take place there must be a way of balancing charge transfer. For this reason, a functioning electrochemical cell requires at least two electrodes, where the second electrode to acts as a source/sink of electrons. Considering a hypothetical two electrode cell with a solution containing ions O^- and R^+, the reaction taking place at the anode would be:

$$O^- - e^- \rightarrow O \tag{2.1}$$

and the reaction taking place at the cathode would be:

$$R^+ + e^- \rightarrow R \tag{2.2}$$

The total chemical change in the cell would be:

$$O^- + R^+ \rightarrow O + R \tag{2.3}$$

For such electrolysis to take place O^- must diffuse to the anode, R^+ must diffuse to the cathode and electrons must have a path from the anode to the cathode; typically through wires which are external to the cell. The current though such an external circuit, i, is given by:

$$i = AI \tag{2.4}$$

where A is the electrode area and I is the current density. By measuring the current, the charge transfer q can be extracted. Using Faraday's Law the number of moles, m, of the starting product used in the reaction can be found:

$$q = \int_0^t i \, \mathrm{d}t = mnF \tag{2.5}$$

where t is time, n is the number of electrons transferred per molecule of reactant and F is the Faraday constant.

The reactions will only take place spontaneously if the net change in free energy is negative. Assuming this is not the case for the hypothetical cell, the reaction must be driven by applying a potential between the two electrodes. This potential must be greater than the difference between the reversible potentials of the reactions at the anode and the cathode, given by:

$$\Delta G = -nF(E_e^C - E_e^A) \tag{2.6}$$

where ΔG is the Gibbs free energy change associated with the overall cell reaction under the electrolysis conditions, E_e^C and E_e^A are the reversible potentials for the reactions at the cathode and anode respectively. If this condition is met the reaction will still be extremely slow as the ions would need to diffuse to the surface of the electrodes. Rather than relying on diffusion kinetics, the rate of reaction can be increased by applying an over-potential. Thus the voltage, V, required to cause the reaction to take place is:

$$V = E_e^C - E_e^A - |\eta_A| - |\eta_C| - iR \tag{2.7}$$

where $|\eta_A|$ and $|\eta_C|$ are the over-potential at the anode and cathode respectively; and R is the resistance of the circuit. This equation is where the term iR drop originates and it represents energy inefficiencies which must be minimised. iR drop is also one of the main reasons electrochemistry experiments usually use a third electrode, the reference electrode.

By using a reference electrode, a primary electrode can be selected and isolated from the secondary electrode, allowing the measurement of the current to voltage response of just the primary electrode. This primary electrode is also known as the working electrode. In order to isolate the electrode a potentiostat must be used, which is comprised of a feedback circuit based around an operational amplifier. A potentiostat controls the potential at the working electrode using the reference electrode but does not allow any current to pass through the reference electrode therefore reducing iR drop. The counter (secondary) electrode should have a much larger surface area than the working electrode to avoid polarisation effects on the counter electrode. Reference electrodes must be stable in the solutions used, inside the required potential window. This allows a fine control of the potential at the solid/liquid interface.

2.1.2 The Solid/Liquid Interface

In the case of an electrode-electrolyte interface there exists a segregation of positive and negative charges, much like a capacitor. An ideal interface is one in which no charge is transferred no matter how much potential is applied and it is this case that was first modelled by Helmholtz. This model simply included a single layer of ions to balance the excess opposite charge in the electrode. These two layers of opposite charge were called the electrical double layer. Gouy and Chapman furthered this theory by allowing the charged ions in the solution to move freely. This results in a distribution of ions that is greatest near the electrode and decreases with distance to neutrality, where it is effectively the bulk electrolyte. Stern's modification to the Gouy-Chapman model introduced a plane of closest approach due to ions having a finite size, rather than being points. Finally, in Grahames model, a second plane of closest approach was added for ions with solvation shells[40]. As non-specifically as well as specifically adsorbed ions are included it allows the solvent species to be modelled bonding to the surface (see figure 2.1). Once the surface was modeled it was possible to understand the current responses of the electrode-electrolyte interface, which in turn allowed meaningful data to be gathered during experiments such as cyclic voltmmetry.

2.1.3 Cyclic Voltammetry

One of the more popular potential sweep experiments performed in the study of surface electrochemical reactions is Cyclic Voltammetry (CV). As mentioned

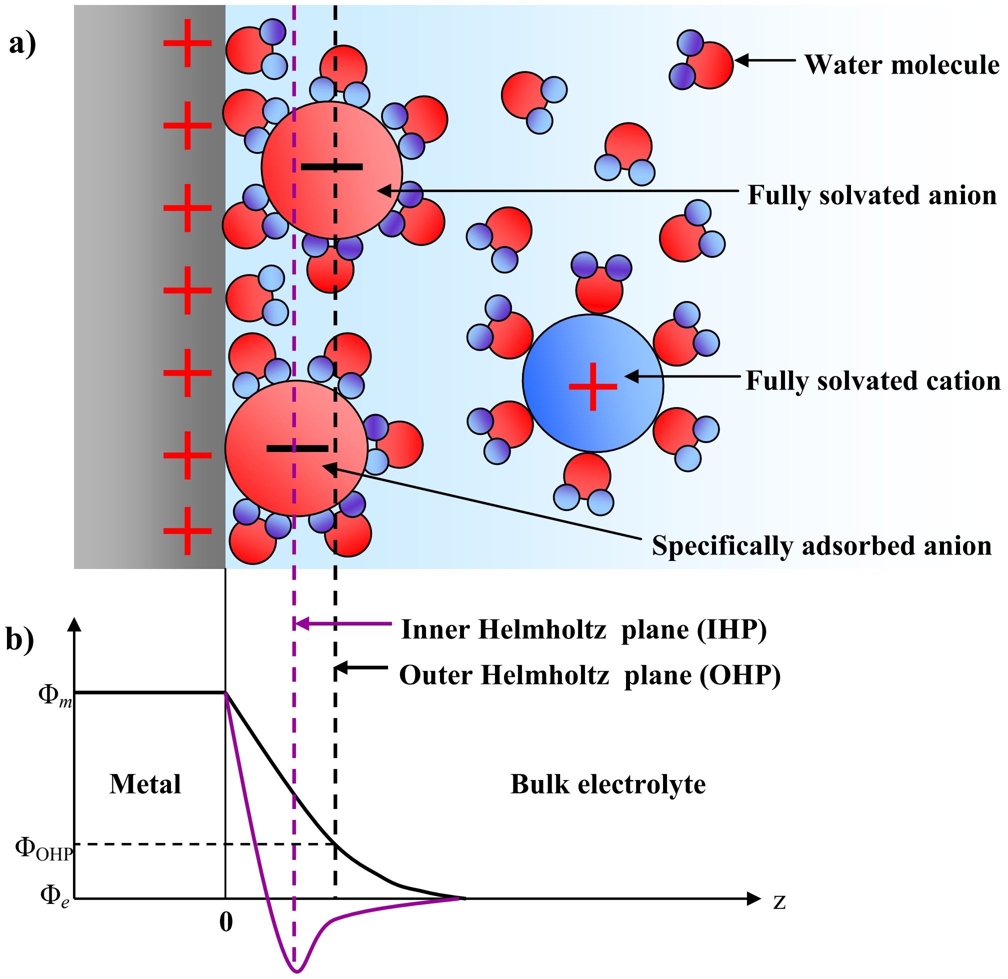

FIGURE 2.1: (a) Schematic diagram of the electrode/electrolyte interface showing fully solvated and specifically adsorbed anions. (b) Potential drop across the interface in the case of fully solvated (black line) and specifically adsorbed anions (purple line). See subsection 2.1.2 for further details.

previously the oxidation and reduction of a species on the electrodes results in an electron transfer. In a CV experiment the potential is cycled linearly with time between two points. The electron transfers that result from the formation/breaking of bonds induced by this cycling cause the current to peak in the cyclic voltammograms at voltages dependent upon the system. When analysing CVs it is known that an electron transfer takes place and usually the number of electrons per molecule but no structural or chemical information is measurable. For this reason CV is usually used in conjunction with other techniques, such as STM and SXS.

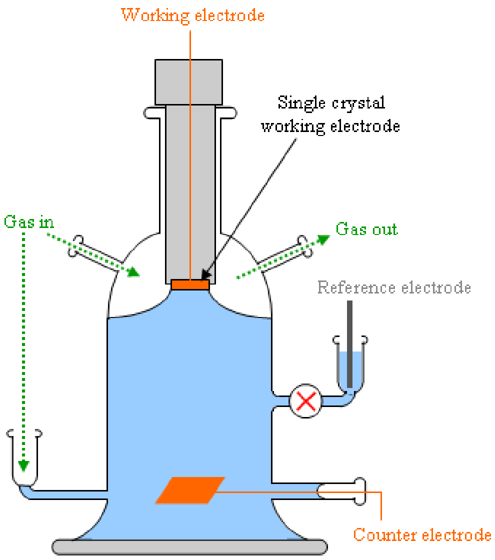

FIGURE 2.2: Schematic diagram of a typical three-electrode electrochemical cell. The electrolyte forms a hanging meniscus with the working electrode surface, ensuring the CV obtained is due to reactions occurring the on well defined single crystal surface and avoiding contact with the polycrystalline sides and back of the crystal. The electrolyte is deoxygenated by purging with N_2 gas.

A schematic of a three electrode, hanging meniscus electrochemical cell is shown in figure 2.2, which is typical of the type used in CV experiments. The working, counter and reference electrodes have been labelled and the working electrode will be the single crystal sample of interest. Reference electrodes commonly used for CV experiments include $Ag/AgCl^-$ and the reversible hydrogen electrode (RHE), where $Ag/AgCl^-$ is the reference used in the experiments in this thesis. $Ag/AgCl^-$ has a potential of +197 mV vs RHE and all potentials stated in this thesis are vs $Ag/AgCl^-$ unless stated otherwise. The potential at the counter electrode is held by a potentiostat relative to the reference electrode, such that current flows only between the working and counter electrodes.

In a CV experiment the working electrode potential is varied with time as shown in the top plot of figure 2.3. The potential is scanned at a constant rate, usually between 1 and 100 mV s^{-1}, from the initial value E_1 to an upper limit E_2. Following this a triangular potential cycle is produced as the reverse potential sweep from E_2 to the original value of E_1 is completed. The bottom plot of figure 2.3 shows the current response for a simple solution phase reversible electron transfer reaction (see equation 2.1) measured during a CV. No current flows initially as the potential is swept positively, due to the potential being below the reaction threshold. As the potential crosses the reaction threshold the observed current increases to a peak. The potential reaches a maximum as the anion diffusion layer depletes and the reaction speed becomes limited by the diffusion rate from the bulk electrolyte. The anion-depleted layer continues to grow as the potential increases, reducing the diffusion rate and thus the current. CVs give valuable information with regards to the potential at which reactions occur, in addition to making it possible to calculate the surface coverage of adsorbates by integration of the current peaks. During the reverse potential sweep the current response is dependent on the reversibility of the electrochemical reaction[41]. In the case of a fully reversible reaction the current peak has an equal integrated intensity and occurs at the same potential as the initial sweep. For an irreversible reaction the charge transfer is reduced and/or the peak position will be shifted. Potential sweep experiments, such as cyclic voltmmetry, are limited as they give no structural information. X-ray diffraction can be used in combination with electrochemistry to give a more rounded view of the interface.

2.2 X-ray Diffraction

Diffraction is an effect that occurs when particles, usually photons, electrons or neutrons, of sufficient energy pass through ordered matter. The experiments in this thesis deal solely with diffraction from single crystals. This section begins with crystallography and leads on to general x-ray diffraction via the kinematical approximation.

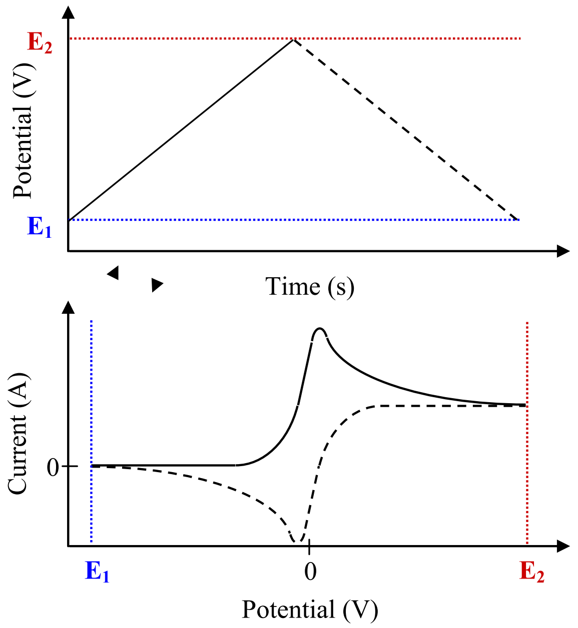

FIGURE 2.3: (Top) Variation of potential with time in a Cyclic Voltammetry experiment. (Bottom) Solution phase cyclic voltammogram for a reversible electron transfer reaction.

2.2.1 Scattering from a Single Electron

The simplest example of scattering is that of scattering from a single electron which must also be considered structureless. In the classical description of scattering from an electron the electrical field component of the x-ray causes the electron to begin vibrating (see figure 2.4). This vibration creates a spherical electrical wave which propagates in all directions. The amplitude of this radiated field at a distance of R from the electron is:

$$E_{rad}(R,t) = -\frac{-e}{4\pi\varepsilon_o c^2 R} a_x(t - \frac{R}{c}) \tag{2.8}$$

where e is the charge on the electron, ε_o is the permittivity of free space, c is the speed of light, and a_x is the acceleration seen by the observer (which is evaluated at an earlier time due to the speed of light being finite). It is important to note the leading minus sign which drops in during the derivation of classical electric dipole radiation. This minus sign shifts the phase of the emitted radiation by π.

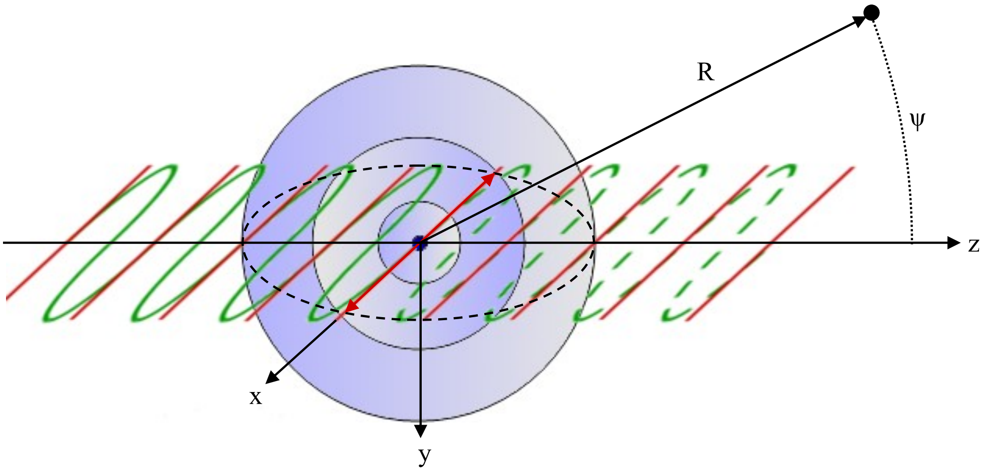

FIGURE 2.4: Classical description of scattering of an x-ray by a free electron. The incident plane wave propagates along the z direction and is polarised along the x axis. The electric field of the incident wave causes the electron to oscillate, which in turn radiates a spherical wave. The observed intensity is calculated at a distance R from the electron.

The acceleration seen by the observer is dependent on the angle of observation out of the plane of polarisation, ψ. The true acceleration must be multiplied by $cos\psi$. If E_{in} is the electric field of the incident wave and E_{x_o} is its amplitude then:

$$E_{in} = E_{x_o} e^{-i\omega t} \tag{2.9}$$

Thus the observed acceleration, where m is the mass of the electron and ω is the frequency of the oscillation, would be:

$$a_x(t) = \frac{-e}{m} E_{x_o} e^{-i\omega(t-\frac{R}{c})} cos\psi = \frac{-e}{m} E_{in} e^{i\omega\frac{R}{c}} cos\psi \tag{2.10}$$

This allows equation 2.10 to be rewritten, giving the amplitude of the emitted wave as a function of the incoming wave.

$$\frac{E_{rad}(R,t)}{E_{in}} = \left(\frac{e^2}{4\pi\varepsilon_0 mc^2}\right) \frac{e^{ik_0R}}{R} cos\psi \tag{2.11}$$

or

$$\frac{E_{rad}(R,t)}{E_{in}} = r_0 \frac{e^{ik_0R}}{R} cos\psi \tag{2.12}$$

where r_0 is the Thomson scattering length or classical electron radius. The experiments in this thesis are performed with horizontally polarised x-rays thus $cos\psi = 1$ in all cases and will henceforth be disregarded.

2.2.2 One Atom

When considering scattering from a classical approach the atom consists of a cloud of electrons around a nucleus. As the scattering is not from a point source the scattered wave is no longer spherically symmetrical. The scattering field becomes a superposition of scattering from all points within the atom. Taking first the example of two points within this atom, one at a position $\hat{r}$ from the other. The difference in phase of the incident wave is $\hat{k}_i \cdot \hat{r}$, where $\hat{k}_i$ is the incident wavevector. A similar shift in phase occurs with the outgoing wave. This gives a phase difference of:

$$\Delta\Phi(\hat{r}) = (\hat{k}_i - \hat{k}_f) \cdot \hat{r} = \hat{Q} \cdot \hat{r} \tag{2.13}$$

where $\hat{Q}$ is the momentum transfer. By viewing the electrons as a charge cloud with a number density of $\rho(\hat{r})$, the charge at any volume element $d\hat{r}$ within the atom would be proportional to $\rho(\hat{r})\mathrm{d}\hat{r}$. The integral of $\rho(\hat{r})\mathrm{d}\hat{r}$ would be:

$$\int \rho(\hat{r})\,\mathrm{d}\hat{r} = Z \tag{2.14}$$

where Z is the number of electrons. Including the phase factor $e^{i\hat{Q}\cdot\hat{r}}$ gives the scattering amplitude:

$$f^0(\hat{Q}) = \int \rho(\hat{r}) e^{i\hat{Q}\cdot\hat{r}}\, \mathrm{d}\hat{r} \tag{2.15}$$

where $f^0(\hat{Q})$ is the atomic form factor in units of the Thomson scattering length. It can be seen that, due to the phase factor, the amplitude of diffraction an vary from Z at $\hat{Q} = 0$ to 0 at $\hat{Q} = \infty$. Classically the scattering intensity would be the complex conjugate of $f^0(\hat{Q})$ but as atomic electrons are governed by quantum mechanics additional effects must be considered. Electrons have discrete binding energies, the most bound being the K band. X-rays have an energy that is usually in the region of the K band binding energy. If the X-ray energy is lower than the K band binding energy they do not respond strongly to the x-rays. Electrons in the L, M etc. shells will still cause scattering but at a reducing intensity. This is the first of the dispersion corrections, denoted $f'(\hat{E})$, which also displays a resonant behaviour around the electron binding energies, causing a marked drop in the scattering amplitude. The second dispersion correction, $if''(\hat{E})$, is an imaginary term which represents energy dissipation in the system. It is worth noting that both parts of the dispersion correction are dependent on the energy of the incident x-ray and not the momentum transfer. This gives a corrected atomic form factor as:

$$f^0(\hat{Q}, E) = f^0(\hat{Q}) + f'(\hat{E}) + if''(\hat{E}) \tag{2.16}$$

2.2.3 Crystallographic Definitions

Before scattering from a crystal can be described the crystal must first be defined. A crystal is periodic a array of lattice points with long range order and these lattice points consist of a group of atoms known as a basis. A lattice is best described by the vectors between nearest neighbour lattice points. In the case of a 3D crystal, as found in this thesis, three vectors $\hat{a}$, $\hat{b}$ and $\hat{c}$, and the angles between them

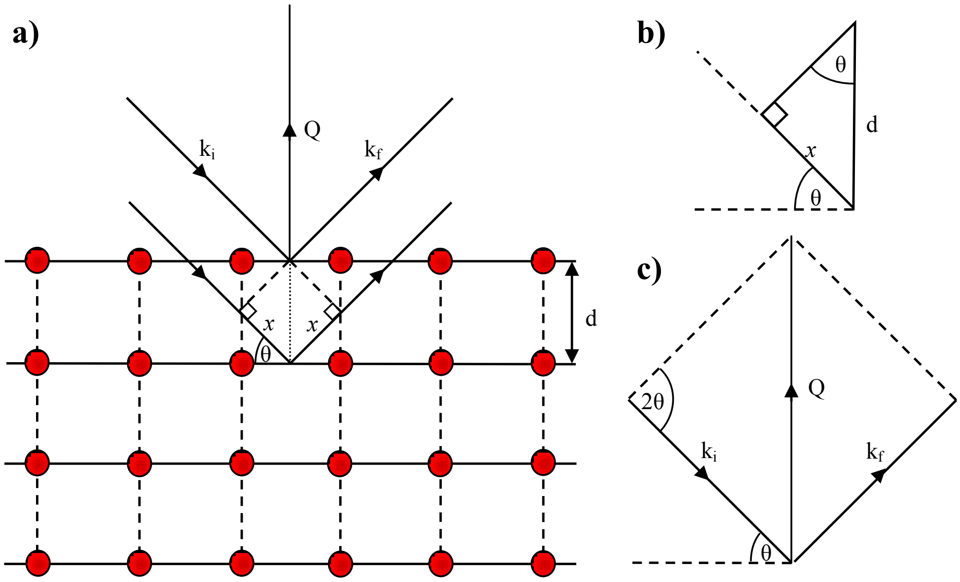

FIGURE 2.5: Schematic representation of the scattering from a series of parallel atomic planes, separated by a distance d. The incident x-ray beam has a wave-vector k_i and approaches at an angle of incidence of θ. The scattered beam has a wave-vector k_f.

α, β and γ, are required to define the lattice. An integer (positive or negative) number of translations along these vectors from one lattice point will locate any other lattice point. The parallelepiped defined by the vectors $\hat{a}$, $\hat{b}$ and $\hat{c}$ is known as a unit cell (see figure 2.6).

2.2.4 Crystal Planes and Millar Indices

The 3D crystal structure can be generated by repeating the unit cell at every lattice point. As this 3D crystal is infinite there are an infinite number of 2D planes associated with it. As x-ray diffraction is concerned with scattering from these planes a convenient way of grouping families of planes is required (a schematic representation of such scattering is shown in figure 2.7). Millar indices are an ideal way of achieving this and are denoted by (h, k, l). h, k and l are derived by finding the plane that is closest to the origin of the crystal lattice. The intercepts of this plane are found in terms of the lattice vectors a, b and c. Taking the

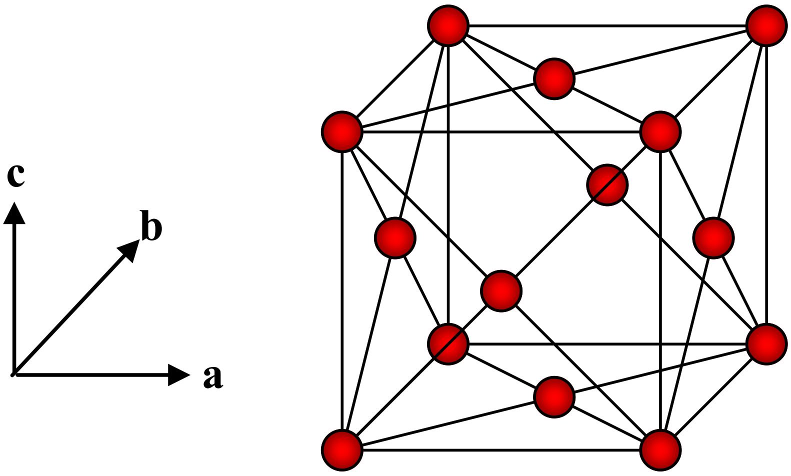

Figure 2.6: The face centred cubic (fcc) crystal structure. This is a cubic lattice with a four atom basis. In this case $\hat{a} = \hat{b} = \hat{c}$ and the angles between them $\alpha = \beta = \gamma = 90°$.

reciprocals of these intercepts and multiplying by the common denominator gives the Millar indices. The (100), (110) and (111) low index planes for Face Centred Cubic (FCC) crystals are shown in figure 2.7. Directions in cubic crystals, such as FCC, are denoted as $[h\ k\ l]$ and are perpendicular to the plane with the Millar indices of $(h\ k\ l)$. Inter-planer lattice spacing d_{hkl} can be calculated from the Millar indices using:

$$\mathrm{d}_{hkl} = \frac{a_0}{\sqrt{h^2 + k^2 + l^2}} \tag{2.17}$$

where a_0 is the cubic lattice parameter.

2.2.5 Scattering from the Unit Cell

As mentioned previously, the unit cell contains the basis of the crystal which is repeated at every lattice point. The scattering amplitude of one unit cell can be found by simply summing the contributions of all of the atoms it contains. The

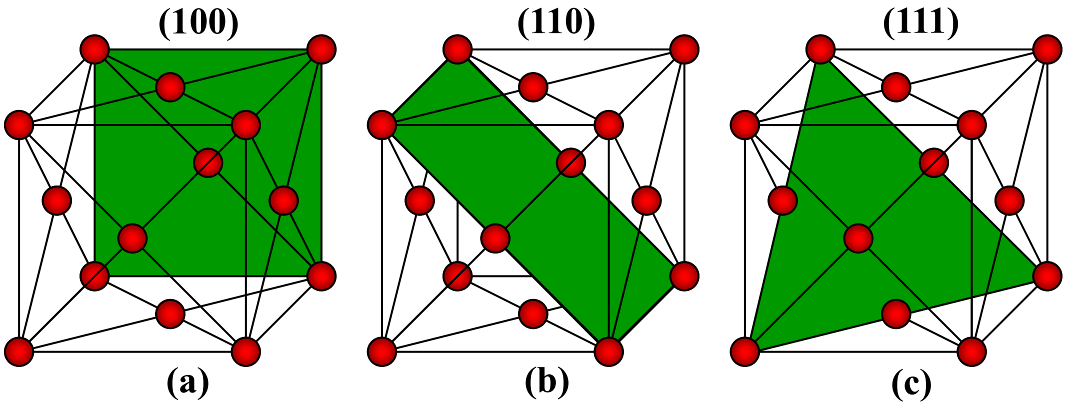

(a) (b) (c)

FIGURE 2.7: The three low index planes for fcc crystals (a) (100), (b) (110) and (c) (111)

atoms in the unit cell do not have to be the same element as each is assigned an individual form factor $f_j(\hat{Q})$. The unit cell form factor would be:

$$F^{UNIT}(\hat{Q}) = \sum_{\hat{r}_j} f_j(\hat{Q})e^{i\hat{Q}\cdot\hat{r}_j} \tag{2.18}$$

for a unit cell of j atoms, where $\hat{r}_j$ is the position of each atom.

2.2.6 Scattering from a Crystal

Even with the most powerful x-ray sources in existence it is currently impossible to detect the scattering from a single molecule or unit cell. By using crystals the scattered intensity can be boosted by many orders of magnitude. The crystal form factor can be found using a similar summation as used in previous steps:

$$F^{crystal}(\hat{Q}) = \sum_{\hat{r}_j} f_j(\hat{Q})e^{i\hat{Q}\cdot\hat{r}_j} \sum_{\hat{R}_n} e^{i\hat{Q}\cdot\hat{R}_n}, \tag{2.19}$$

where $\hat{R}_n$ is the position of each unit cell and equals:

$$\hat{R}_n = n_1\hat{a} + n_2\hat{b} + n_3\hat{c}, \tag{2.20}$$

where n_1, n_2 and n_3 are integers. Due to the large size of the crystals, when compared with the x-ray beam footprint, used in x-ray experiments the lattice sum component of equation 2.19 contains a vast number of unit cells; such that it equals zero except under the condition:

$$\hat{Q} \cdot \hat{R}_n = 2\pi \times integer \tag{2.21}$$

where the summation will be equal to the number of terms, approximately of the order of 10^{12} for a small crystallite.

2.2.7 Diffraction Conditions

To find a solution to equation 2.21 the reciprocal lattice may be introduced such that:

$$\begin{aligned} \hat{a} \cdot \hat{a}^* &= 2\pi \\ \hat{b} \cdot \hat{b}^* &= 2\pi \\ \hat{c} \cdot \hat{c}^* &= 2\pi \end{aligned} \tag{2.22}$$

where $\hat{a}^*$, $\hat{b}^*$ and $\hat{c}^*$ are the reciprocal lattice vectors. The reciprocal lattice would then be defined as:

$$\hat{G} = h\hat{a}^* + k\hat{b}^* + l\hat{c}^* \tag{2.23}$$

where h, k and l are the Millar indices and take integer values. Combining equations 2.20 and 2.23 it can be seen that:

$$\hat{G} \cdot \hat{R}_n = 2\pi(hn_1 + kn_2 + ln_3) \tag{2.24}$$

It follows that equation 2.21 is satisfied when:

$$\hat{Q} = \hat{G} \tag{2.25}$$

so diffraction from a perfect infinite crystal only occurs when $\hat{Q}$ equals a reciprocal lattice vector. This is known as the Laue condition.

2.2.8 Reciprocal Lattice

The final problem that requires solving at this point is finding the reciprocal lattice vectors in terms of the real space lattice vectors. This is simple in the case of a 1D lattice but becomes more complicated for 2D and 3D lattices. It can be shown that for a 3D lattice the reciprocal lattice basis vectors are:

$$\begin{aligned} \hat{a}^* &= \frac{2\pi}{V_c}(\hat{b} \times \hat{c}) \\ \hat{b}^* &= \frac{2\pi}{V_c}(\hat{c} \times \hat{a}) \ , \\ \hat{c}^* &= \frac{2\pi}{V_c}(\hat{a} \times \hat{b}) \end{aligned} \tag{2.26}$$

where $V_c = \hat{a} \cdot (\hat{b} \times \hat{c})$ which is the volume of the unit cell. Substituting these into equation 2.23 forms a 3D lattice of reciprocal space points which satisfy the Laue condition. This lattice can be used to find the positions of maximum scattered intensity, or Bragg points.

2.3 Surface X-Ray Diffraction

2.3.1 Scattering from a Semi-Infinite Crystal

The theory presented so far has been for the case of an infinite 3D crystal. The crystals used in x-ray diffraction experiments are truncated, with the interface even being sub-surface in some cases. To begin modelling a surface an isolated 2D monolayer can be considered. In this case $\hat{R}_n$ is altered so that $n_3 = 0$ where $\hat{c}$ is the crystal lattice vector along the surface normal so that:

$$\hat{R}_n = n_1\hat{a} + n_2\hat{b} \ , \tag{2.27}$$

This alters equation 2.19 showing that the form factor for scattering from the 2D is:

$$F^{crystal}(\hat{Q}) = \sum_{\hat{r}_j} f_j(\hat{Q}) e^{i\hat{Q}\cdot\hat{r}_j} \sum_{n_1,n_2} e^{i\hat{Q}\cdot(n_1\hat{a}+n_2\hat{b})} \ , \tag{2.28}$$

leading to the scattering condition being:

$$\hat{G} = h\hat{a}^* + k\hat{b}^* \ , \tag{2.29}$$

where $\hat{Q} = \hat{G}$. This scattering pattern is no longer a lattice in reciprocal space but 1D rods with constant intensity perpendicular to the a^*b^* plane in reciprocal space. In the case of a perfectly terminated semi infinite crystal the diffraction pattern would be a sum of the diffraction from an infinite crystal and the diffraction from a single monolayer, giving both the fixed intensity rods and intense Bragg points. The diffraction pattern measured from a real surface differs from this ideal case. The Bragg points are not true points but are instead smeared out along the l direction which, in addition to the rods caused by the surface, are commonly known as crystal truncation rods (CTRs) (see figure 2.8). The intensity is streaked between the Bragg peaks because in a real case the crystal is not infinite. The beam footprint is usually of the order of 0.1-1 mm on the crystal surface which is large enough to be considered infinite, however in comparison the penetration depth of X-rays is many orders of magnitude smaller and must be considered finite.

In this case:

$$F^{CTR}(\hat{Q}) = \sum_{\hat{r}_j} f_j(\hat{Q}) e^{i\hat{Q}\cdot\hat{r}_j} \sum_{n_1,n_2} e^{i\hat{Q}\cdot(n_1\hat{a}+n_2\hat{b})} \sum_{n_3} e^{i\hat{Q}\cdot(n_3\hat{c})} \tag{2.30}$$

If n_3 is a large number and the in plane Laue conditions are met then:

$$F^{CTR}(\hat{Q}) = F^{UNIT}(\hat{Q}) n_1 n_2 \sum_{n_3} e^{i\hat{Q}\cdot(n_3\hat{c})} \ . \tag{2.31}$$

The measured intensity would then be:

$$I = I_0 \left(\frac{r_0}{R}\right)^2 \left|F^{CTR}(\hat{Q})\right|^2 \tag{2.32}$$

then:

$$I = I_0 \left(\frac{r_0}{R}\right)^2 \left|F^{UNIT}(\hat{Q})\right|^2 n_1^2 n_2^2 \left|\sum_{n_3} e^{i\hat{Q}\cdot(n_3\hat{c})}\right|^2 \ , \tag{2.33}$$

as:

$$\sum_{n_3} e^{i\hat{Q}\cdot(n_3\hat{c})} = \frac{1 - e^{i\hat{Q}\cdot(n_3\hat{c})}}{1 - e^{i\hat{Q}\cdot\hat{c}}} \tag{2.34}$$

$$\begin{aligned}\left|\sum_{n_3} e^{i\hat{Q}\cdot(n_3\hat{c})}\right|^2 = &\left|\frac{(1-e^{i\hat{Q}\cdot(n_3\hat{c})})(1-e^{i\hat{Q}\cdot(n_3\hat{c})})}{(1-e^{i\hat{Q}\cdot\hat{c}})(1-e^{i\hat{Q}\cdot\hat{c}})}\right| \\ &\left|\frac{1+1-e^{i\hat{Q}\cdot(n_3\hat{c})}-e^{i\hat{Q}\cdot(n_3\hat{c})}}{1+1-e^{i\hat{Q}\cdot\hat{c}}-e^{i\hat{Q}\cdot\hat{c}}}\right| \\ &\left|\frac{1-cos(\hat{Q}\cdot n_3\hat{c})}{1-cos(\hat{Q}\cdot\hat{c})}\right| \\ &\left|\frac{sin^2(\hat{Q}\cdot n_3\hat{c}/2)}{sin^2(\hat{Q}\cdot\hat{c})/2)}\right|\end{aligned} \tag{2.35}$$

For large values of n_3, $\left|sin^2(\hat{Q}\cdot n_3\hat{c}/2\right|$ will be a rapidly oscillating function. Due to the resolution restrictions during experiments this oscillation is never observed and thus the approximation of the average value of $1/2$ can be used. This gives the scattered intensity from a perfectly terminated crystal as:

$$I = I_0\left(\frac{r_0}{R}\right)^2\left|F^{UNIT}(\hat{Q})\right|^2 n_1^2 n_2^2\left|\frac{1}{2sin^2(\hat{Q}\cdot\hat{c})/2)}\right|. \tag{2.36}$$

2.3.2 Modelling Surface Structure

In most cases a surface x-ray diffraction experiment will not be performed on a perfectly terminated crystal. Surface relaxation, roughness and surface occupation will all affect the CTR intensity profile. Reducing the surface occupation will decrease the scattered x-ray intensity at reciprocal space positions between Bragg peaks, with the greatest decrease seen exactly half way between Bragg peaks at the anti-Bragg positions. In the case of surface expansion the shape of the Bragg peaks change, becoming asymmetrical; an example of this is shown in figure 2.9. The CTR for which there is no in-plane momentum transfer during diffraction is known as the specular CTR and it is sensitive to electron density along the surface normal. Off specular CTRs have an in-plane component to the momentum transfer

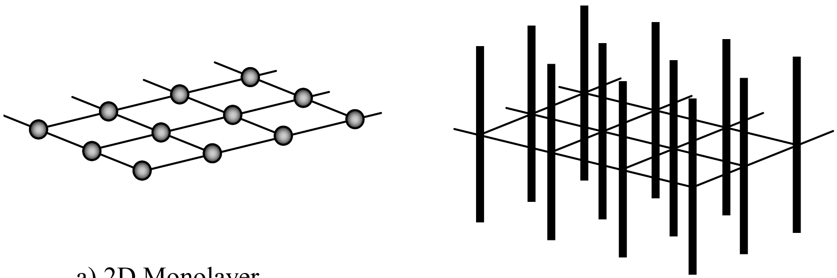

a) 2D Monolayer

d) 2D Monolayer

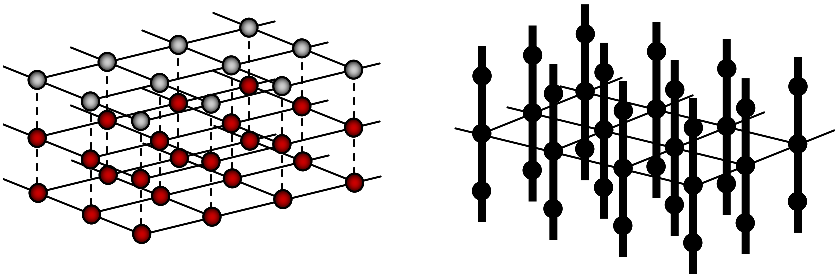

b) Crystal Surface

e) Bulk Crystal and 2D Layer

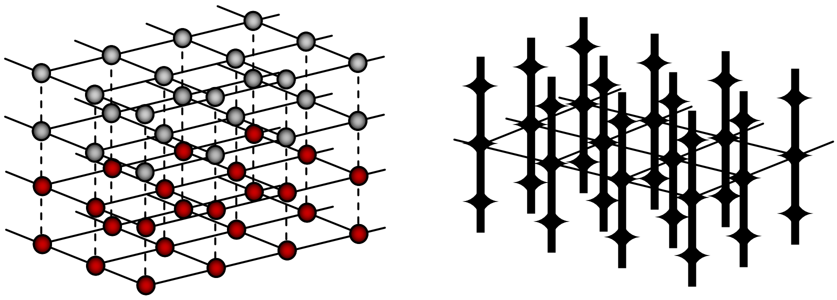

c) Crystal-Crystal Interface

f) Crystal Truncation Rods

FIGURE 2.8: Real space structures for (a) a two dimensional monolayer, (b) the surface of a crystal and (c) a crystal-crystal interface. Reciprocal space diffraction pattern for (d) an isolated monolayer, (e) the superposition of a 2D monolayer onto a bulk crystal and (f) a more realistic representation of the intensity along the crystal truncation rods (CTR).

and are only sensitive to atoms near lattice positions. Due to this, if the surface is coated with a structure that is different from the bulk crystal, such as NiO on Ni, the off specular measurements are sensitive to the interface between the two but not the surface.

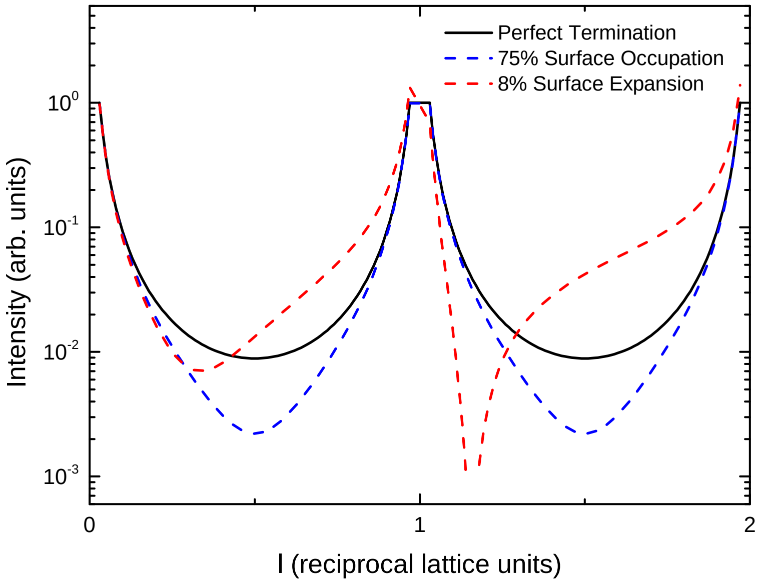

FIGURE 2.9: CTR profile for the case of a perfectly terminated crystal (solid black line), a crystal with an expanded surface layer (red dashed line) and a surface with a relative occupation of 85% (dashed blue line).

2.3.3 The (111) FCC surface

The most densely packed surface of the two low index surfaces used in this thesis is the FCC (111) surface. Figure 2.10 shows a computer generated image of the hexagonally close packed surface structure. The simplest definition of the hexagonal unit cell requires two vectors $\hat{a}$ and $\hat{b}$, with a magnitude of the nearest neighbour spacing and an angle of 120^o separating them. Due to the ABC stacking, repetition along the surface normal only occurs every three atomic layers; which defines the $\hat{c}$ lattice parameter, shown in figure 2.10b. The reciprocal lattice can be calculated using the method detailed earlier in this chapter, the result is shown in figure 2.10c. The $[h00]_{hex}$ and $[0k0]_{hex}$ directions are in plane with the surface, separated by an angle of 60^o, while the $[00l]_{hex}$ is along the surface normal. The amplitude of the reciprocal lattice vectors are:

$$a^* = b^* = \frac{4\pi}{\sqrt{3}a_{NN}} \tag{2.37}$$

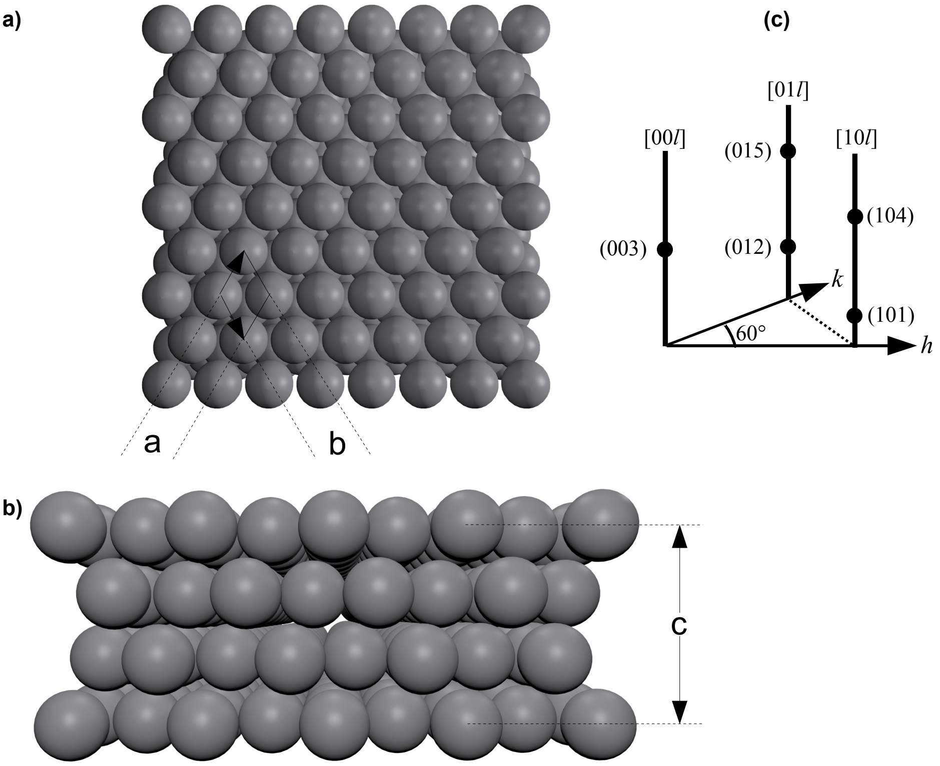

FIGURE 2.10: Fcc(111) real space surface structure: (a) top view and (b) side view. (c) Corresponding reciprocal space lattice.

and

$$c^* = \frac{2\pi}{\sqrt{6}a_{NN}} \tag{2.38}$$

Figure 2.10c shows that the Bragg peaks are separated by three $\hat{c}^*$ in the [00l] direction, which is due to the three atomic layer thickness along the surface normal direction of the real unit cell. The following equations relate the [111] surface notation to the [001] bulk notation:

$$\begin{aligned} h_{fcc} &= \frac{2}{3}h_{111} - \frac{2}{3}k_{111} + \frac{l_{111}}{3} \\ k_{fcc} &= \frac{2}{3}h_{111} + \frac{4}{3}k_{111} + \frac{l_{111}}{3} \\ l_{fcc} &= -\frac{4}{3}h_{111} - \frac{2}{3}k_{111} + \frac{l_{111}}{3} \end{aligned} \tag{2.39}$$

such that the (003) Bragg peak using the surface notation is seen to be the (111) bulk Bragg peak.

Evaluating the CTR scattering profile first requires the bulk structure factor F_{Bulk}, given by:

$$
\begin{aligned}
f^{Bulk} &= f^0(\hat{Q}) DW_{Bulk} \sum_n e^{in\left(2\pi\left(\frac{h}{3}-\frac{k}{3}-\frac{l}{3}\right)\right)} \\
&= \frac{f^0(\hat{Q}) DW_{Bulk}}{1-e^{2\pi i\left(\frac{h}{3}-\frac{k}{3}-\frac{l}{3}\right)}}
\end{aligned}
\tag{2.40}
$$

where $f^0(\hat{Q})$ is the Q dependent atomic form factor and n is summed across infinity. The Debye-Waller factor, DW_{Bulk}, accounts for thermal disorder, decreasing the intensity of the diffracted x-rays, and depends on the root mean square (rms) displacement of the atoms (σ) from their average position; this is caused by thermal vibration. The relationship between the displacement σ and the Debye-Waller factor DW_{Bulk} is shown in equation (2.41),

$$
DW_{Bulk} = e^{-\frac{1}{2}\left(\hat{Q}\sigma\right)^2} \ . \tag{2.41}
$$

The Debye-Waller factor can be calculated from the Debye temperature which can be found, for all elements, in the International Tables for Crystallography [42].

In the case of metal crystals, as seen in this thesis, the bonds are not strongly directional and the CTR data can be modelled by considering relaxations in the top three or four layers. The scattering of the surface layers can be considered a continuation of the scattering from the bulk structure, giving:

$$
f^{Surf} = f^0(\hat{Q}) \theta_n DW_n e^{in\left(2\pi\left(\frac{h}{3}-\frac{k}{3}-l\left[\frac{1}{3}+\epsilon_n\right]\right)\right)} \tag{2.42}
$$

Due to the difference in atomic bond strengths in the near surface region compared to the bulk, the Debye-Waller factor (DW_n) is considered separately for each layer. The relative occupation of individual surface layers can be altered with the θ_n term, which is simply a multiplicative fraction controlling the atomic density of individual layers. Compared to a perfect crystal termination, a relaxed surface layer gives an asymmetry in the CTR profile around the Bragg peaks. The surface normal displacement, i.e. the surface relaxation, can be controlled for each layer with the ϵ_n term. The change in scattering is caused by interference between the x-ray scattering from the modified surface layers and the bulk crystal. The total scattered intensity is given by:

$$I^{Tot} = \left|f^{Tot}\right|^2 = \left|f^{Bulk} + f^{Surf}\right|^2 \ . \tag{2.43}$$

Using this equation it can be seen that certain positions on the CTR are particularly sensitive to specific changes in the surface atomic layers. For example, positions close to Bragg peaks (such as ((0 0 2.7) or (1 0 0.7)) would change greatly if the surface underwent a relaxation, whereas a roughening of the surface would not affect the intensity to any great degree. On the other hand, positions half way between Bragg peaks (such as (0 0 1.5) or (1 0 2.5)) would show a decrease if the surface roughened but little change with surface relaxation.

2.3.4 The (100) surface

The (100) surface is more open than the (111) surface. A computer generated model of this surface is shown in figure (2.11), along with the surface unit cell and the corresponding reciprocal space map. The amplitude of the reciprocal space lattice vectors are:

$$\hat{a}^* = \hat{b}^* = \frac{2\pi}{a_{NN}} \tag{2.44}$$

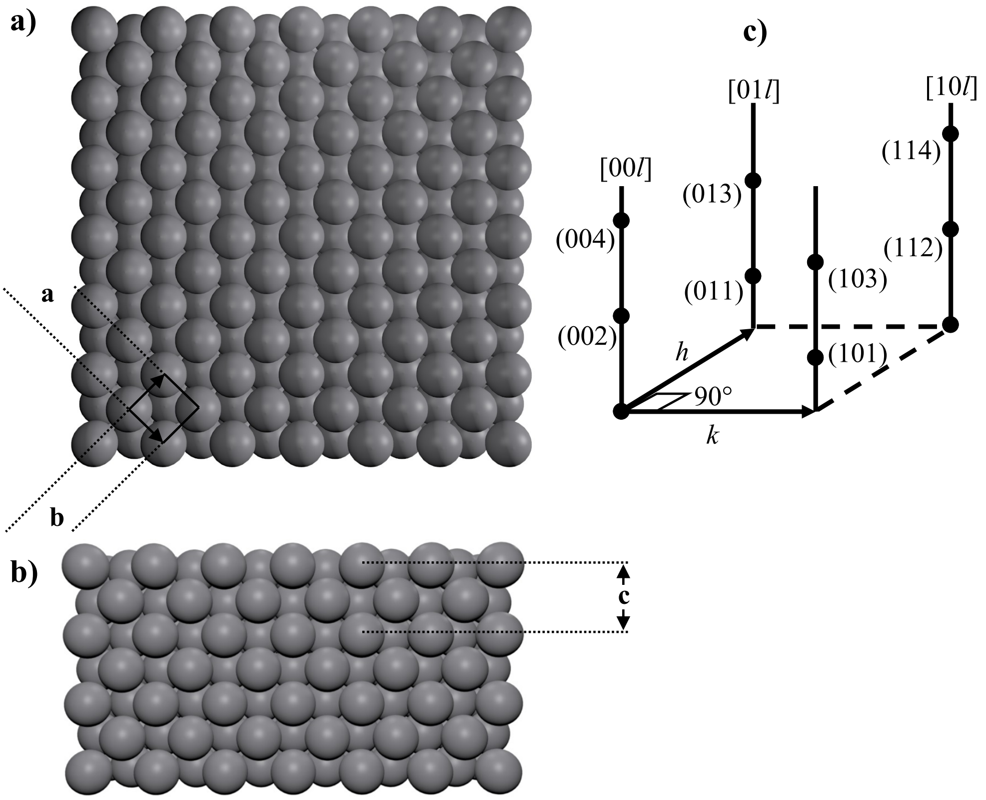

FIGURE 2.11: Fcc(100) real space surface structure: (a) top view and (b) side view. (c) Corresponding reciprocal space lattice.

and

$$\hat{c}^* = \frac{4\pi}{\sqrt{2}a_{NN}} \ . \tag{2.45}$$

The following equations relate the tetragonal surface unit cell shown in figure (2.11) to the bulk cubic unit cell:

$$\begin{aligned} h_{fcc} &= h_{100} + k_{100} \\ k_{fcc} &= h_{100} - k_{100} \ . \\ l_{fcc} &= l_{100} \end{aligned} \tag{2.46}$$

As with the case of the (111) surface, the CTRs for the (100) surface by considering the scattering from the bulk crystal and the surface layers separately. The bulk structure factor in this case is:

$$f^{Bulk} = \frac{f^0(\hat{Q})DW_{Bulk}}{1 - e^{2\pi i\left(\frac{h}{2}+\frac{k}{2}+\frac{l}{2}\right)}} \tag{2.47}$$

and the scattering from the surface layers is:

$$f^{Surf} = f^0(\hat{Q})\theta_n DW_n e^{in\left(2\pi\left(\frac{h}{2}+\frac{k}{2}+l\left[\frac{1}{2}+\epsilon_n\right]\right)\right)} \tag{2.48}$$

The total scattered intensity is once again given by equation (2.43). Examples of reciprocal lattice positions which are sensitive to surface relaxation would be (0 0 1.8) and (1 0 0.8) which are close to the Bragg peaks at (0 0 2) and (1 0 1) and as can be seen from figure 2.9, the greatest changes during relaxation occur near Bragg peaks. Examples of positions sensitive to surface roughness are (0 0 1) and (1 0 2). These are points halfway between braggpeaks but also known as anti-Bragg points, figure 2.9 also shows the surface occupation as well as surface roughness causes the greatest change at these points.

2.4 β Factor

The β factor roughness model used in this thesis was found by Robinson, in 1986 [4], to work well on a variety of samples. It is a simple model of statistical roughness and the modifying factor has a similar form to those commonly used to explain scattering from systems with partial stacking disorder. The β factor is an exponential distribution of heights where the first layer is fully occupied, the second has an occupancy of β and the third has an occupancy of β^2 and so on. This modifies equation 2.36 such that:

$$I_{Rough} = I_{CTR} \frac{(1-\beta)^2}{1+\beta^2-2\beta cos(\hat{Q}\cdot\hat{a}_3)} \ . \tag{2.49}$$

2.5 X-ray Voltammetry

X-ray Voltammetry (XRV) is an extremely useful combination of x-ray diffraction and cyclic voltammetry. Figure 2.9, and equations 2.42 and 2.48, show that certain structural properties of the surface affect the diffracted CTR intensity. The diffracted x-ray intensity is measured at a fixed position in reciprocal space which is sensitive to changes on the surface, such as surface relaxation or surface roughness. Cycling across a potential range can then give a great insight into potential dependent sample stability and structural effects. XRV measurements are used to find interesting, potential dependent, structural changes, which can then be characterised by potentiostatic CTR measurements. The atomic scale structural changes of the surface found by XRV measurements can be linked to the macroscopic electrochemical phenomena found in CV measurements. Surface structures such as reconstructed surface layers, ordered adsorbate layers and changes in surface segregation can all be monitored by XRV measurements.

2.6 Summary

Information regarding the transfer of electrons to and from the electrode surface can be provided using cyclic voltammetry while information on the surface atomic structure can be provided from surface x-ray diffraction measurements. By combining these techniques *in-situ* it is possible to directly monitor the atomic structure of the surface during reactions. A method of note is the XRV technique which allows the potential dependence of the surface structure to be probed. A picture of the processes occurring at the interface, and any induced structural changes, can be built up using a combination of CV and XRV measurements. A description of the experimental methodology in which the x-ray techniques are applied to the study of the electrochemical interface is given in detail in chapter 3.

Chapter 3

Experimental Details

3.1 Introduction

Using *in-situ* x-ray diffraction and electrochemistry techniques to study the electrode/electrolyte interface has become a well established research area, with multiple groups using this combination since the initial experiments in the 1980s. To achieve reliable results, various issues such as sample quality and environment must be addressed. The procedure for preparation of a crystal sample is detailed in this chapter, in addition to the transfer method to the *in-situ* experimental set up. Following this is an introduction to the experimental cell designs and an introduction to the required instrumentation. The chapter ends with a description of the typical experimental procedure which details the steps needed to achieve reliable data.

3.2 Sample Preparation

Preparation of the single crystal surface is the first stage in the experimental procedure and is vital to obtain a well defined surface. The samples used in this thesis are metallic, or bi-metallic, single crystals; aligned so the surfaces are the (111) or (100) crystal planes, with a maximum miscut of 0.2^o. The Pt(111) crystal is disc shaped, 10 mm diameter and with a depth of 3 mm, whereas the Pt(100) and $Pt_3Ni(111)$ crystals are both disc shaped and 6 mm diameter with a depth of 6 mm.

Sample preparation is dependent on the sample, however in this case it is common to all the crystals used. The surface is mechanically polished using diamond polishing paste, giving an optically good surface. To achieve a good single crystal surface the crystal is annealed for 24 hours at approximately 800^oC in a hydrogen atmosphere. The surface atoms rearrange into their lowest energy configuration upon cooling, providing large low index terraces with an orientation dependent on the surface alignment. A phase of ultra high vacuum (UHV) preparation is required next; argon ion sputter and thermal annealing cycles are used to produce a clean surface, free of oxygen and carbon. After each cycle the surface can be monitored using low energy electron diffraction (LEED) and Auger electron spectroscopy (AES) until a clean, good quality surface is observed. On leaving the UHV environment the sample surface must be protected with a drop of electrolyte and transferred to the electrochemical environment quickly, to ensure the surface is exposed to the atmosphere for as little time as possible. Cyclic voltammetry is also a useful tool for known systems, as it can be compared to the CV published in the scientific literature, giving another method for monitoring surface condition.

For subsequent experiments repreparation of the surface is necessary, which, in the case of reactive surfaces such as $Pt_3Ni(111)$, requires the UHV preparation detailed earlier. In the case of more stable crystal surfaces, such as Pt(111), the surface can be reprepared without UHV, using either the flame annealing technique [43] or a radio frequency (RF) annealer. The RF annealer has advantages over the flame annealing technique in that the sample can be annealed and cooled in the desired atmosphere, such as a Ar and H mix, allowing a more controlled preparation environment. Both methods produce a good quality surface, confirmed by both CV and SXS [44].

3.3 Electrochemical Cell

3.3.1 The Conventional X-ray Electrochemical Cell

After surface preparation a drop of electrolyte or ultra pure water placed on the crystal surface to protect it from the atmosphere. Following this the crystal is transferred to the electrochemical cell (schematic is shown in figure 3.1). The x-ray cell has not changed much since the first in-situ x-ray diffraction experiments [8, 9] and has been described in detail in the following references [5, 45, 46]. Due to being chemical inert and its ability to be machined, Kel-F is the material of choice for the body of the cell. Once the crystal is placed in a sample holder and screwed tightly into the body, it is held firmly with the surface as the highest point of the cell. The working and counter electrodes enter the cell through screw-in fittings, which are sealed with ferrules to ensure there are no air leaks. The connection is made between the working electrode and the crystal by passing the wire through the base of the cell, so that it contacts the back of the crystal. The electrolyte inlet and outlet enter the cell on opposite sides in the same manner as the electrodes. A rubber O-ring system holds a polypropylene film over the top of the cell, creating a sealed system.

The electrolyte is held in a reservoir, allowing degassing by way of N_2 gas. The reservoir is connected to the cell by 3 mm Teflon tubing, with a tap allowing separation when required. The outlet from the cell leads to a syringe, again connected with 3 mm tubing including a tap. The taps are used to isolate the cell and maintain a fixed volume of liquid (figure (3.2)). In this cell design the electrolyte has access to the poly crystalline back and sides of the cell, which is a major drawback as it leads to unreliable electrochemical measurements. By first

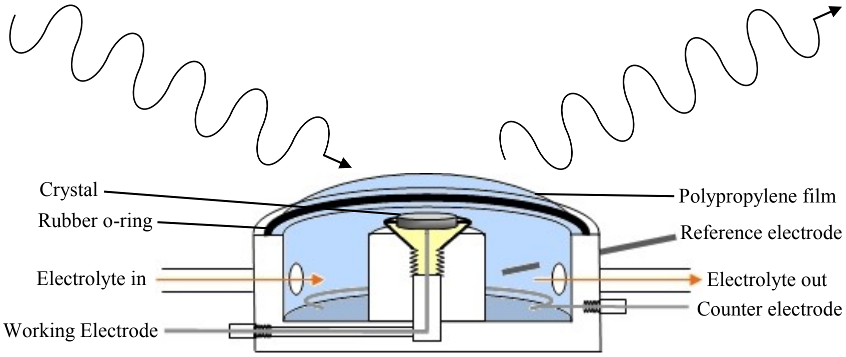

Figure 3.1: Schematic cross-sectional view of the x-ray electrochemical cell

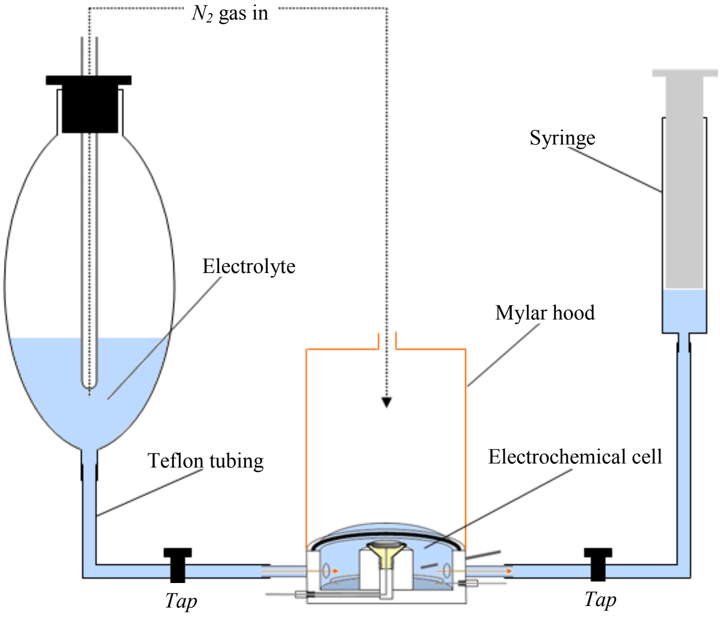

Figure 3.2: Schematic arrangement of experimental setup. The flow of electrolyte through the cell is controlled y the syringe, which is used to collapse the polypropylene film, allowing transmission of x-rays to the surface.

reproducing the expected CV measurements for a particular surface, from a conventional electrochemical cell, x-ray measurements can continue with confidence that the surface is free of impurities. In order to allow x-rays to be transmitted through the electrolyte, the polypropylene film must first be deflated; trapping ∼10 μm of electrolyte above the crystal surface and maintaining potential control. The gas concentrations in and around the cell are controlled by way of a Mylar hood. In most cases nitrogen is used to provide an inert atmosphere inside the hood; however this can easily be exchanged for other gases, such as CO to study carbon monoxide adsorption. The cell components are cleaned in a 50:50 mixture of concentrated sulphuric and nitric acid, then boiled ultra pure water before assembly.

3.4 Instrumentation

Due to the attenuation of the polypropylene film and the layer of liquid over the crystal surface an intense x-ray source, such as a synchrotron, is required to complete experiments. In this section synchrotron radiation and the instrumentation required for an *in-situ* diffraction experiment are described.

3.4.1 Synchrotron Radiation

In the 1970s it was realised that the intensity of x-rays emitted by electrons forced around a curved path of a synchrotron was many times greater than that of standard laboratory sources. Synchrotrons, initially built for high energy physics experiments, made a wide range of x-ray experiments dependent on high intensity radiation possible. Modern third generation synchrotrons, built solely as photon sources, have an x-ray intensity a million million times greater than fixed tube and rotating anode sources. Dedicated synchrotrons continue to be built around the world, due to the success of experiments in a wide range of fields. The experiments detailed in this thesis were completed at the Advanced Photon Source (APS) at the Argonne National Lab (ANL).

In order for the electrons to reach the required relativistic speeds, they are first accelerated in a linear accelerator and then passed into a small circular booster synchrotron. These relativistic electrons are then injected into the main storage ring. Bending magnets (BMs) placed around the storage ring ensure the electrons

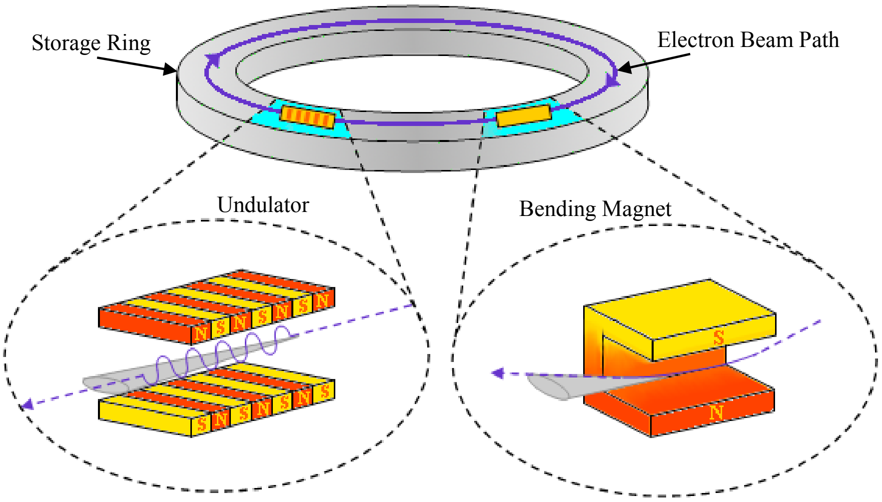

Figure 3.3: Schematic of a synchrotron ring showing an example of an insertion device (ID), the undulator, and a bending magnet (BM). See subsection 3.4.1 for more details.

travel in a circular path. As the electrons pass through bending magnets, their direction of travel changes; causing an emission of Bremsstrahlung radiation in a tangential cone (seen in figure 3.3). In some cases insertion devices (IDs) can be placed in the straight sections of the ring, between bending magnets. The two types of IDs are undulators and wigglers. IDs cause the electron beam to oscillate, as it passes through, by using a row of magnets with alternating polarity. The wiggler produces comparatively large oscillations in the electron beam, resulting in an intense photon beam with a broad energy spectrum. In the case of the undulator the oscillations are smaller and have a frequency such that the emitted photons interfere constructively, giving an extremely intense x-ray beam.

3.4.2 Beamline Setup

While synchrotron produced photon beams are intense, their other main advantage is the broad range of wavelengths available. In most experiments it is necessary to isolate a single wavelength of light from the white beam of synchrotron radiation. This is possible with a monochromator which is a large near perfect single crystal placed in the path of the beam. The monochromator selects the desired wavelength

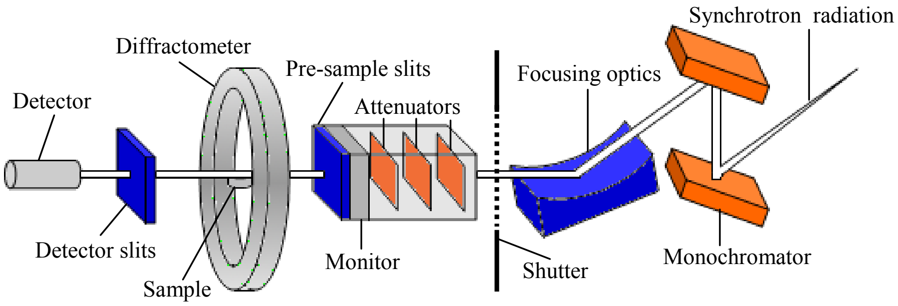

Figure 3.4: Experimental considerations on a typical synchrotron beamline.

by varying the incidence angle in accordance with Braggs law. A good, defect free single crystal is required; silicon is often used as it is relatively cheap. The wavelengths used in the experiments in this thesis is of the order of 1.2 Å(10 keV).

Once the x-ray beam has passed through the monochromator, the focusing optics focus the beam onto the centre of the diffractometer. In order for the incident beam to have the desired properties when it reaches the sample, various issues must first be considered. As the Bragg peaks and the straight through beam are so intense they can damage the detector, attenuators are used to reduce the beam intensity. The material used for attenuators is dependent on the beam energy; however they are typically metal foils of varying thickness, such as Al or Ni. A monitor is used to measure the intensity of the incidence beam as a point of reference for the measured signal. The monitor may be an ion chamber or a Mylar scatter foil, which deflects a fraction of the beam into the monitor detector. The beam than passes through a set of slits which can be adjusted, horizontally or vertically, defining the beam and giving control of the beam footprint on the sample.

The sample is mounted in the centre of the diffractometer which is different depending on the individual beamline. A description of 12-BM-B, the beamline used for the experiments in this thesis, will follow. Once the x-ray beam has been diffracted the signal to noise ratio can be maximised by passing it through an arrangement of detector slits. The slits can also adjust the spectrometer resolution before incidence on the detector. Schematic of a typical synchrotron beamline is shown in figure 3.4.

3.4.2.1 12-BM-B, APS

The 12-BM-B beamline is situated on a bending magnet at the APS, Argonne National Lab. The beamline uses a water-cooled, double bounce monochromator with Si(111) crystals, followed by a double mirror system (flat plus toroidal) focusing the beam at the centre of a 6-circle Huber diffractometer. This arrangement provides an effective working energy of 4.5 to 23 keV, with the ability to go up to 30 keV if using an unfocused beam. A complete description of the beamline can be found in reference [47]. A series of aluminium foil attenuators are used in the typical beamline arrangement. Figure 3.5 shows schematically the main angles of rotation 2θ, θ, χ and ϕ, all of which are set to zero. 2θ and θ control the detector and incident beam angles respectively. The χ circle rotates the sample in the direction perpendicular to the incident beam. The sample is rotated about the surface normal direction using the ϕ circle. A schematic illustration of the four circles used on the APS diffractometer are shown in figure 3.5. The diffracted beam passes through a final set of slits on the detector arm before reaching a 13-element Ge detector.

3.5 Experimental Procedure

In order to perform a successful x-ray diffraction experiment, a well established routine must be followed. The typical steps are detailed in this section in the order that they have been conducted for the experiments in this thesis. Users at all facilities control their experiments using specialist diffractometry software.

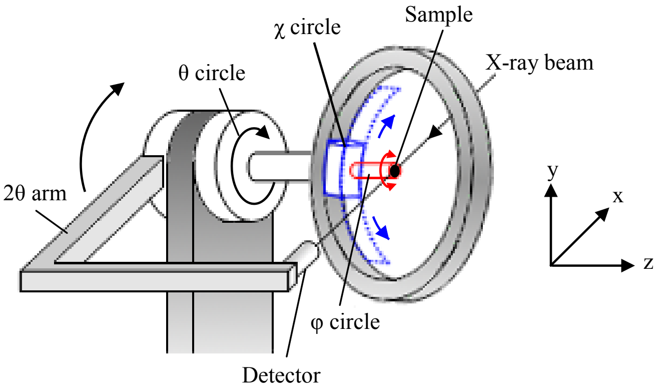

FIGURE 3.5: Schematic illustration of the four circles used on the APS diffractometer.

At the APS the SPEC control program is used which is a UNIX based software package. SPEC allows the user to control various parts of the beamline, including the motors, slit size, attenuation and electrode potential; in addition to being the data acquisition tool [48]. On the APS beamline the diffractometer can be operated in four circle mode using the fourc version of SPEC [49], and it is this mode in which the experiments in this thesis were performed.

3.5.1 Crystal Alignment

The first stage of diffractometer alignment is to ensure that the incident x-ray beam passes through the centre of rotation of the diffractometer. In the case of a four circle diffractometer a specially made pin is mounted on the goniometer. The pin is then rotated in ϕ, while all other motors are fixed at zero, and its position on the goniometer is adjusted until it appears to have no horizontal movement. χ is then rotated from 0^o to 180^o and the z-axis is adjusted until the point of the pin is at the same location for both of these positions. Following this “burn paper” is used to find the location of the beam. The burn paper is placed on the far side of the pin from the incident beam; the diffractometer is then translated until the shadow from the point of the pin is in the centre of the burn from the beam.

Next the 2θ, θ and χ motors must be zeroed. Zeroing the 2θ is achieved using the "straight through" beam. The vertical detector slits are closed so that only a very small gap ($\sim$ 0.1 mm) remains, the 2θ motor is then scanned across the beam (ensuring beforehand that there is sufficient attenuation in place to prevent damage to the detector!); this will give a profile of the beam. The zero for the 2θ motor is then set to the centre of the beam profile. The χ motor can be zeroed simply by using an electronic spirit level. A soller slit is generally used to zero the θ motor. Once mounted, θ is scanned and the centre of the peak intensity is found; the θ motor zero is set to the centre of the peak. Once this is done the diffractometer alignment is complete and the sample can now be mounted.

Once the sample is mounted, crystal alignment can begin. The sample is scanned in the z direction and the z-axis is set to a position where the beam intensity is half that of the straight through beam, which is known as half-cutting the beam. Once SPEC has been provided a real space unit cell and the diffractometer angle positions (2θ, θ, χ and ϕ) for two reciprocal lattice coordinates, typically a specular and non-specular Bragg position, it can relate those angular positions to any other reciprocal lattice coordinate. Therefore the next step is to find the angular positions for two Bragg peaks, which allows the user to work in reciprocal space for the rest of the experiment. A UB matrix is used to relate the real space angle positions to the reciprocal space map, a detailed description of which can be found in reference [50]. Once the sample is aligned the polypropylene film is usually inflated and the system is placed under potential control. To ensure the surface has survived the preparation/transfer process the CV is measured via SPEC and compared to the literature.

3.5.2 Data Acqusition

The most common x-ray measurement is a rocking scan, which refers to the movement of a particular motor while measuring the scattered intensity; the detector is fixed during this scan. A theta rocking scan on at a position on a CTR would start measuring the background scattering on one side of the CTR, pass through the more intense CTR and out into the background on the other side. The first x-ray measurement once alignment is completed is usually a rocking scan through the anti-Bragg position, a position sensitive to the surface occupation, which gives a good indication as to the smoothness of the surface. If a reasonable intensity is observed the surface is smooth enough to proceed with the experiment. XRVs are then taken at various surface sensitive reciprocal positions, usually on the CTRs or reconstruction sensitive positions. These XRVs highlight any structural changes that occur over the potential region of interest. The surface is then characterised with potentiostatic CTR measurements at any potentials of interest.

3.5.2.1 Structure Scans

Scans along the high symmetry $[h00]$, $[0k0]$ and $[00l]$ reciprocal space directions at a small out of plane momentum transfer ($l = 0.15$) can sometimes discover in-plane surface structures, such as reconstructed surface layers or an ordered adsorbate layer. Scattering with different symmetry than the underlying bulk structure can also be observed. An example of this would be CO on Pt(111) where the CO forms a p(2x2) structure, giving rise to a peak at (0.5 0.5 0.15) when scanning along the $[h\ k\ 0.15]$ direction [51]. The coherent domain size (D) can be calculated using the full width half maximum (FWHM), $\Delta\theta$ (in radians), of a theta rocking scan on the structure peak determined by fitting the peak with a lineshape:

$$D = \frac{2\pi}{\Delta\hat{Q}} = \frac{2\pi}{\hat{Q}\Delta\theta} \tag{3.1}$$

where $\hat{Q}$ is the momentum transfer.

3.5.2.2 CTR Measurements

CTRs, which were described in detail in chapter 2, are affected by structural properties of the surface; such as the root-mean-square roughness, surface relaxation and occupation. Due to alignment errors, simply performing a scan in the l direction along the CTR is too inaccurate. Therefore rocking scans are performed at intervals of l along a desired CTR in order to measure it. Once the background x-ray intensity has been removed, the integrated intensity of the rocking scan can be found either by fitting a lineshape or by applying a numerical method. The CTR dataset of integrated intensity as a function of l is produced by repeating this process for each rocking scan along the CTR.

3.5.2.3 Correction Factors

Meaningfully comparing CTR data with theoretical expectations requires that certain correction factors are applied to the raw data, which affect the observed intensity. If the beam footprint has a greater width than the sample diameter at low angles, the low angle area correction must be considered first. The formula for the low angle area correction factor (A) is:

$$A = Rsin\theta_i \tag{3.2}$$

where R is the ratio of crystal diameter and the beam width. θ_i is the angle of incidence and is dependent on whether the scattered beam has an in-plane component to the momentum transfer. For positions on the specular CTR $\theta_i = sin^{-1}\left(\frac{\lambda\hat{Q}}{4\pi}\right)$, whereas for non-specular CTRs $\theta_i = sin^{-1}\left(sin\theta sin\chi\right)$; where θ and χ are the positions of the θ and χ motors, and λ is the wavelength of the incident x-rays. R is a fit parameter varied in the initial fit of a particular sample and held constant for subsequent data analysis.

As the crystal surface is covered with a layer of liquid, an adsorption factor must be used to modify the data. This adsorption factor takes into account the attenuation of the electrolyte and is dependent on the thickness of the liquid layer, which is included as a best fit parameter. Once these modifications have been performed the data is ready to be analysed.

3.5.3 Fit Procedure and Error Analysis

Analysis of the CTR data is performed using the kinematical scattering formalism covered in chapter 2. A least squares method is used to find the best fit to the CTR data, in which the parameters that are varied could include the relative surface occupation (ϵ), the atomic layer expansion(θ) and the individual layer Debye-Waller factor (σ). The variation in integrated intensity of several symmetrically equivalent reflections allows the derivation of the error on the integrated intensity of CTR rocking scans; this is detailed in reference [4]. An example of symmetrically equivalent reflections for a (111) crystal at $l = 1$ (or any other fixed arbitrary value of l) would be the (0 1 1), (1, $\bar{1}$, 1) and ($\bar{1}$ 0 1) positions, which are all equivalent due to the 120^o symmetry of the crystal. The (111) crystal directions are shown in figure 3.6. This error arises from systematic errors such as small misalignments, movement of the beam footprint on the surface, changes in the angle of incidence during large rotations of the sample, etc. To minimise the importance of the systematic errors, the intensities of the equivalent reflections can be averaged; however, due to the nature of synchrotron experiments, taking repeat readings of symmetry equivalents is not always considered an effective use of beamtime. From experience the systematic errors are typically 10%, which are considered dominant over the statistical errors. The statistical errors arise from the counting error on a data point which is taken as $\sqrt{N}$, where N is the number counts observed, and range from a maximum of ~1.5% at the anti-Bragg positions to a minimum of ~0.1% at positions close to Bragg peaks.

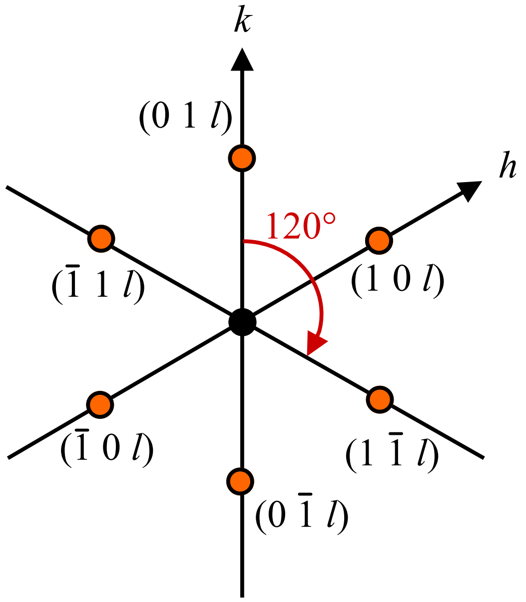

FIGURE 3.6: (111) reciprocal lattice at an arbitrary fixed value of l. The deduced error on a CTR data point is taken from the variance in intensity of symmetry equivalent reflections. The $(1\ 1\ l)$, $(1\ \bar{1}\ l)$ and $(\bar{1}\ 0\ l)$ CTRs are equivalent(as are the $(1\ 0\ l)$, $(0\ \bar{1}\ l)$ and $(\bar{1}\ 1\ l)$ due to the 120° symmetry of the crystal.

3.5.4 Summary

Following the theoretical principles presented in chapter 2, this chapter gave an overview of the considerations involved in completing a successful in-situ diffraction experiment. Adsorption of x-rays in the electrolyte overlayer is the major constraint in studies of this nature, and the required intense x-ray intensity to perform the experiments in this thesis could only be provided by a synchrotron radiation facility. In order for these experiments to be completed, potential control must be maintained and the electrolyte thickness must be minimised, which can be achieved using a purpose built electrochemical cell. Liquid contact to the back and sides of the cell and diffusion problems, due to the x-ray electrochemical cell geometry, can cause reliability issues with the EC measurements. In order to overcome this problem, the features from the x-ray electrochemical cell CV are compared to the features from a CV taken in a conventional electrochemical cell; if they are the same the system is considered to be behaving.

Chapter 4

The Oxidation of Platinum (111)

4.1 Introduction

In this chapter a study of the structure and morphology of the Pt(111) surface during oxidation, induced by the applied electrochemical potential, is described. In the operation of a hydrogen fuel cell the cathode material (typically Pt nanoparticles) will be subjected to potentials between 0.4 (full power) and 0.8 V (standby open circuit potential) for a platinum based cathode. Transient exposure to potentials higher than the OCP can occur during certain conditions such as start/stop conditions while an exposure to potentials lower than 0.4 bears a more fundamental than practical significance. Herein, however, we will only focus on the potential window from 0.4 to 1.1 V. In this way, we capture the potentials of normal operating conditions as well as part of the potential window positive of OCP. Potentials up to 1.3 V can be observed during start-up/shut down conditions but those are more detrimental to the catalyst support then to the catalyst itself.

It is possible to tailor Pt nanoparticles by using different methods of production, leading to nanoparticles of different shapes with low index faces[52] or even high index faces[53]. This allows the catalytic properties of the nanoparticles to be altered. Electrochemical studies of the ORR on Pt(111) in various solutions[54, 55] have shown the (111) face to be the most active low index surface. Nanoparticles such as these can be used as high surface area fuel cell catalysts, however they lose their electrochemical surface area while operating[56]. One of the main reasons for this surface area loss is sintering and agglomeration of the Pt nanoparticles. Xu *et al.* [57] saw a similar effect during *in-situ* STM experiments on thin films of platinum deposited on glassy carbon, in which the potential induced growth of platinum islands was seen. The growth of these islands was most likely caused by the diffusion of platinum adatoms from smaller to larger islands, with the maximum island size seen being ∼100 nm.

Numerous experiments in UHV have been performed to study the effects of oxygen on the Pt(111) surface in the past four decades. EELS (Electron Energy Loss Spectroscopy) measurements taken at <120 K have shown molecular oxygen adsorption on the Pt(111) surface, with Thermal Desorption Spectroscopes showing the coverage to be 0.5 ML [58, 59]. STM studies have shown that molecular oxygen can be broken down into atomic oxygen using UV irradiation, in addition the atomic oxygen was found in fcc and hcp sites [60]. LEED experiments have shown that atomic oxygen bonds to the surface with (2 x 2) structure, forming at low coverages which indicates an island growth mechanism and therefore long-range effects on the electronic structure of the surface [58]. Studies where the oxide is formed by atomic oxygen adsorption have shown a p(2 x 2) structure forms at a coverage of up to 0.25 O molecules per Pt surface atom, with 0.25 being the absolute saturation coverage for a perfect (2 x 2) layer [61]. Increasing the oxygen coverage decreases the surface order, although the (2 x 2) pattern remains between 0.25 ML and 0.50 ML; consistent with a different high-density phase. Disordering of the chemisorbed layer becomes more pronounced as surface oxygen coverage increases above 0.50 ML and it has been postulated that this is caused by formation of oxide particulates on the surface [62, 63]. At coverages between 0.25 and 0.5 monolayers it has been shown, by using different oxygen isotopes, that exchanges occur between multiple adsorption sites [64]. Coverages up to 0.75 have been achieved by NO_2 exposure at 400 K, giving results consistent with atomic oxygen adsorption [65]. Ozone (O_3) has been used to achieve coverages up to 2.4 ML, for which temperature programmed desorption (TPD) saw an increasing desorption activation energy at coverages $>$1.2 ML; most probably arising from decomposition of platinum oxide particles [66]. Heating to 900 K during exposure to oxygen causes an oxide to form, which is a single chemical species and decomposes at temperatures of 1250 K and above [58].

In-situ x-ray experiments on the Pt/Rh(111) surface, a well defined Pt monolayer system, have shown that there is a low coverage of oxygen for potentials below 1.0 V vs. RHE and oxide formation above this potential [67]. H. You *et al.* [68] performed *in-situ* x-ray diffraction experiments measuring the structure of the oxide on Pt(111) between 1.025 V and 1.175 V and found that a place exchange of the oxygen and a fraction of the atoms in the top Pt monolayer accurately modelled the CTR data. In addition, above the critical charge transfer of 1.7 e^{-}/Pt atom irreversible roughening was seen. This charge transfer threshold equates to about 1.25 V vs. RHE. *In-situ* STM measurements have shown that the Pt(111) surface will oxidise and roughen at lower potentials (OH adsorption region between 600 mV and 850 mV vs. RHE) if cycled in an environment in which oxygen is present [69]. Ellinger *et al.* showed that oxidation of a Pt(111) crystal in a partial pressure of 500 mbar at temperatures from 520 to 910 K, resulted in two atomic layers of distorted, bulk-like α-PtO_2 [70].

Platinum and platinum based alloys in electrochemical environments display a common response within a well defined potential window. The negative boundary of this window is the point at which hydrogen evolution begins, which is generally around -200 mV. Potential dependent X-ray diffraction measurements below this potential are impossible in thin layer cell as the build up of hydrogen gas between the crystal surface and the polypropylene film forces the electrolyte away from the crystal surface, stopping any potential control. Positive of this negative limit is the hydrogen adsorption region, the size of which is dependent on the surface geometry

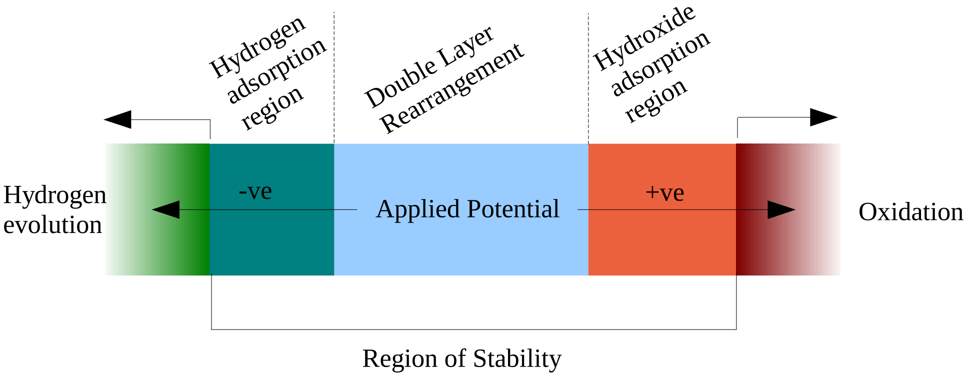

Figure 4.1: The potential dependent regions common to most platinum surfaces, showing the region of stability. Below the negative limit of stability is the hydrogen evolution region then, heading more positive, are the Hydrogen adsorption region, the region of double layer rearrangement and the hydroxide adsorption region. Finally beyond the positive limit of stability is the oxidation region. The three phases of the region of stability can be clearly seen in the CV in figure 4.3

and chemistry, in addition to the electrolyte used. In the centre of the window is the double layer region where very small current features can sometimes be seen due to double layer rearrangement of anions and/or cations. Heading towards the positive end of the window is the hydroxide adsorption region where OH^- is dissociated from water molecules in the solution and bonds to the surface. This process can be seen as charge transfer peaks in the cyclic voltammetry. Beyond the positive limit of the window of stability is the oxidation region (see figure 4.1). Oxidation of platinum surfaces causes irreversible roughening, in most cases causing a loss of reactivity. The region bounded by the evolution of hydrogen and the oxidation for the surface is known as the window of stability.

The experiments in this chapter begin with XRV measurements inside the window of stability (-200 mV to 600 mV), which were taken at surface sensitive positions. A set of symmetrically inequivalent CTR data in the hydrogen adsorption region was taken. Afterwards the sample was oxidised during an XRV measurement, from

-200 mV to +1100 mV, taken at the specular anti-Bragg position; the measurement of the intensity was continued until it became stable. The oxide was then characterised with a set of CTR measurements which showed a markedly different structure to that seen in the reversible oxide region. A further XRV measurement was taken during reduction of the oxide and the CTR data of the reduced surface clearly show irreversible roughening. After re-preparation the crystal was then cycled multiple times into the oxide region after which STM measurements show the formation of ordered platinum islands appearing as “fish scales” in STM images. X-ray measurements were taken and confirm the long range order and domain size, as well as the island height.

In addition, complimentary *ex-situ* STM measurements have been performed separately. Starting with the as prepared surface the potential was cycled in the range of -150 mV to -800 mV, after which the STM measurement was taken. The process was repeated after expanding the potential window, first to 900 mV and then to 1100 mV.

4.2 Pt(111) Surface Characterisation

The Pt(111) crystal was annealed to a temperature of 1000 °C in a 97% Ar_2 and 3% H_2 atmosphere. The crystal was heated for 7 minutes and then left to cool for an additional 7 minutes. This preparation method is described in detail in reference [71] and has been shown to give good quality (111) surfaces with large (111) terraces for certain noble metals, including gold and platinum. After preparation, the crystal was transferred to the electrochemical cell, with a drop of deionised water placed on the crystal to shield the surface from contamination during transfer. After mounting the cell on the diffractometer, potential contact was made at -200 mV. The crystal was then aligned using the method described in subsection 3.5.1.

The large scale (100x100 nm) STM image of pristine Pt(111) displays the presence of a few randomly distributed monoatomic steps and two dimensional (2D) Pt islands with diameters of 1-2 nm (figure 4.2). The voltammogram of a freshly prepared surface exhibits three distinct potential regions representing hydrogen upd adsorption/desorption, double layer charging and OH adsorption (figure 4.3). After exposure to potentials below 0.75 V the STM image remains the same, indicating that within this potential region the morphology of Pt(111) surface is stable.

In order to measure the level of dissolution of platinum into the solution, Inductively Coupled Plasma Mass Spectrometry (ICP-MS) analysis of the electrolyte was performed. In this process an excess electrons are introduced to a stream of argon gas which is then is heated using an induction coil to the point of ionisation, forming an extreme temperature plasma torch, i.e. 10,000 K. When a droplet of electrolyte is introduced to the torch it vaporises, breaking down into atoms; a significant percentage of which are ionised. The argon flow then carries the ionised electrolyte into a mass spectrometer, where it can be analysed. In this case no measurable amount of Pt was found in the solution, indicating that no dissolution took place within the above mentioned potential limits.

The first stage of the x-ray diffraction experiment was to characterise the Pt(111) surface in 0.1 M $HClO_4$ in the region of stability. In the case of Pt(111) there is an expansion in the hydrogen region at <200 mV. To monitor this expansion the potential cycled from -200 mV to 600 mV at 5 mV s^{-1} during an XRV measurement was performed at the reciprocal lattice position (1 0 3.6), a position sensitive to surface relaxation. The XRV was background subtracted by fitting the rocking scan at this position with a Voigt function and a linear background. The linear background was then subtracted from the XRV intensity. The XRV was then normalised so the intensity of the first point at the negative limit is one (the top plot in Figure 4.4). The beauty of such a measurement is that it gives a good insight into the kinetics of a system. In this case there is a great deal of hysteresis

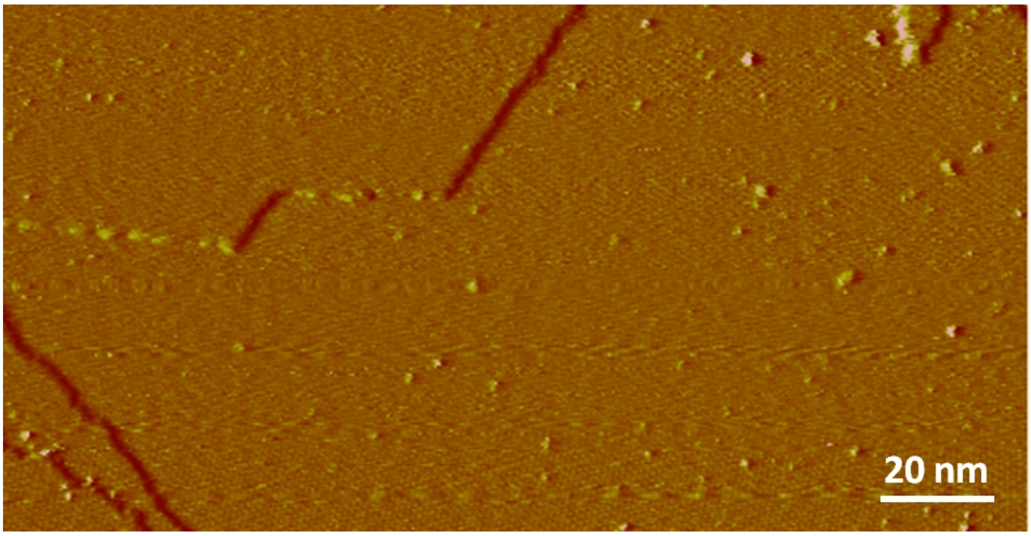

Figure 4.2: STM image of the as prepared Pt(111) surface after UHV preparation, the surface shows large terraces and few step edges.

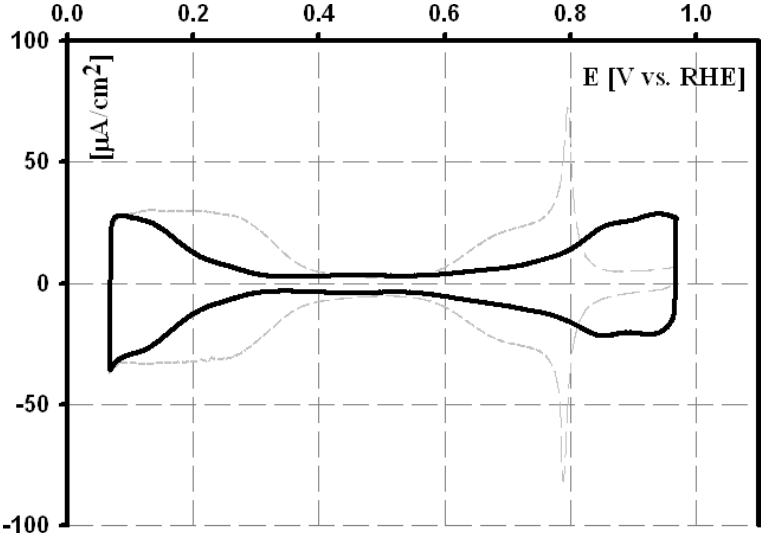

Figure 4.3: The black line shows cyclic Voltammetry measurement of the Pt(111) surface in 0.1 M $HClO_4$ solution between -150 mV and 780 mV vs Ag/AgCl$^-$. Three distinct potential regions can be seen representing, from negative to positive, hydrogen upd adsorption/desorption, double layer charging and OH adsorption.

which is not seen in similar systems, such as Pt(111) in KOH solution, which would indicate the kinetics in $HClO_4$ are slower.

The bottom plot in figure 4.4 are XRVs measured two other surface sensitive positions, the off-specular (0 1 0.4) and the specular (0 0 1.52), using the same potential limits and rate as the previous XRV. These are anti-Bragg positions and, as such, are sensitive to surface occupation. These XRVs have been normalised so that the maximum intensity of each plot is one, in addition the vertical axis for the XRV at (0 1 0.4) has been moved to the right axis for clarity. A fairly linear decrease in the intensity with increasing potential is seen at the specular anti-Bragg position (0 0 1.52) while the inverse is seen at the non-specular position (0 1 0.4) where the intensity increases with potential. It is also worth noting there is little hysteresis in these XRVs when compared to the expansion, suggesting that the kinetics of this change in structure causing the difference in intensity is much faster.

The crystal was held at -200 mV and a set of symmetrically inequivalent CTR measurements (the (1 0 L), (0 1 L) and (0 0 L) rods) was taken to characterise the surface. The CTR data were fit using a three layer model, although only the surface layer showed any marked difference to the bulk. The fit is an ideal termination with a 2.4% expansion of the surface layer. This measurement is consistent with previous measurements of a Pt(111) crystal in the hydrogen adsorption region [10]. Figure 4.5 shows the CTR data as circles with error bars. The solid line shows the best fit to the data. This fit was achieved by varying the fit parameters using a least squared method. Table 4.1 shows the best fit parameters.

4.3 Oxidation of Pt(111)

Upon potential excursions positive of 750 mV, the first morphological changes on the Pt(111) surface were observed in the STM images. It seems that a gradual

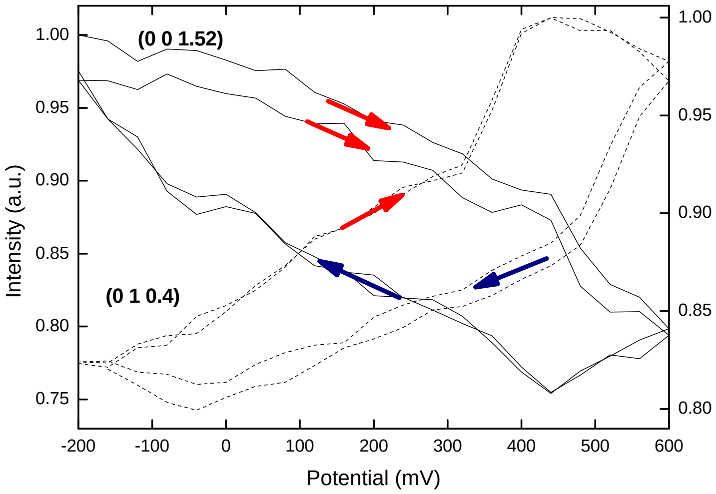

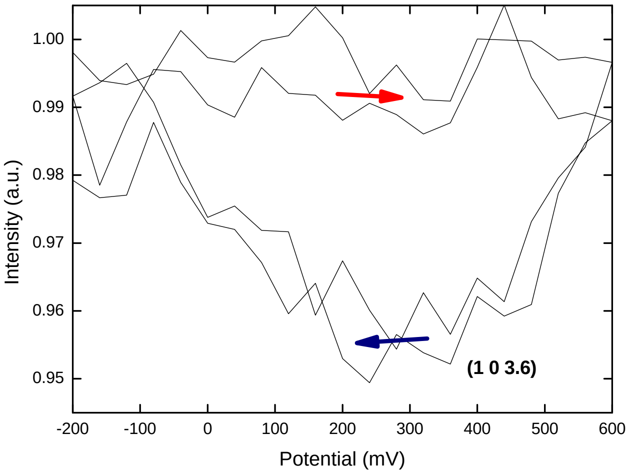

Figure 4.4: Top: XRV measured at the relaxation sensitive position (1 0 3.6), the potential was cycled between -200 mV and 600 mV at 5 mV s^{-1}. Bottom: The solid line shows an XRV taken at the specular anti-Bragg position (0 0 1.52) and the dashed line shows an XRV taken at the off-specular anti-Bragg position (0 1 0.4). The XRV taken at (0 0 1.52) is plotted against the left y-axis and the XRV taken at (0 1 0.4) is plotted on the right y-axis for clarity.

Layer	Occupation	Relaxation	Debeye-Waller Factor
1^{st} (Top)	1.00 ± 0.04	0.003 ± 0.003	0.00 ± 0.08
2^{nd}	1.00 ± 0.03	0.006 ± 0.003	0.00 ± 0.07
3^{rd}	1.00 ± 0.03	0.000 ± 0.003	0.00 ± 0.07

Table 4.1: Best fit parameters obtained from analysis of CTR data taken at -200 mV. The fit parameters deduced for the surface atomic layer expansion, relative surface coverage and surface roughness are shown along with their associated error.

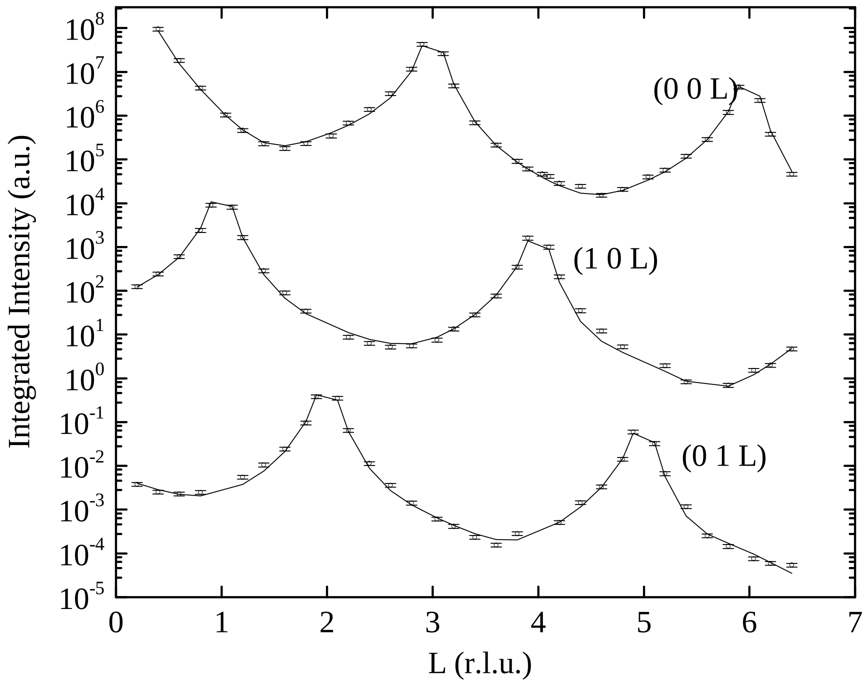

FIGURE 4.5: The (0 1 L), (1 0 L) and (0 0 L) CTRs measured at -0.2 V for the as-prepared surface. The solid line is a fit to the data. The χ_v^2 for this fit was 1.84.

corrugation of steps occurs as the potential window is opened towards the oxide region. The surface changes are clearly seen in the STM image in figure 4.6. ICP-MS analysis of the solution showed traces of platinum pointing to the start of the dissolution of the noble metal.

Continuing the SXS experiment, after measuring the clean surface the potential was scanned from -200 mV to 1100 mV at 5 mV s^{-1}. The sample was then held at 1100 mV, well into the oxidation region. Figure 4.7 shows the x-ray intensity measured at (0 0 1.55), a position sensitive to surface roughness, during this potential scan.

The sharp drop in intensity occurs at ∼900 mV, indicating a roughening as oxidation begins. The surface seems to begin to flatten over a longer period, eventually stabilising ∼2000 s after oxidation begins. A full CTR data set was measured at 1100 mV after the surface had stabilised. In order to fit the data it was necessary

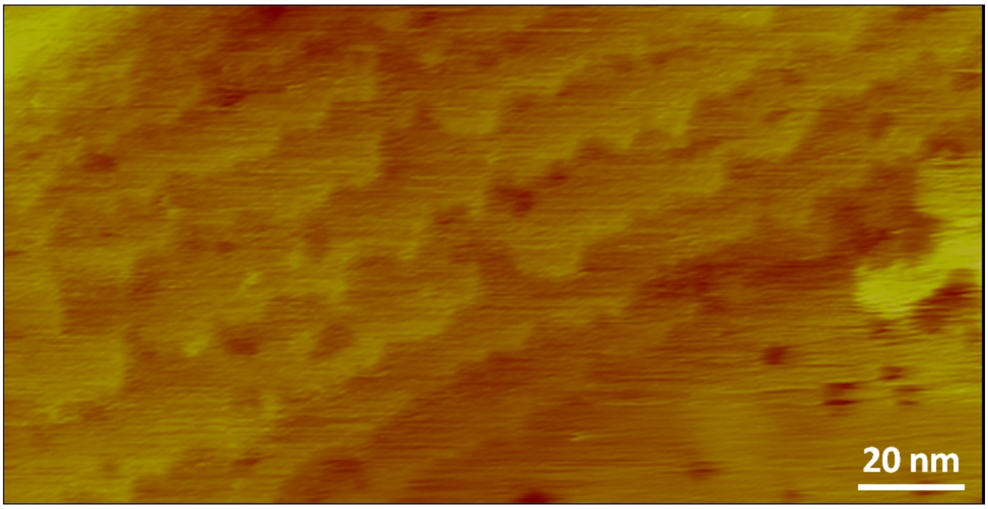

FIGURE 4.6: STM image of the Pt(111) surface after cycling to 900 mV showing a roughening of the surface, along with step formation, when compared the STM of the as-prepared Pt(111) surface shown in figure 4.2

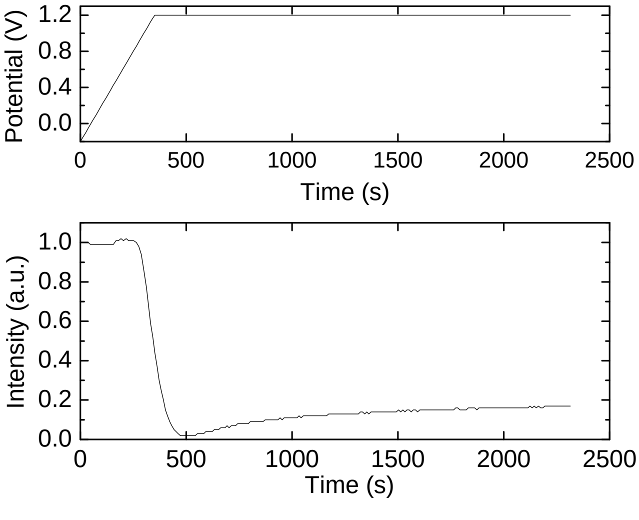

FIGURE 4.7: X-ray intensity measured at the specular anti-Bragg position (0 0 1.55), during a potential scan from -200 mV to +1100 mV at 5 mV s^{-1}; and for ∼2000 s after the scan finished. This scan reveals the slow kinetics of oxide formation on Pt(111).

Layer	Occupation	Relaxation	Debeye-Waller Factor
1^{st}a (Top - buckled)	0.18 ± 0.03	0.094 ± 0.006	0.00 ± 0.18
1^{st}b (Top)	0.49 ± 0.03	-0.012 ± 0.001	0.00 ± 0.11
2^{nd}	0.94 ± 0.03	0.009 ± 0.002	0.00 ± 0.07
3^{rd}	1.00 ± 0.03	0.004 ± 0.001	0.00 ± 0.06

Table 4.2: Best fit parameters obtained from analysis of CTR data taken at +1100 mV. The fit parameters deduced for the surface atomic layer expansion, relative surface coverage and surface roughness are shown along with their associated error. The buckled top layer has been separated into two layers.

to use separate fits for the specular and non-specular CTR data, which indicates it is likely that the oxide is an ordered incommensurate structure or lacks long range order. Previous LEED studies of the oxide structure in UHV, where the oxide is formed by atomic oxygen adsorption [62, 63], have shown that increasing the oxygen concentration decreases the surface order and it was postulated that this was due to the formation of oxide particulates on the surface. X-ray measurements taken in HK directions at low L were inconclusive as they did not show any signs of either an incommensurate structure or any powder diffraction from an oxide. DFT studies have shown that the top monolayer forms a buckled Pt layer, the magnitude of the buckling depends on whether the oxygen is surface or sub-surface with surface oxygen causing a much greater buckling [72]. In addition, neither this x-ray data nor DFT support a place exchange model. The specular oxide data was fit to a buckled Pt surface layer model, the buckling was 0.75 ± 0.13 Åwhich agrees well with the sub surface model (0.73 Å). The sub surface oxygen was not included in the model as its contribution is negligible. Table 4.2 shows the best fit parameters for the fit to the oxide data.

The model also shows that a degree of roughening has occurred during the oxidation process. This roughening is caused by dissolution of platinum atoms (seen in ICP-MS analysis), platinum mobility on the surface, or more likely a combination of the two effects. This causes a drop in occupation in the second layer to 0.94 and a total drop of 0.67 in the first layer when including both the buckled and unbuckled platinum atoms. The fit to the CTR data also reveals a expansion of

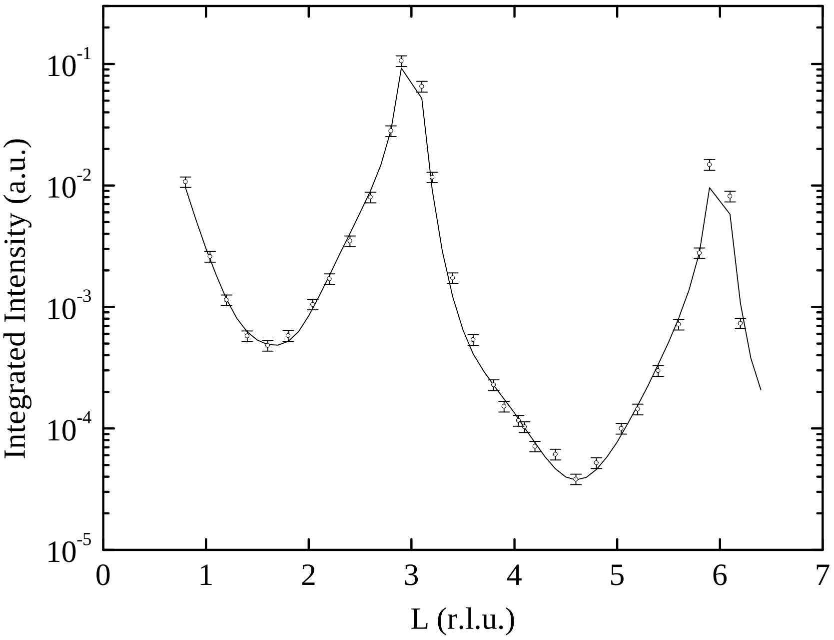

FIGURE 4.8: The (0 0 L) CTR measured at 1.1 V. The solid line is a fit to the data and the χ^2 for this fit was 1.82.

0.9 ± 0.2 % of the second layer and an inward relaxation of 1.2 ± 0.1 % of the top layer. The surface was then reduced by a cathodic sweep to -200 mV at a rate of 5 mV s^{-1}. During this negative sweep the x-ray scattering intensity was monitored at the anti-Bragg position (0 1 0.2) and is shown in figure 4.9.

The oxide appears to be stable down to a potential of ∼600 mV after which point the intensity peaks and then falls off rapidly as the surface is reduced. Following this a quick recovery of the intensity was seen. These features are likely to be due to the dissolution of platinum oxide particulates, followed by a partial redeposition of the Pt surface layer. CTR measurements of the reduced surface were taken and a β factor (described in section 2.4) of 0.41 ± 0.06 was used to model the surface. The combination of little additional roughening and the sharp drop and recovery of the surface occupation during reduction would indicate that the reduction of the oxide causes disruption in the platinum lattice.

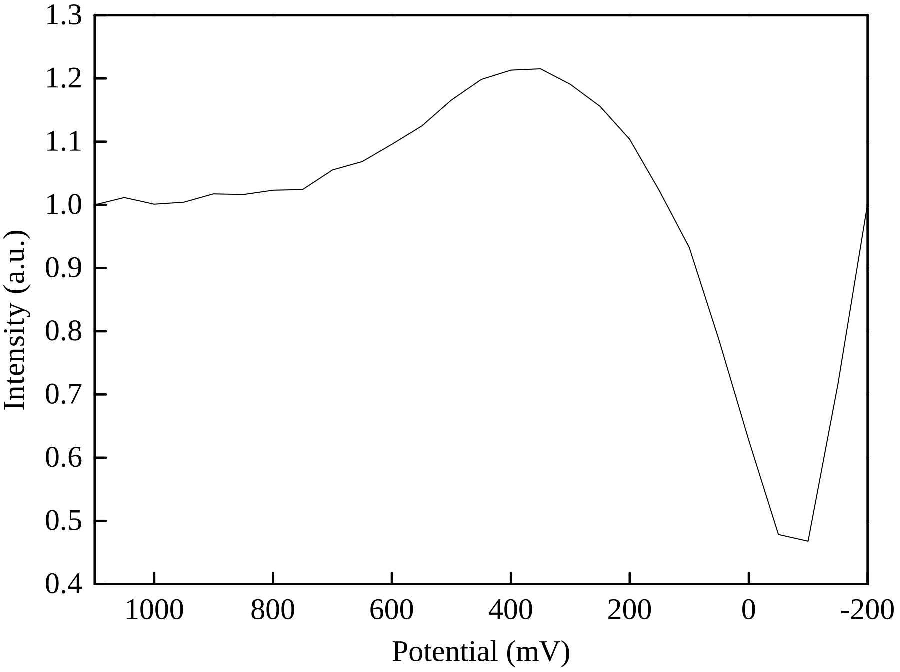

FIGURE 4.9: Intensity measured at the (0 1 0.2) anti-Bragg position during oxide reduction. The intensity at this position gives an indication of the surface roughness, showing that the oxide appears to be stable to potentials as low as ∼600 mV.

4.4 The Effect of Cycling into the Oxide Region on the Pt(111) Surface

The Pt(111) crystal was reprepared and checked using the methods described in the Surface Characterisation (4.2) section of this chapter. In this experiment the polypropylene film was raised and the potential was cycled from -0.2 V to 1.1 V at a sweep rate of 50 mV s^{-1} for 100 potential cycles. Once the cycling was complete the potential was held at -200 mV. CTR measurements were taken of the (0 0 L), (1 0 L) and (0 1 L) rods. When beginning to take these measurements it quickly became apparent that a modified rocking scan would be required as they showed a two component lineshape, in contrast to the sharp component lineshape observed for the clean surface. The anti-Bragg positions of the CTR dropped in intensity at

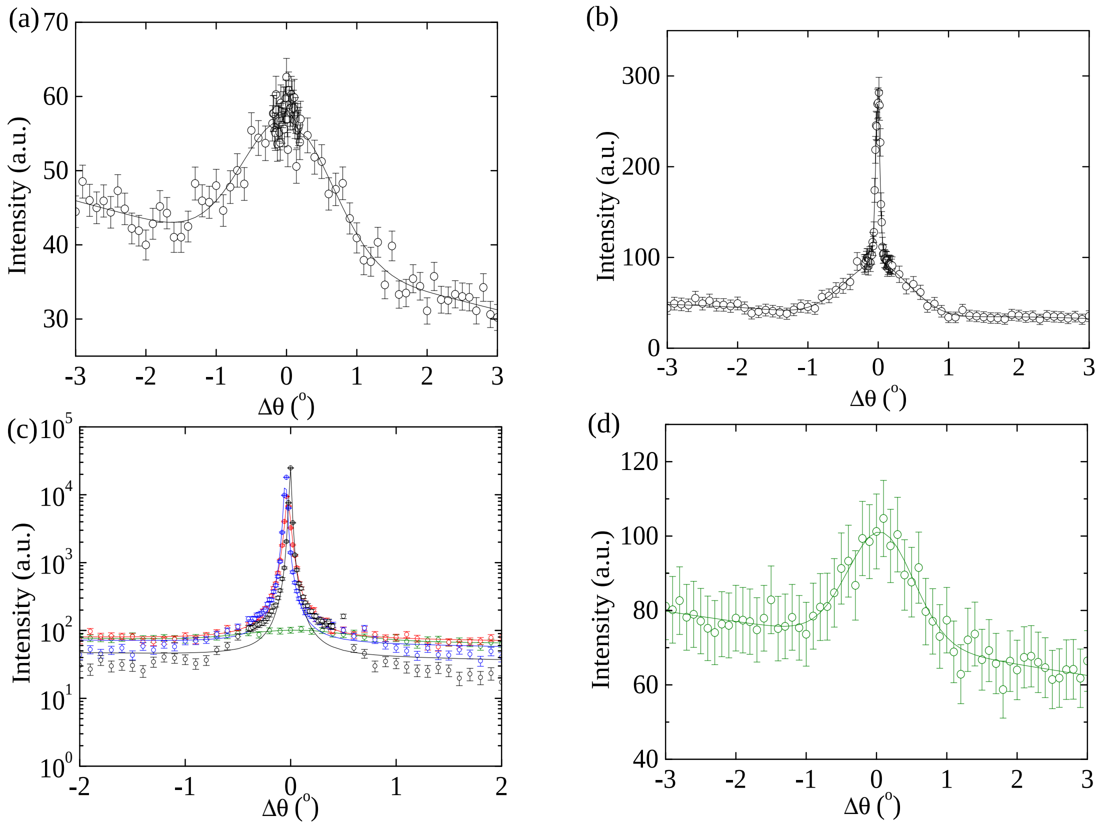

FIGURE 4.10: Rocking scans of the (0 0 2.2), (0 0 2.6), (0 1 0.6) and (0 1 0.6); showing broad and diffuse lineshape components. Red - Clean surface; Black - held at 1100 mV; Blue - After reduction to -200 mV; Green - After 100 cycles over the range -200 mV to 1100 mV. For clarity the scan after 100 cycles over the range -200 mV to 1100 mV has been plotted separately, as its intensity is far lower than that of the clean surface.

least two orders of magnitude when compared with the clean surface, consistent with considerable surface roughening. Figures 4.9a and 4.9b illustrate the two component lineshape showing two measurements at positions on the specular CTR after potential cycling which indicates the presence of both a sharp component and a broad component.

At the anti-Bragg position the sharp component has completely disappeared as indicated by the results in Figure 4.10c which show measurements close to the anti-Bragg position of the non-specular CTR, (0 1 0.6), obtained under four different conditions. The colour code is Red - Clean surface; Black - held at 1100 mV; Blue - After reduction to -200 mV; Green - After 100 cycles over the range -200 mV

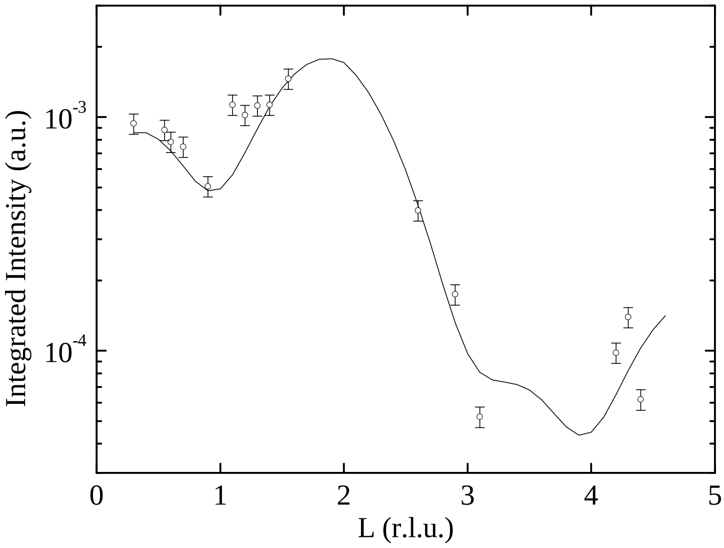

FIGURE 4.11: Broad component of the (0 1 L) CTR of the cycled surface, the line is the three atomic layer fit. This shows that the Pt adislands present on the cycled surface are crystalline to a depth of 3 atomic layers.

to 1100 mV. The result obtained after cycling is enlarged in figure 4.9d where it can be seen that the scattering is entirely diffuse in nature, i.e. there is no sharp component to the lineshape. Fits to the data are shown by the solid lines and correspond to a Voigt lineshape from which the coherence length can be obtained. The fits to both the specular CTR profiles and the non-specular position give a consistent domain size for the broad component that is 60 ± 11 Å. This compares to the domain size obtained from the sharp component which is in the range 1000 ± 200 Å. The measurements for the cycled surface indicate that there has been significant surface restructuring and recrystallization and that there is now a Pt surface layer that has only short range order (6 nm).

The non-specular CTR's measured from this surface (data not shown) were modelled using the β model of roughness. The best fit is given by a β factor of 0.8 ± 0.2 which corresponds to an rms roughness of 5 ± 1 Å. Estimates from the β model suggest that the surface roughness it is in the range of 4-6 Pt(111) lattice spacings, (10-15 Å). The results imply that during cycling there is either continuous dissolution and regrowth or movement of the Pt lattice with a limited diffusion length over which long-range order can be maintained (hence the domain size of 6 nm).

The sharp and diffuse component of each rocking scan, such as in figures 4.10, were fit with Voigt functions from which the integrated intensity of each diffuse component was calculated. The l dependence of the diffuse component of rocking scans along the $(0\ 1\ l)$ CTR is shown in figure 4.11. The $(0\ 1\ l)$ rod was chosen as it had the greatest number of scans with measurable diffuse components. As the diffuse component is solely the result of diffraction from surface domains with long range order, the bulk crystal is not included in the model used to fit this data. Two, three and four atomic layer models were used to fit the data, with the three atomic layer model providing the best fit, which is shown as the solid line in figure 4.11.

Upon opening the positive potential limit to 0.95 V, corrugation of steps as well as significant increase in the adisland density is observed in the STM. Finally at 1100 mV, the surface transforms into a two-dimensional semi-ordered array of adislands (Figure 4.12) with a diameter of ∼6 nm which is in good agreement with the x-ray data.

4.5 Summary

The Pt(111)-electrolyte interface has been characterised using surface x-ray diffraction techniques both in the potential range of OH adsorption (which indicates the surface is stable) and into the potential range of oxide formation (which leads to irreversible restructuring of the surface). XRV measurements indicate that the surface undergoes reversible changes in surface structure in the potential region of stability. A surface expansion of 2.4 ± 0.4 % was measured in the hydrogen region,

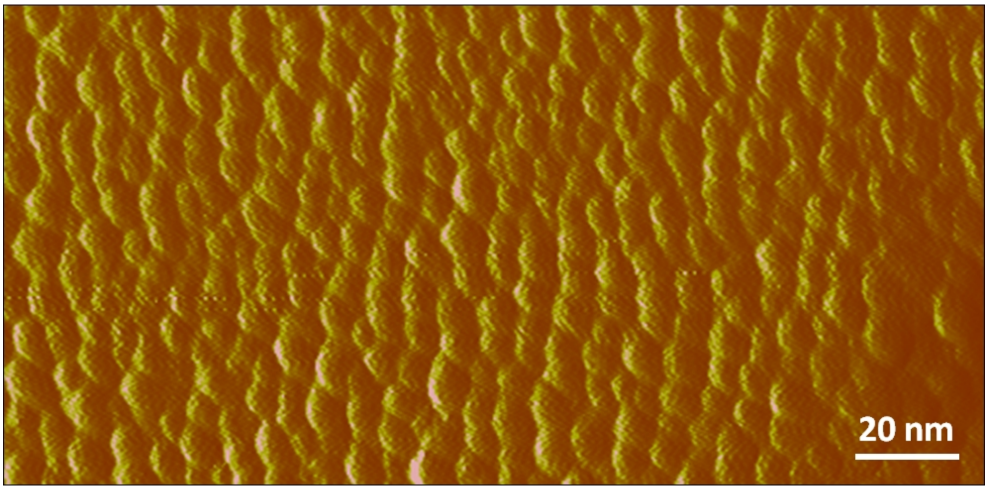

FIGURE 4.12: STM image of the Pt(111) surface after cycling to 1100 mV 100 times, clearly showing the Pt adislands with an equivalent domain size to that was seen with SXS.

along with a change in surface occupation across this entire potential range. During oxidation a sharp drop of intensity, indicating roughening, was seen to begin at 900 mV. A set of CTR data in the oxide region showed the oxide was incommensurate and scans along high symmetry directions revealed no superstructure peaks, showing that the oxide had no long range order. The specular CTR data was modelled by a buckled surface layer with a d-spacing of 0.75 ± 0.13 Åalong the surface normal, agreeing well with DTF models for Pt(111) with sub-surface oxygen. The CTR measurements were taken again after oxide reduction, and the data were consistent with an irreversible roughening of the surface.

The effects of repetitive cycling into the oxide region were also studied. The Pt(111) surface was cycled into the oxide region 100 times. Rocking scans at various positions along the CTRs showed a two component lineshape, with the new broad component caused by structures with short range order on the surface. The x-ray intensity at the anti-Bragg position decreased by two orders of magnitude, consistent with considerable surface roughening. The fits to the broad components of individual rocking scans gave a consistent domain size of 60 ± 11 Å, which agrees well with the STM data, and showed dramatic Pt surface restructuring and the formation of a ”fishscale“ pattern, i.e. a pattern of evenly sized platelets. A fit to the broad component of the (0 1 L) CTR indicated that the 60 Å platelets were crystalline to a depth of 3 atomic layers.

The results presented in this chapter are for the close packed (111) surface. To get further insight into the mechanism of Pt surface oxidation it is necessary to explore the dependence on the surface geometry. In the next chapter a similar study of the Pt(100) surface is presented.

Chapter 5

The Oxidation of Platinum (100)

5.1 Introduction

It has been recently shown that Pt nanocubes can be synthesised [73], which expose predominately (100) faces and are more active in acidic solution with regards to the ORR [74, 75]. Furthermore, it is instructive to examine electro-oxidation of the Pt(100) surface for comparison with the Pt(111) surface. Measurements using a Field Ion Microscope in UHV have shown that Pt atoms migrate on the Pt(100) surface exclusively along the [100] and [010] directions, which proceeds by a concerted-displacement mechanism in the temperature range from 170 to 205 K [76]. UPS experiments have shown that oxygen changes the surface electronic structure of Pt(100)(1 x 1), increasing the work function from 5.92 eV to 7.11 eV on the oxide surface [77]. At temperatures below 600 to 700 K platinum forms only one monolayer of oxide and Pt(100) was measured to be more resistant than Pt(111) to surface diffusion of oxide; surface oxides of more than a monolayer in thickness were produced above 700 K [78]. Pt(100) has a reconstructed hexagonal phase when dosed with hydrogen in UHV environment. In fact the Pt(100)(1 x 1) unreconstructed surface has been shown to be very reactive, with hydrogen contamination increasing at 1% of a monolayer every seven minutes; and the reconstruction occurring with less than 10% of a monolayer at 370 K [79]. A high-energy resolution core level photoemission study has shown that the activation energy of the phase transformation from Pt(100)(1 x 1) to Pt(100)-hex is 0.76 eV [80].

Electrochemistry studies on the Pt(111) and Pt(100) surfaces in H_2SO_4 have shown (100) to be more active with regards to the oxygen reduction reaction [81], whereas in KOH solutions the (100) surface was measured to be less active than the (111) surface; likely due to OH^- adsorption blocking oxygen adsorption sites [82]. The hydrogen oxidation reaction has also been studied in $HClO_4$, where hydrogen adsorption was seen to continue into the hydrogen evolution region and the adsorbed hydrogen did not have any role in the evolution process [83]. In the case of $HClO_4$ solution, the crystal orientation has been show to make little difference to the ORR rate [84]. Cyclic voltammetry experiments in alkaline solution have shown that the gas mixture which the Pt(100) surface is cooled in after annealing affects the quality of the surface, with argon-hydrogen or carbon monoxide-argon mixes giving the best long range (1 x 1) order [85].

Ex-situ electrochemistry and LEED studies have been performed in which the Pt(100) surface was cycled to various potentials, showing increasing roughening of the surface as the postive limit of the cycling increased [86]. A combined electrochemical, LEED, RHEED and AES study has shown that the Pt(100)-hex phase is stable up to 0.9 V in 0.01 M $HClO_4$ and the reconstruction is not uniformly lifted above this potential in this solution [87].

The experiments in this chapter begin with XRV measurements taken in the region of potential stability (-200 mV to +600 mV) at surface sensitive positions. A set of symmetrically inequivalent CTR data at the negative and positive limits of this region were taken. Afterwards the sample was oxidised by way of an anodic sweep from -200 mV to +1100 mV, with the x-ray intensity monitored at the (1 1 2.1) anti-Bragg position until it became stable. The oxide was then characterised with a set of CTR measurements which showed a similar structure of oxide particulates as seen on Pt(111). The oxide was reduced during a cathodic sweep from 1100 mV to -200 mV, with the x-ray intensity measured at the (0 0 1) anti-Bragg position. CTR measurements of the reduced surface show irreversible roughening which was modelled with a β factor. After re-preparation the crystal was cycled multiple times into the oxide region which, unlike Pt(111), caused catastrophic roughening rather than the formation of platinum islands.

5.2 Surface Characterisation

Figure (5.1) shows XRVs taken at two positions sensitive to surface relaxation, (1 1 2.7) and (1 1 3.3), cycled in the potential range -200 mV and 600 mV at 5 mVs^{-1}. This region is chosen as it highlights any expansion during hydrogen adsorption. The XRVs were background subtracted by fitting a rocking scan at each of these positions with a Voigt function and a linear background. XRVs have been normalised so the intensity of the most intense point in each scan equals one. A clear expansion in the hydrogen region is seen with a sharp increase and decrease in intensity of the (1 1 3.3) and (1 1 2.7) XRVs respectively, on the anodic sweep. No hysteresis is seen on the cathodic sweep, unlike the similar relaxation seen on Pt(111). Figure 5.2 shows an XRV at the anti-Bragg position (1 1 2.1), which is sensitive to the commensurate surface occupation of OH^{-}, cycled in the same range of -200 mV and 600 mV at 5 mVs^{-1}. The scan was background subtracted and normalised using the same method as the previous XRVs; it showed no measurable change.

To characterise the relaxation, the potential was set to -200 mV, a potential in the hydrogen adsorption region, and a CTR dataset was taken for both the (0 0 L) and (1 1 L) rods. These CTRs were fit using a 3 layer model which allows variation of the 3 topmost atomic layers, the fit parameters are shown in table 5.1

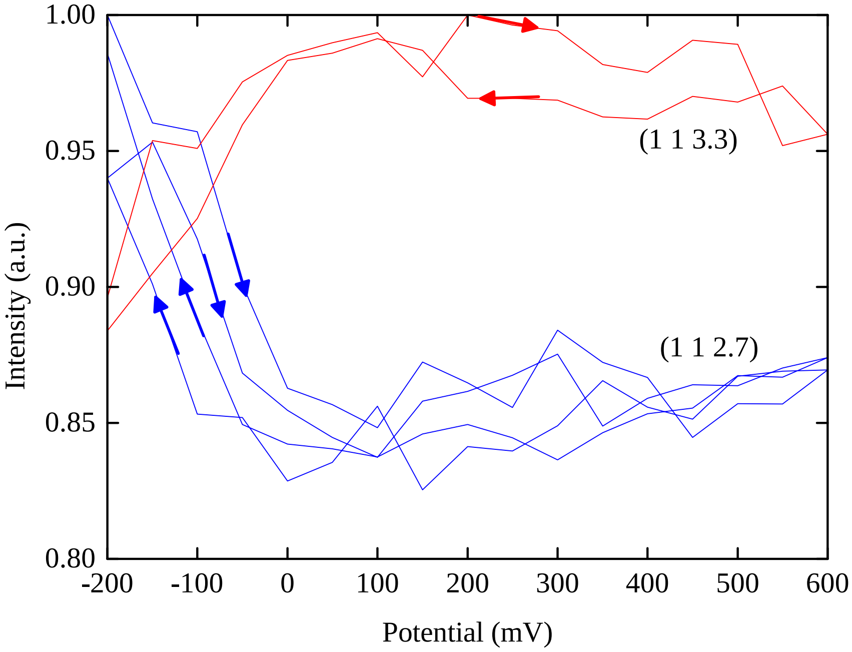

FIGURE 5.1: XRV measured at the relaxation sensitive positions (1 1 3.3) and (1 1 2.7), which are shown in red and blue respectively, as the potential was cycled between -200 mV and 600 mV at 5 mV s^{-1}. A surface expansion in the hydrogen region can be seen.

Layer	Occupation	Relaxation	Debeye-Waller Factor
1^{st} (Top)	0.24 ± 0.04	0.036 ± 0.010	0.00 ± 0.17
2^{nd}	1.00 ± 0.03	0.001 ± 0.003	0.00 ± 0.07
3^{rd}	1.00 ± 0.03	0.008 ± 0.004	0.00 ± 0.08

TABLE 5.1: Best fit parameters obtained from analysis of CTR data taken at -200 mV. The fit parameters deduced for the surface atomic layer expansion, relative surface coverage and surface roughness are shown along with their associated error.

and the data and best fit are shown in figure 5.3. The fit shows an imperfect termination, with the top monolayer having an occupation of 0.25 ± 0.04 monolayers. The fit for the specular and non-specular rods are the same, which shows the structure is commensurate the (1 x 1) structure and not the incommensurate hex reconstruction seen with experiments in UHV environments. It would appear that exposure either to the electrolyte, or the atmosphere during sample transfer, causes a collapse of the hex reconstruction.

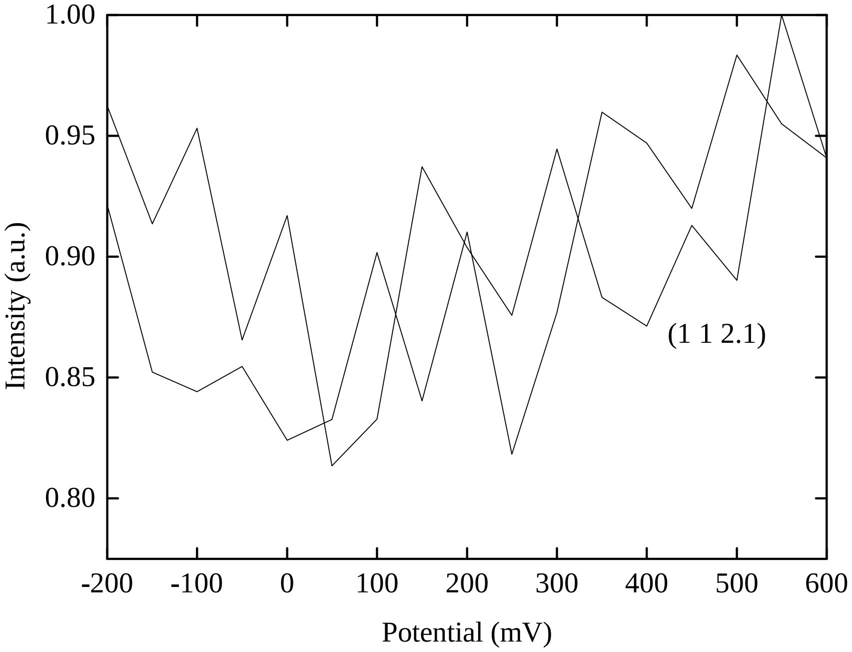

FIGURE 5.2: XRV measured at the commensurate surface occupation/roughness sensitive position (1 1 2.1), as the potential was cycled between -200 mV and 600 mV at 5 mV s^{-1}. No measurable change was seen indicating the surface was stable at these potentials.

Layer	Occupation	Relaxation	Debeye-Waller Factor
1^{st} (Top)	0.22 ± 0.03	0.032 ± 0.010	0.00 ± 0.18
2^{nd}	1.00 ± 0.03	-0.005 ± 0.004	0.00 ± 0.08
3^{rd}	1.00 ± 0.04	0.007 ± 0.004	0.00 ± 0.08

TABLE 5.2: Best fit parameters obtained from analysis of CTR data taken at +600 mV. The fit parameters deduced for the surface atomic layer expansion, relative surface coverage and surface roughness are shown along with their associated error.

An anodic sweep to +600 mV was performed and the CTR measurements were repeated. The fit parameters at this potential are shown in table 5.2 and the data and best fit are shown in figure 5.4. The only change was an inward relaxation of 0.02 ± 0.02 Åof the first complete monolayer which is not significant.

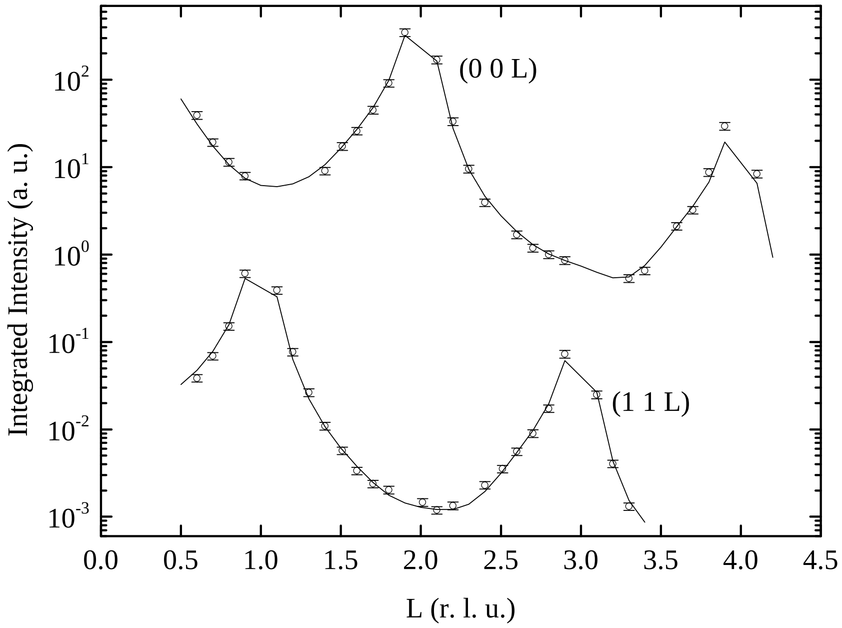

FIGURE 5.3: The (1 1 L) and (0 0 L) CTRs measured at -0.2 V for the as-prepared surface. The solid line is a fit to the data and the χ^2 for this fit is 1.59.

5.3 Oxidation of Pt(100)

Once the study of the Pt(100) surface within the region of stability was complete, characterisation of the oxide could begin. A cathodic sweep down to -200 mV was followed by an anodic sweep to +1100 mV at 5 mV s^{-1}, a potential in the oxidation region. The x-ray intensity was measured during this scan at the (0 0 1) anti-Bragg position, shown as circles in figure 5.5; for comparison the oxidation of Pt(111) is displayed on the same plot as triangles. It can be seen that while oxidation begins at approximately the same potential on both surfaces (900 mV), the process is much faster on Pt(100) where the intensity plateaus roughly 1600 s earlier than Pt(111). This would indicate that the oxide of platinum forms much more readily on Pt(100) than Pt(111), almost certainly due to the more open structure of the Pt(100) surface.

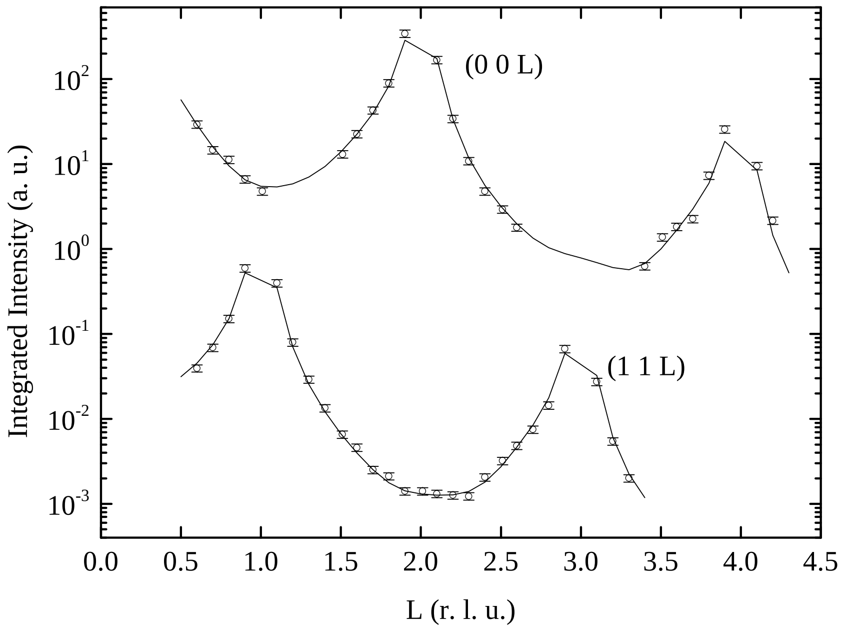

FIGURE 5.4: The (1 1 L) and (0 0 L) CTRs measured at 0.6 V for the as-prepared surface. The solid line is a fit to the data and the χ^2 for this fit is 1.78.

The CTR measurements were repeated in the oxide region. The specular and non-specular CTRs required separate fits, which, as with Pt(111), indicated the oxide is an ordered incommensurate structure or lacks long range order. The fit parameters at this potential for the specular CTR are shown in table 5.3 and the data and best fits are shown in figure 5.6. As with the oxide formation on Pt(111), a buckling of 0.82 ± 0.12 Åin the top monolayer is seen. This would indicate that the oxide particulates formed on Pt(100) could have the same structure and orientation as those found on Pt(111).

The surface was then reduced during an anodic sweep to -200 mV at 5 mV s^{-1}. The xray intensity was measured at the (0 0 1) position during the reduction, an anti-Bragg position sensitive to surface occupation. As with Pt(111) a sharp drop in intensity was seen at the beginning starting at approximately 450 mV, followed by a recovery as the potential reaches 0 V; with the maximum recovery seen at -200 mV. This would indicate that the oxide is stable at potentials as low as 450 mV,

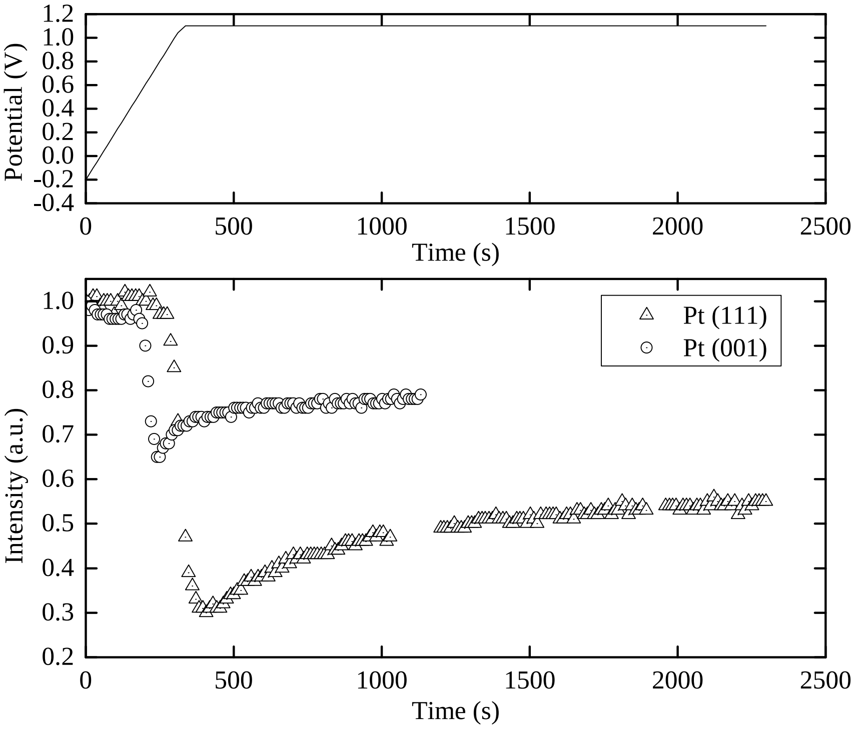

Figure 5.5: XRV measured at the surface occupation sensitive position (0 0 1), as an anodic sweep was performed from -200 mV and 1100 mV at 5 mV s^{-1}. The measurement of the x-ray intensity continued at the potential of 1100 mV until it stabilised. For comparison, the Pt(100) data (circles) is shown alongside the Pt(111) data (triangles) which was take at the (0 0 1.55) anti-Bragg position. The oxidation kinetics on the Pt(100) system are far quicker than the Pt(111), likely due to its more open surface.

Layer	Occupation	Relaxation	Debeye-Waller Factor
$1^{st}a$ (Top Buckled)	0.08 ± 0.04	0.21 ± 0.03	0.00 ± 0.42
$1^{st}b$ (Top)	0.56 ± 0.03	0.000 ± 0.004	0.00 ± 0.19
2^{nd}	0.93 ± 0.02	0.006 ± 0.003	0.00 ± 0.07
3^{rd}	1.00 ± 0.02	0.001 ± 0.003	0.00 ± 0.07

Table 5.3: Best fit parameters obtained from analysis of specular CTR data taken at +1100 mV. The fit parameters deduced for the surface atomic layer expansion, relative surface coverage and surface roughness are shown along with thier associated error.

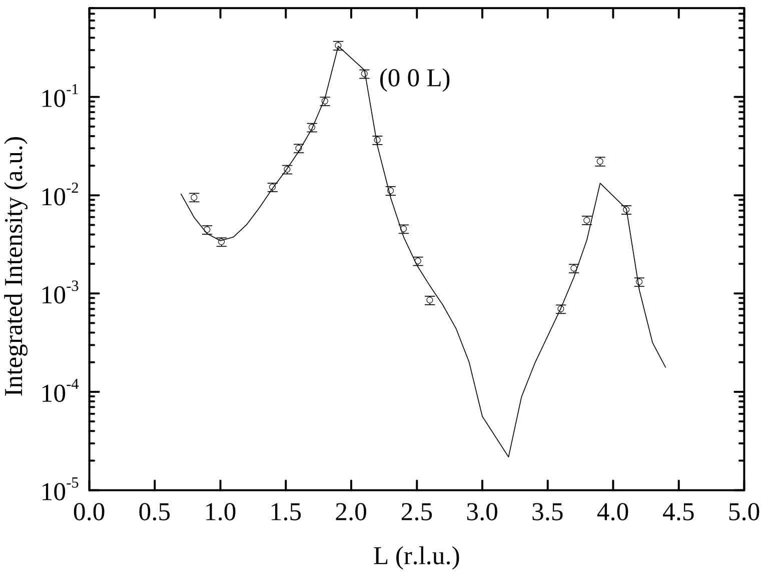

FIGURE 5.6: The (0 0 L) CTR measured at 1.1 V for the oxide surface. The solid line is a fit to the data and the χ^2 for this fit is 1.33.

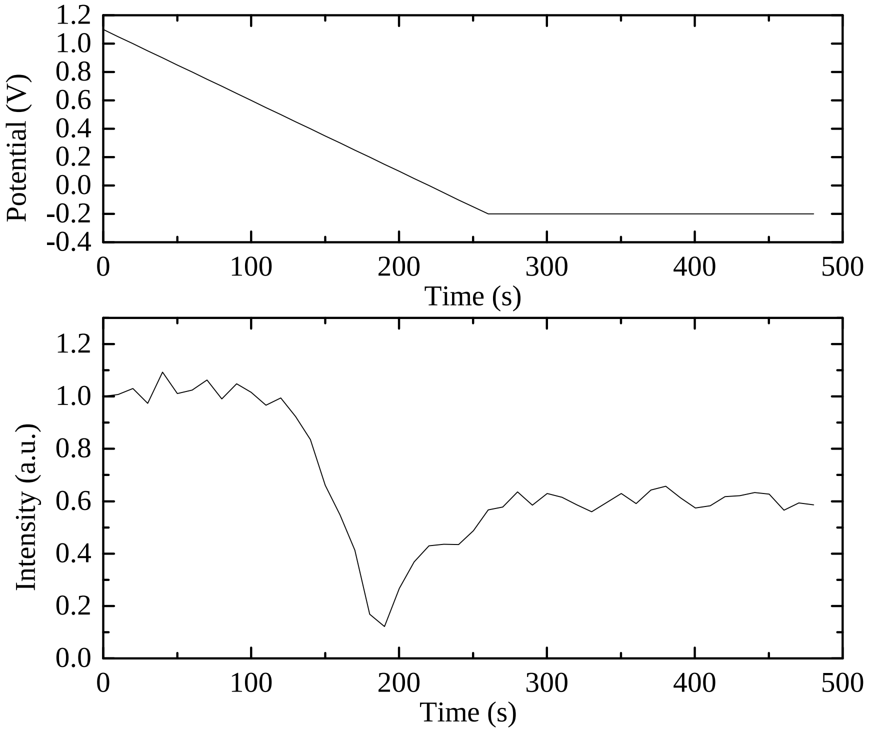

FIGURE 5.7: XRV measured at the surface roughness sensitive position (0 0 1), as a cathodic sweep was performed from 1100 mV to -200 mV at 5 mV s^{-1}. Reduction begins, as with Pt(111), at ~600 mV where a similar dissolution and redeposition process is seen.

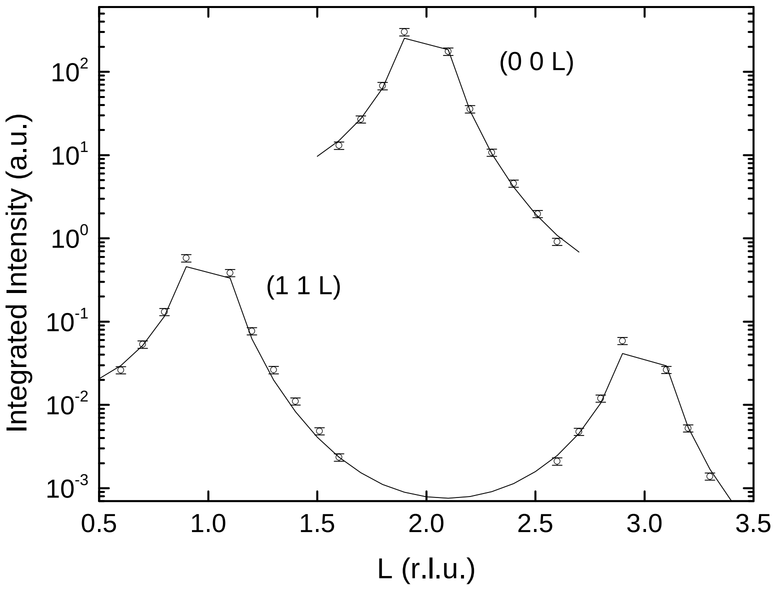

FIGURE 5.8: The (1 1 L) and (0 0 L) CTRs measured at -0.2 V for the reduced surface. The solid line is a fit to the data and the and the χ^2 for this fit is 1.90.

at which point there is a fairly rapid reduction of the oxide particulates. The CTR measurements were repeated once again on the reduced surface, the data and best fit is shown in figure 5.8. Both CTRs were fit with the same model, a β factor of 0.32 ± 0.07, showing that the surface had returned to a commensurate structure.

Following surface repreparation, the crystal was remounted and aligned. The film raised and the potential cycled 100 times between -200 mV and 1100 mV at 50 mV s^{-1}. The CTR measurements were then repeated, the data for which is shown in figure 5.9. There is no fit to this data as the only intensity seen is at the Bragg positions caused by an extreme roughening of the surface. This prohibits the use of the kinematical approximation for modelling; unlike Pt(111) no island growth is seen on the Pt(100) surface. The cause of this roughening is likely to be due to recrystallisation of the surface during cycling, as the Pt atoms attempt to form Pt(111) terraces due to this surface having a lower surface energy.

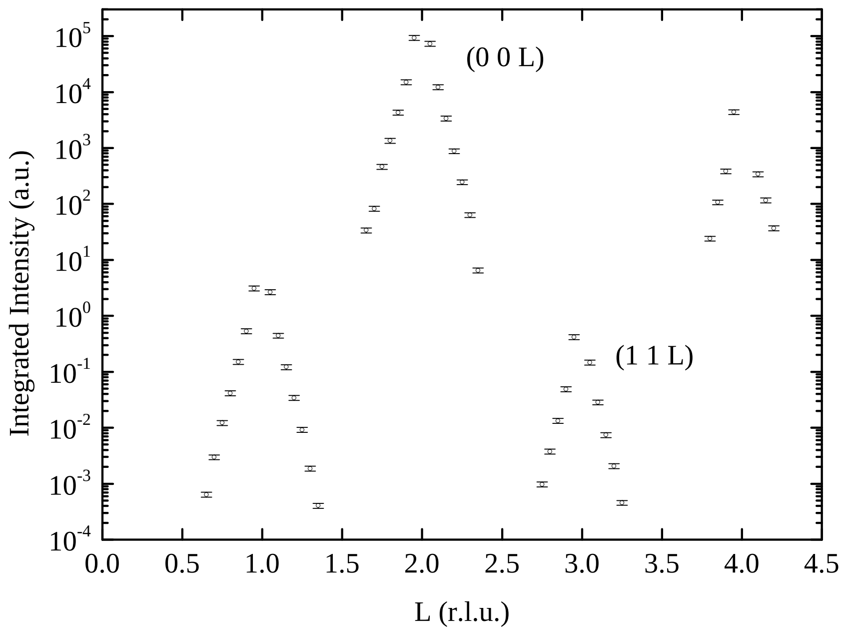

FIGURE 5.9: The (1 1 L) and (0 0 L) CTRs measured at -0.2 V for the cycled surface. It was not possible to fit this data due to the high degree of roughness.

5.4 Summary

The Pt(100)-electrolyte interface has been characterised using surface x-ray diffraction techniques both in the potential range of OH adsorption (which indicates the surface is stable) and into the potential range of oxide formation (which leads to irreversible roughening of the surface). XRV measurements in the region of stability indicate the surface undergoes a reversible surface relaxation in the hydrogen adsorption region of 0.02 ± 0.02 Å. CTR measurements of the clean surface reveal an incomplete 0.25 monolayers of platinum on the surface due to excess atoms from the lifting of the hex-reconstruction. This reconstruction is lifted either during the cooling process or on contact with the electrolyte. The Pt(100) oxide is incommensurate, and analysis of the CTR data was consistent with a buckling of the Pt surface layer of 0.82 ± 0.12 Å; similar to that caused by oxide particulates on Pt(111). CTR measurement after reduction revealed that the roughening of the surface was irreversible and, unlike the Pt(111) surface, the roughening process occurred during the oxide formation rather than during oxide reduction. The l dependence of the CTRs indicated that the surface was extremely rough after cycling into oxide region multiple times, with measurable intensity only seen very close to the Bragg positions.

While Pt(100) is more active than Pt(111) with regards to the ORR, it appears to be more susceptible to irreversible structural changes caused by oxidation and reduction. This comparison gives a strong insight into the role of surface atomic geometry on catalyst stability. As a consequence, platinum nanocubes would be ill suited as catalysts in PEMFCs as the open (100) surfaces leave them extremely vulnerable to sintering. In the following chapter the link between stability and reactivity is explained for a promising alternative catalyst material, i.e. a bimetallic Pt_3Ni alloy, which has shown remarkably high activity for the oxygen reduction reaction.

Chapter 6

Potential Dependence of the Surface Stability of $Pt_3Ni(111)$

6.1 Introduction

Bimetallic surfaces offer an exciting new avenue into catalyst research. Alloy systems can change the electronic properties of the catalyst surface or give bifunctional properties to the surface due to the surface geometry. An example of the latter would be Pt_3Sn which is highly resident to CO poisoning due to Sn surface atoms bonding strongly with CO, leaving the Pt surface atoms free to perform as a catalyst [88]. One of the most interesting bimetallic systems is $Pt_3Ni(111)$, which has been identified as being 90-fold more active than the current state-of-the-art Pt/C catalysts for PEMFC [89]. This has been attributed to a change in the electronic properties of the surface Pt atoms (so-called d-band shift) induced by the presence of a Ni-rich sub-surface. Two different surface compositions of polycrystalline Pt_3Ni surface can be prepared in UHV, either the annealed 100% Pt or the sputtered 75% Pt surface;with the 100% Pt or “Pt skin” surface having the greatest activity with regards to the ORR in acidic solution [90]. Both surfaces are much more active than pure Pt with the 100% Pt surface being four times more active[91]. Alloying Pt with Ni causes a positive shift in the d-band centre, which causes the increase in activity due to weakening of the OH_{ad} interaction [92].

A combined LEED, LEIS and UPS study on $Pt_3Ni(111)$ showed that this surface is segregated once annealed, giving 100% Pt concentration in the surface layer. A (1 x 1) LEED pattern was seen as with Pt(111), as was a positive shift in the d-band centre to 3.09 eV [93]. *In-situ* resonance SXS experiments have shown that at -150 mV the $Pt_3Ni(111)$ surface is segregated, such that the top layer is 100% Pt while the second layer is Ni rich at 52% Ni concentration and the third layer is Pt rich at 87% Pt. It is this segregation which causes the shift in the d-band and a 10-fold increase in the ORR activity [89]. Monte Carlo calculations of Pt_3Ni nanoparticles found that the octahedral nanoparticle surface segregation would be identical to the $Pt_3Ni(111)$ surface [94]. Pt_3Ni nanoparticles can be tailored to give either cubic nanoparticles with (001) faces or octahedral nanoparticles with (111) faces using various methods, with the octahedral nanoparticle having the greatest ORR activity [95–97]. These octahedral nanoparticles have been seen to self assemble into superlattices with a low packing density, ideal for high surface area fuel cell catalysts [98].

The experiments in this chapter begin with the characterisation of the $Pt_3Ni(111)$ surface, including the surface segregation. An XRV measurement within the window of stability (-200 mV to +600 mV) was taken at a position sensitive to surface relaxation. A specular CTR was taken at the negative limit, with an identical measurement at +600 mV to allow comparison of the surface segregation. To probe the stability of the surface at increasing potentials CTR measurements were taken at 850 mV and 950 mV. After reduction of the surface an attempt was made to measure the specular CTR, but at this point the surface became unstable, likely associated with nickel leeching.

6.2 Pt_3Ni Surface Preparation

The $Pt_3Ni(111)$ crystal surface was prepared in UHV by continued cycles of sputtering and annealing. AES was used to ensure the surface was clean and the process was continued until a sharp (1 x 1) pattern was seen using LEED. During transportation outside of the UHV environment the crystal was immediately transferred into clean de-aerated water. Both immersion back into the UHV environment and measurements of the electrochemical response, which are sensitive to impurity concentrations, have proven that this method maintains a contaminant free surface. Following this procedure, using a drop of electrolyte for protection of the surface, the crystal can be safely transferred to the x-ray electrochemical cell.

Pt_3Ni bulk alloy has a an ordered fcc lattice with a random occupation of platinum and nickel, according to the stoichiometry, when annealed the surface layers segregate forming a pure platinum surface “skin”. Auger electron spectroscopy and previous x-ray experiments at -200 mV vs. $Ag/AgCl^+$, have shown that the surface is pure platinum. As nickel has a lower atomic number than platinum, the Pt layer concentration causes changes in the CTRs that are identical to changes in layer occupation. There is no way with general x-ray diffraction to differentiate between individual layer platinum concentration and occupation.

6.3 Surface Characterisation

The $Pt_3Ni(111)$ crystal was prepared in UHV using sputter and anneal cycles, until a clean LEED (1 x 1) pattern was seen. After removing the sample from UHV it was transferred into the x-ray electrochemical cell and then mounted on the diffractometer. Potential contact was made at -0.2 V.

The window of stability of $Pt_3Ni(111)$ is similar to that of Pt(111), therefore a comparable measurement of the surface expansion was performed using an XRV

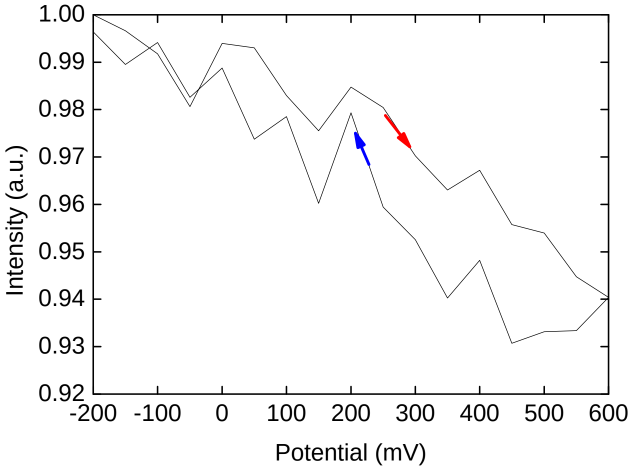

FIGURE 6.1: XRV measured at the relaxation sensitive position (0 0 2.7), the potential was cycled between -200 mV and 600 mV at 5 mV s^{-1}. The drop in intensity shows an inward relaxation of the surface in the hydroxide adsorption region.

at the (0 0 2.7) position; a position sensitive to surface expansion. This XRV was taken within the potential limits of -200 mV to +600 mV at 5 mV s^{-1} and is shown in figure 6.1. As with Pt(111) a surface relaxation is seen, however there is much less hysteresis with $Pt_3Ni(111)$. This would indicate the expansion kinetics are much faster on $Pt_3Ni(111)$.

In order to measure any changes in surface segregation and the relaxation the first step was to characterise the surface at the negative potential limit (-200 mV). As the specular CTR is sensitive to electron density along the surface normal it is the best tool for analysing surface segregation, in addition to measuring the surface relaxation. The CTR data and fit is shown in figure 6.2, with the best fit parameters shown in table 6.1. The CTR was fit using a least squares method and is in good agreement with previous results on this system [90].

The film was then raised for an anodic sweep to +600 mV at 5 mV s^{-1}, in preparation for the CTR measurement. The specular CTR was measured using rocking scans with the same intervals in l as used for the -200 mV CTR data. The CTR data and fit at this potential are shown in figure 6.4, with the best fit parameters

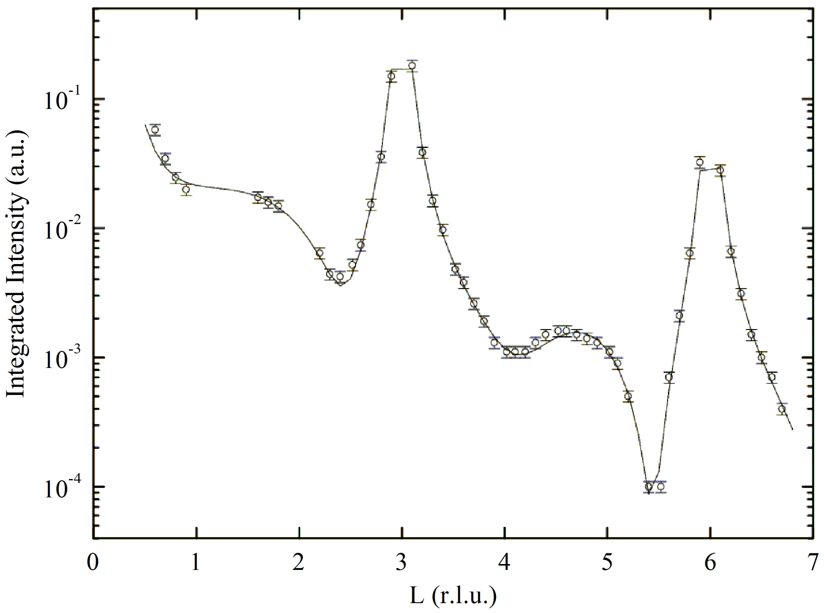

FIGURE 6.2: The specular CTR measured at -0.2 V for the as-prepared surface. The solid line is a fit to the data and the χ^2 for this fit is 1.07.

Layer	Occupation	Platinum Conc.	Relaxation	Debye-Waller Factor
$1^{st}(Top)$	1.00 ± 0.05	1 (fixed)	-0.005 ± 0.002	0.17 ± 0.02
2^{nd}	1.00 ± 0.07	0.41 ± 0.06	-0.008 ± 0.002	0
3^{rd}	1.00 ± 0.05	0.77 ± 0.06	0.004 ± 0.002	0

Bulk Debye-Waller factor = 0.15 ± 0.02
Beta Factor = 0

TABLE 6.1: Best fit parameters obtained from analysis of CTR data taken at -200 mV vs. Ag/AgCl$^+$. The fit parameters deduced for the surface atomic layer expansion, relative surface coverage, platinum concentration of each layer and surface roughness are shown along with their associated error. The bulk Debye-Waller factor is also shown.

shown in table 6.2. The only significant change seen to the crystal was a decrease in surface occupation of the top monolayer to 0.93 ± 0.04, a diffusion effect similar that caused by platinum mobility seen on the Pt(111) surface. In addition to the decrease in Pt occupation of the top layer, a half monolayer of oxygen at a distance of 2.0 Åwas required for a good fit; which is assumed to be OH_{ad}. This model would indicate a breaking of the platinum skin when cycling to +600 mV, possibly making the surface vulnerable to nickel dissolution. Nevertheless, on performing

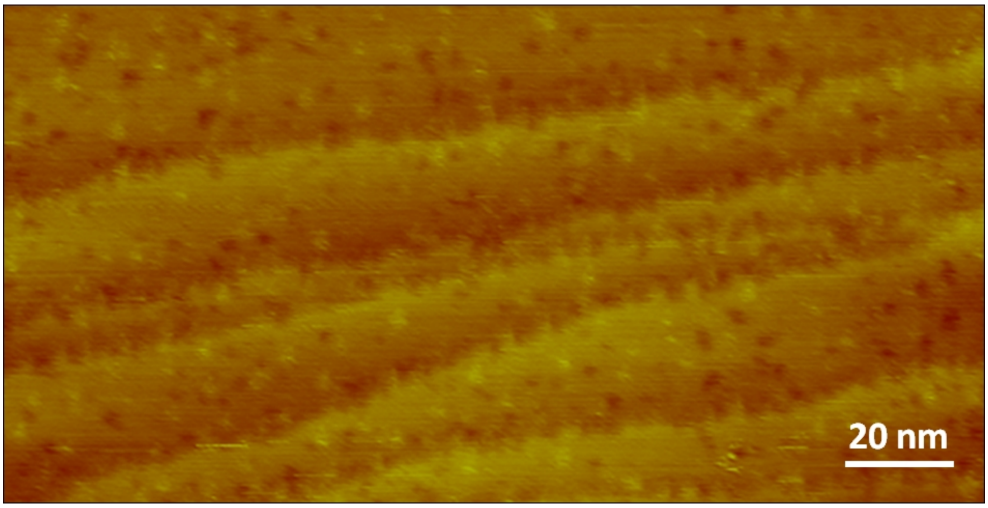

FIGURE 6.3: STM image of the as-prepared $Pt_3Ni(111)$ surface, showing smaller terraces than Pt(111). In addition, small vacancies are seen in the surface due to the dissolution of the small percentage of Ni present on the surface after preparation.

a potential sweep back to -200 mV, rocking scans at surface sensitive positions confirmed that the intensity changes were fully reversible.

Although both voltammetry and SXS analysis suggest a near perfect first layer that contains 100% of Pt atoms (so-called Pt-skin), neither method is capable of providing missing real space atomic structure, required for a visualization of potential/electrolyte induced local changes in the surface morphology of the Pt-skin layer. In other words, these techniques cannot see small surface imperfections because they sum the signal from the whole surface. As for Pt(111) in figure 4.2, this information is obtained from analysis of an STM image presented in figure 6.3. The overall picture that emerges from STM analysis is that the Pt-skin surface is more defected than the surface of Pt(111); a notable feature is the appearance of both adislands and pits that are randomly distributed on relatively large terraces (∼25 nm), which are separated by monoatomic steps. The fact that this image corresponds to pristine $Pt_3Ni(111)$ immersed at -150 mV indicates that annealing induced segregation in UHV is not ideal, and selective loss of the remaining 5% of the Ni surface atoms occurs instantaneously upon immersion into the electrolyte. The same was confirmed by ICP-MS analysis of the supporting electrolyte. The

Layer	Occupation	Platinum Conc.	Relaxation	Debye-Waller Factor
O Layer	0.5 ± 0.7	n/a	0.30 ± 0.06	0
$1^{st}(Top)$	0.93 ± 0.04	1.00 ± 0.07	-0.002 ± 0.003	0.15 ± 0.02
2^{nd}	1.00 ± 0.07	0.49 ± 0.06	-0.010 ± 0.002	0
3^{rd}	1.00 ± 0.05	0.75 ± 0.06	0.005 ± 0.002	0

Bulk Debye-Waller factor = 0.15 ± 0.02
Beta Factor = 0

Table 6.2: Best fit parameters for the reduced surface occupation model, obtained from analysis of CTR data taken at +600 mV vs. Ag/AgCl$^+$. The fit parameters deduced for the surface atomic layer expansion, relative surface coverage, platinum concentration of each layer and surface roughness are shown along with their associated error. The bulk Debye-Waller factor is also shown.

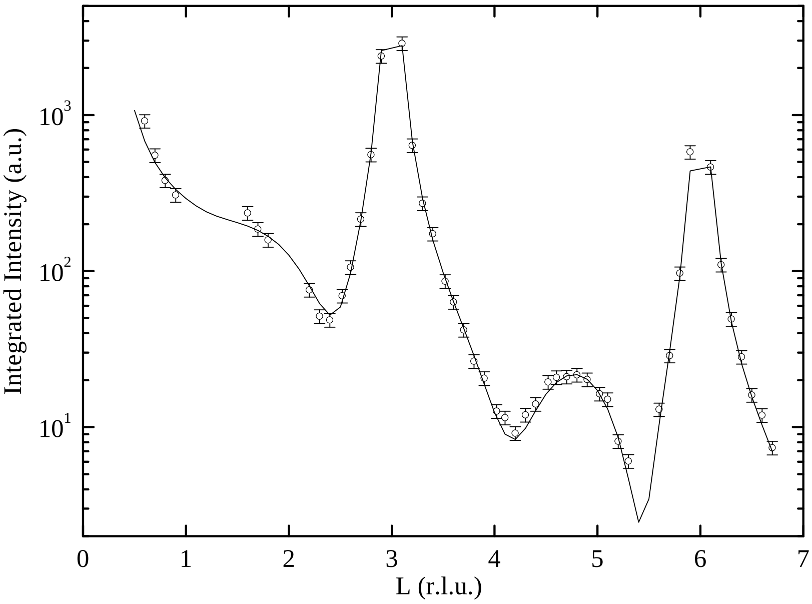

Figure 6.4: The specular CTR measured at 600 mV. The solid line is a fit to the data and the χ^2 for this fit is 1.09.

amount of Ni found in the solution corresponded to 0.04 ML of Ni calculated as number of surface atoms compared to Pt surface atoms. Importantly, however, even after exposure to potentials up to 750 mV the STM image remains roughly the same, suggesting that between -150 and 750 mV the Pt-skin is indeed stable.

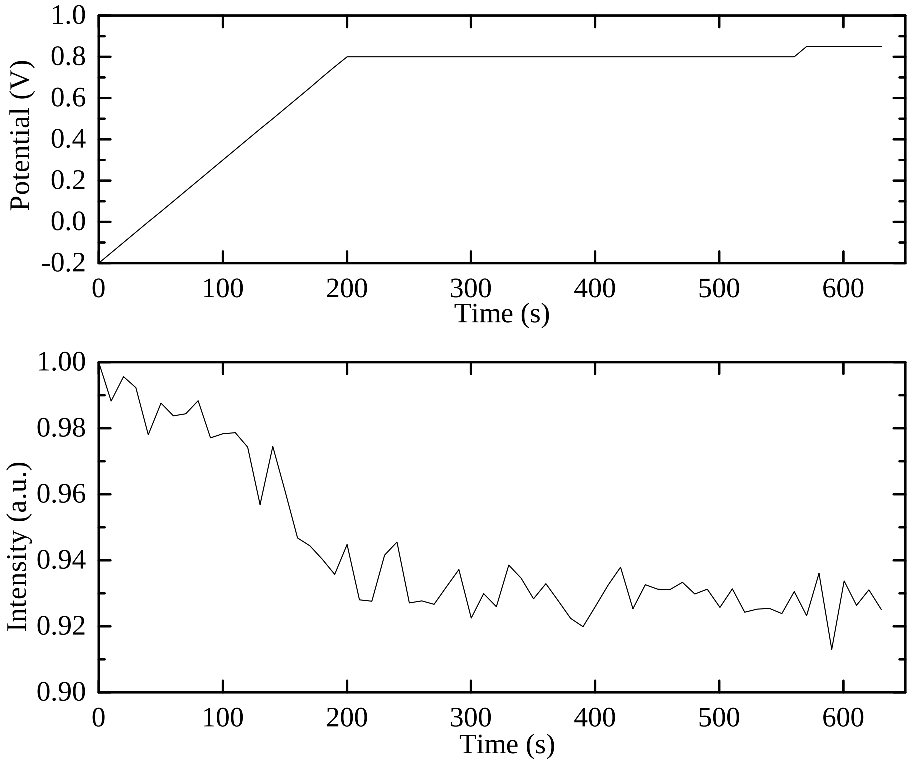

Figure 6.5: X-ray intensity measured at (0 0 2.7) during the potential sweep from -200 mV to +800 mV at 5 mV s^{-1}. The potential begins at -200 mV at time = 0, reaching 800 mV at the line on the left. At the line on the right the potential is stepped up to 850 mV. The measurement has been background subtracted and normalised so the most intense point equals one. The surface appears to be stable at this potential.

6.4 Surface Stability at Increasing Potentials

The next step after characterising the surface was to measure the surface within the window of stability at increasing potentials, starting at 850 mV, a potential close to the edge of the region of stability measured with cyclic voltammetry. Figure 6.5 shows a cathodic sweep from -200 mV to +800 mV. The sample was then stepped to +850 mV in preparation for a CTR measurement. During this anodic sweep it can be seen that the relaxation of the surface is proportional to the potential applied, reaching stability almost as soon as the sweep is complete. This is typical of a change in structure with fast kinetics. The total change in intensity at 850 mV is comparable with that seen in the XRV to +600 mV, to

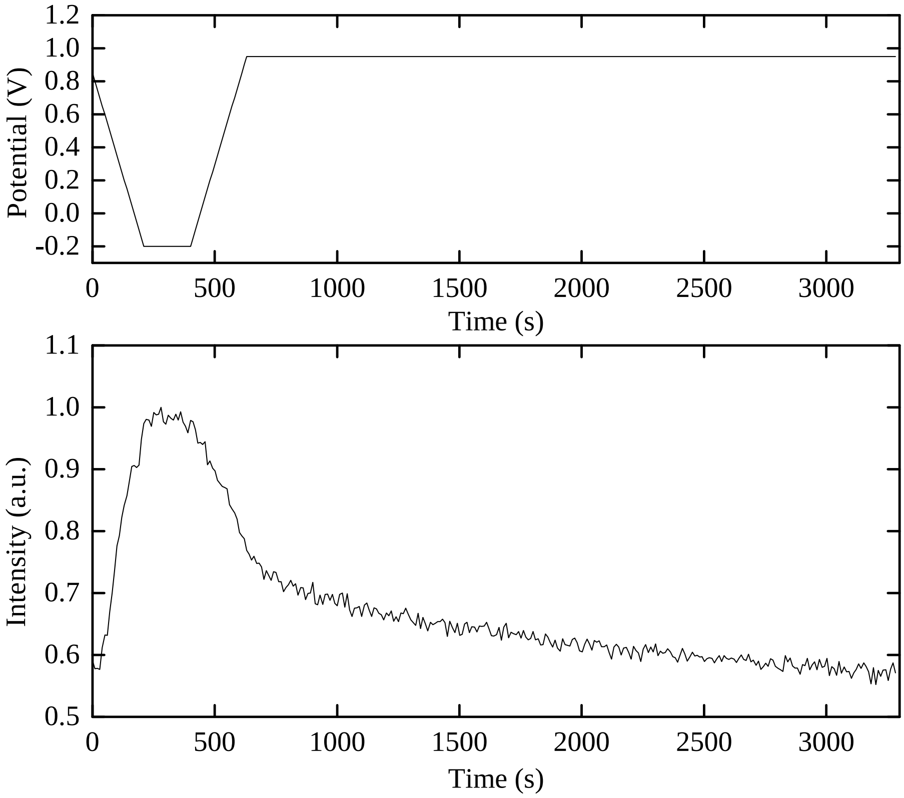

FIGURE 6.6: X-ray intensity measurement at (0 0 1.7). At time = 0 the potential is 850 mV and the potential is reduced at a rate of 5 mV s^{-1} until it reaches -200 mV. The potential is then increased at a rate of 5 mV s^{-1} until it reaches 950 mV. The measurement has been background subtracted and normalised so the most intense point equals one. At 950 mV the surface take over 2000 s to stabilise, reminiscent of the oxidation process on Pt(111).

approximately 93% of the intensity at -200 mV. A measurement of the specular CTR was performed, the fit for which was identical to that at +600 mV. This result shows that there is no significant change in the surface structure or stability between +600 mV and +850 mV in this system.

A potential step was performed from 850 mV down to -200 mV and then back up to 950 mV, with the x-ray intensity measured at (0 0 1.7), a position sensitive to electron density in the surface layers. The plot is shown in figure 6.6 and it has been normalised so that the highest intensity point equals one. A rapid increase in intensity is seen with a stable plateau as soon as -200 mV is reached, this is typical of an increase in surface occupation; which is expected as cycling to 850 mV should

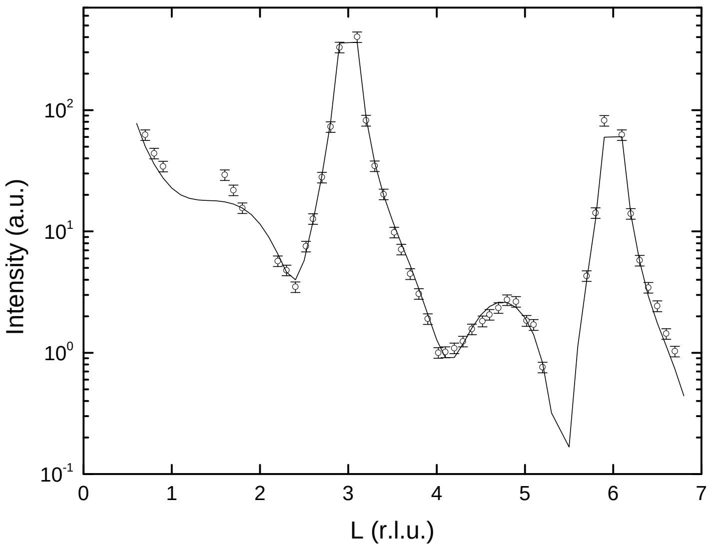

FIGURE 6.7: The specular CTR measured at 950 V. The solid line is a fit to the data and the χ^2 for this fit is 1.82.

Layer	Occupation	Platinum Conc.	Relaxation	Debeye-Waller Factor
O Layer	0.5 ± 0.7	n/a	0.30 ± 0.06	0
$1^{st}(Top)$	0.87 ± 0.05	1 ± 0.07	-0.002 ± 0.003	0.15 ± 0.02
2^{nd}	1.00 ± 0.07	0.49 ± 0.06	-0.010 ± 0.002	0
3^{rd}	1.00 ± 0.05	0.75 ± 0.06	0.005 ± 0.002	0

Bulk Debye-Waller factor = 0.15 ± 0.02
Beta Factor = 0

TABLE 6.3: Best fit parameters obtained from analysis of CTR data taken at 950 mV. The fit parameters deduced for the surface atomic layer expansion, relative surface coverage, platinum concentration of each layer and surface roughness are shown along with their associated error. The bulk Debye-Waller factor is also shown.

be reversible. On the positive sweep to 950 mV a sharp drop in intensity is seen, which is expected as it has was also seen during the sweep to 850 mV. Unlike the sweep to 850 mV the intensity does not reach its minima once reaching 950 mV and instead continues to decay for an additional 40 minutes before stabilising. This is reminiscent of the oxidation process on Pt(111).

With the potential held at 950 mV the specular CTR was measured once again, with the fit performed using the same method. The CTR data and best fit are

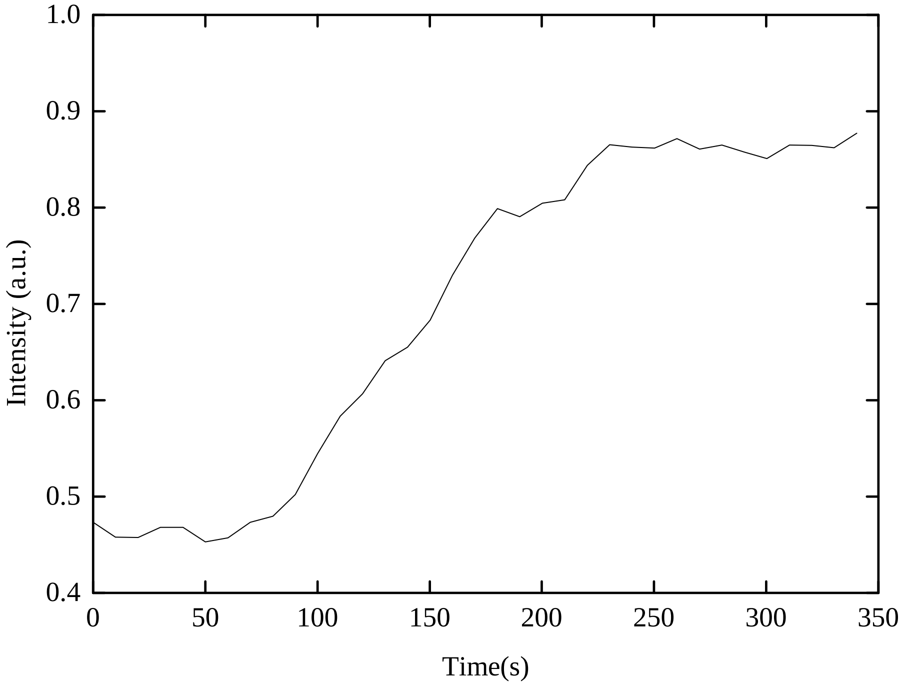

FIGURE 6.8: X-ray intensity measurement at (0 0 1.7). At time = 0 the potential is 950 mV and the potential is decreased at a rate of 5 mV s^{-1} until it reaches -200 mV. The measurement has been background subtracted and normalised so that it is on the same scale as figure 6.6

shown in figure 6.7 and the fit parameters are shown in table 6.3. The fit to the CTR gave results that are broadly consistent with the data measured at 850 mV, the only significant change being the drop in occupation of the surface layer. Attempts were also made to fit this data by varying the sub-surface Ni occupation and by varying the Debye-Waller factor but in both cases the fit was poor. It seems likely, therefore, that even at 950 mV there is no significant change in the concentration profile and the only significant change is in the surface roughness/occupation.

Following the CTR measurements at 950 mV the potential was reduced to -200 mV, and the x-ray intensity was measured at (0 0 1.7) during the sweep; which is shown in figure 6.8. The intensity is normalised against the same intensity as figure 6.6 and shows that the intensity at -200 mV fails to recover to the

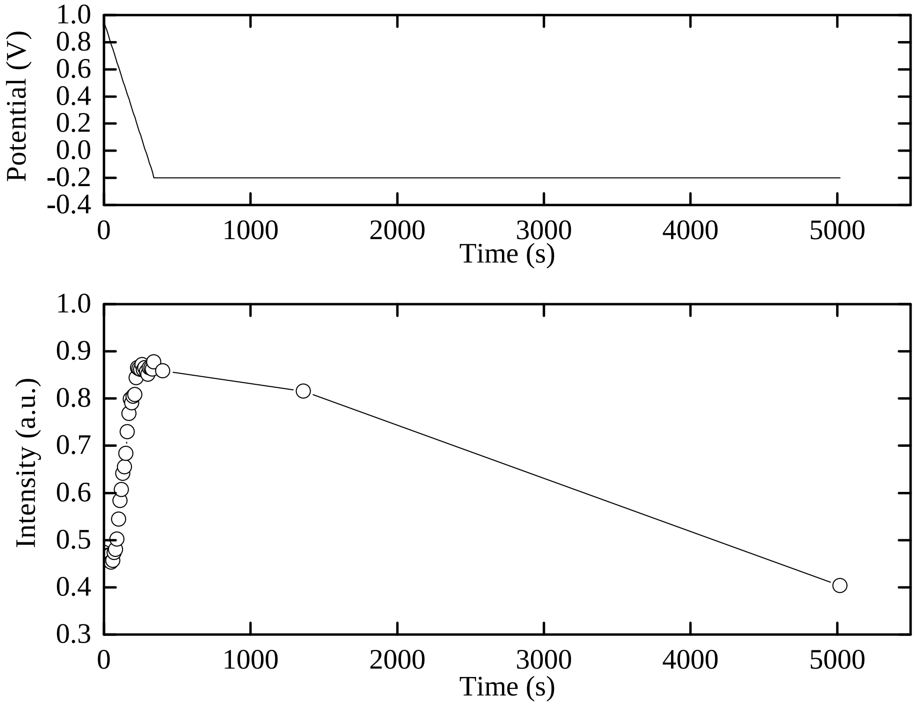

FIGURE 6.9: X-ray intensity measurement at (0 0 1.7). At time = 0 the potential is +0.95 V and the potential is decreased at a rate of 5 mV s^{-1} until it reaches -0.2 mV at the first line. Three additional measurements show the long term degradation of the surface. The measurement has been background subtracted and normalised so that it is on the same scale as figure 6.6.

level seen before the measurements at 950 mV. Following this potential sweep an attempt was made to measure the CTR at -200 mV but, as shown in figure 6.9, the surface was no longer stable and underwent significant roughening as a function of time. This behaviour would be expected if the surface platinum skin had been broken, allowing dissolution of the sub-surface nickel.

Figure 6.10 shows the STM for the surface held at 900 mV for 1000 s and then reduced. As with Pt(111), $Pt_3Ni(111)$ shows its first morphological changes after potential excursions above 750 mV. A gradual corrugation of steps occurs on both surfaces as the potential is opened up towards the oxide region. ICP-MS analysis of the adjacent solution showed traces of platinum pointing to the start of the dissolution of the noble metal. A significant concentration of Ni in the solution was

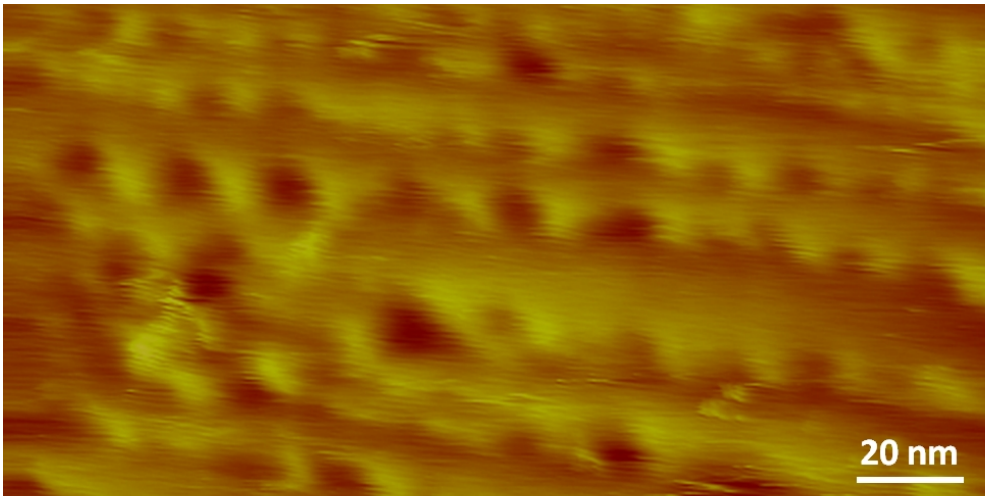

FIGURE 6.10: STM image of the $Pt_3Ni(111)$ surface after cycling to 0.9 V. The surface appears to be roughened during cycling.

measured indicating a further dissolution of the underlying metal. The amount of Ni lost from the interfacial layers corresponded to 0.4 ML. Figure 6.11 is an STM image of the surface after cycling into the oxide region multiple times. The STM image shows, as with Pt(111), the surface transforms into a two-dimensional semi-ordered array of adislands. As in the holding experiments, the morphological changes closely follow those of Pt system with one significant difference which is evident from both sets of experiments, i.e. the rearrangement of surface Pt atoms causes the exposure of the underlying Ni metal which dissolves upon contact with the acidic electrolyte. However the surface retains some of its increased activity, indicating a degree of preservation of the Ni sub-layer.

6.5 Summary

The $Pt_3Ni(111)$ electrolyte interface has been characterised first in the hydrogen adsorption region, using surface x-ray diffraction techniques, then at increasing positive potentials in order to understand the surface structure during oxidation. XRV measurements in the window of stability indicate that the surface undergoes a reversible relaxation in the hydrogen adsorption region. A reduction in the electron

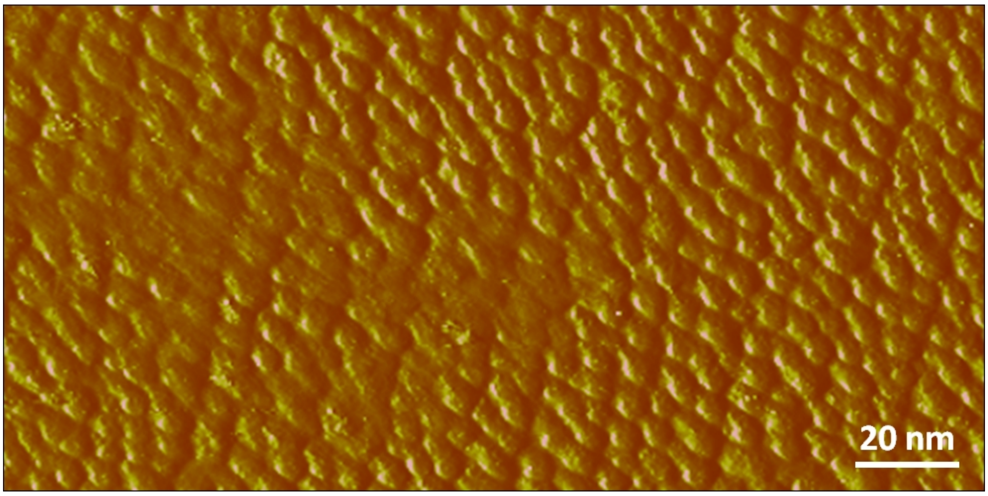

FIGURE 6.11: STM image of the $Pt_3Ni(111)$ surface after cycling to 1.1 V 100 times, showing adislands similar to those seen on Pt(111).

density of the surface atomic layer was seen at the positive limit of the stable region. There was no measurable difference in the surface structure or surface segregation profile after cycling the potential to the onset of surface oxidation. However, potential steps further into the region of oxide formation caused an additional reduction of the surface electron density. A subsequent cathodic sweep led to surface roughening even at negative potentials where the initially prepared surface was stable. Although surface oxidation caused significant leeching of Ni, as shown by the ICP-MS results, STM images of the $Pt_3Ni(111)$ surface show a similar adisland growth as seen on Pt(111). Furthermore, the activity of the $Pt_3Ni(111)$ electrode is considerably reduced after repetitive cycles of the surface oxidation compared to the UHV prepared surface, but it remains higher than that of the pure Pt(111) electrode. This suggests that the Ni rich subsurface adlayer is preserved in the adisland structure.

Chapter 7

Concluding Remarks

One of the main limitations of the low temperature hydrogen fuel cell concerns both the sluggish reactivity of the catalyst on the cathode side towards the oxygen reduction reaction (ORR) and the stability of the catalyst material during potential excursion into the region of oxide formation (which can occur during fuel cell start-up). The state-of-the-art catalyst material is currently pure Pt or Pt-alloy nanoparticles. In an effort to gain a fundamental understanding of the link between catalyst surface structure, reactivity and stability, experiments have been performed on single crystal electrode surfaces via a combination of *in-situ* structural probes and electrochemical (cyclic voltammetry) measurements. The experiments in this thesis have focused on the characterisation of Pt(111), Pt(100) and $Pt_3Ni(111)$ surfaces during oxidation and the change in surface morphology after prolonged potential cycling into the region of oxide formation.

Comparison of the Pt(111) and Pt(100) electrode surfaces provides insight into the role of atomic surface geometry in determining reactivity and stability. Pt(111), which is the least active of the low index surface for the ORR, showed morphological changes after oxidation reduction cycles, with the formation of stable platinum adislands. This restructuring, which occurs due to oxidation and then recrystallisation during oxide reduction, preserves a crystalline (111) surface, although there is a reduction of the in-plane coherence of the crystal structure due to island formation. In contrast, the more active Pt(100) surface undergoes a drastic roughening of the surface during oxidation/reduction cycles. The roughening is due to the fact that the surface is unlikely to recrystallise into the more open (100) surface structure and, hence it is not surprising that the (100) surface becomes completely disordered. In essence, although the Pt surfaces with a more open atomic geometry, e.g. (100) and (110), are more reactive than the close-packed (111) surface, they are intrinsically less stable.

The bimetallic alloy $Pt_3Ni(111)$ surface has been shown to be over 10 times more active for the ORR than pure Pt(111) and exhibits a compositional oscillation at the surface which is formed of Pure Pt. The increased activity is due to the Ni rich sub-surface atomic layer which alters the electronic properties of the pure Pt surface. In addition, the presence of the pure Pt surface layer shields the Ni-rich sub-layer from contact with the electrolyte and prevents dissolution of the Ni from the electrode during cycling at low potentials. The $Pt_3Ni(111)$ electrode appears to be stable when cycling to potentials as high as 850 mV. Nevertheless, potential excursions above this point caused disruptions in the Pt surface layer, leading to Ni dissolution even when the applied potential is returned to a potential range where the UHV-prepared surface was stable. Upon repetitive cycling the $Pt_3Ni(111)$ surface undergoes a similar morphological change to that of Pt(111), where the formation of adislands was seen in STM measurements.

Figure 7.1 shows the activity with regards to the ORR vs. the potential cycling limit for both Pt(111) and $Pt_3Ni(111)$ electrodes. It can be seen that cycling of the Pt(111) electrode to increasingly anodic potential causes an increase in the activity for the ORR until its activity is more like that of the stepped Pt(110) surface. This is likely due to an increase in available reaction sites due to the formation of the crystalline Pt adislands which provide step edges which are analogous to the steps on the (110) surface. In contrast the $Pt_3Ni(111)$ electrode suffers a sharp drop in activity once cycled more positive of 850 mV. This is due to local disruptions of the Pt skin, caused by oxidation, which then leads to exposure of the underlying Ni rich sub-layer to electrolyte and subsequent dissolution of Ni. The reduction in the Ni-rich sub-surface atomic layer causes a decrease in activity which, it might be expected, would tend towards that of pure Pt. However, the Pt3Ni(111) surface shows the same morphological changes as Pt(111), forming adislands. Presumably, these adislands retain some of the active segregated surface structure, preserving the electronic modification due to the Ni-rich subsurface. This leads to a stable surface that remains more active than the pure Pt(111) electrode after prolonged cycling of the potential into the region of oxidation/reduction. Included in the figure are activity measurements at low potential cycles for the Pt_3Ni(10 9 9) and Pt_3Ni(10 7 7) [99], surfaces with lower (111) terrace sizes which indicates the strong link between surface structure and reactivity for the PtNi alloys. The reduction in reactivity of these surfaces over the Pt_3Ni(111) surface would indicate that Ni is dissolved from step edges during cycling at low potentials. Therefore, in contrast to pure Pt, Pt_3Ni(111) is both the most active and stable Pt_3Ni crystal surface.

Perhaps the key insight that can be obtained from these experiments is that electrode activity towards the ORR is intrinsically linked to surface stability, i.e. the more active the surface, the less stable it is. This, in fact, may be a general effect in electrocatalysis. With the fairly imminent depletion of fossil fuels, new methods of producing and storing energy are required to sustain the current standard of living. While fuel cell technology does not solve our energy production needs it does allow a very efficient conversion of chemical energy to electrical energy. To this end future research will likely focus on improving this efficiency, in addition to improving stability. Future experiments would be useful to explore the reactivity-stability relationship in detail for a number of different electrocatalytic reactions. In combination with theoretical calculations and large-scale catalyst screening, the fundamental surface science approach described in this thesis may lead to the discovery of new catalyst materials in a range of energy technologies.

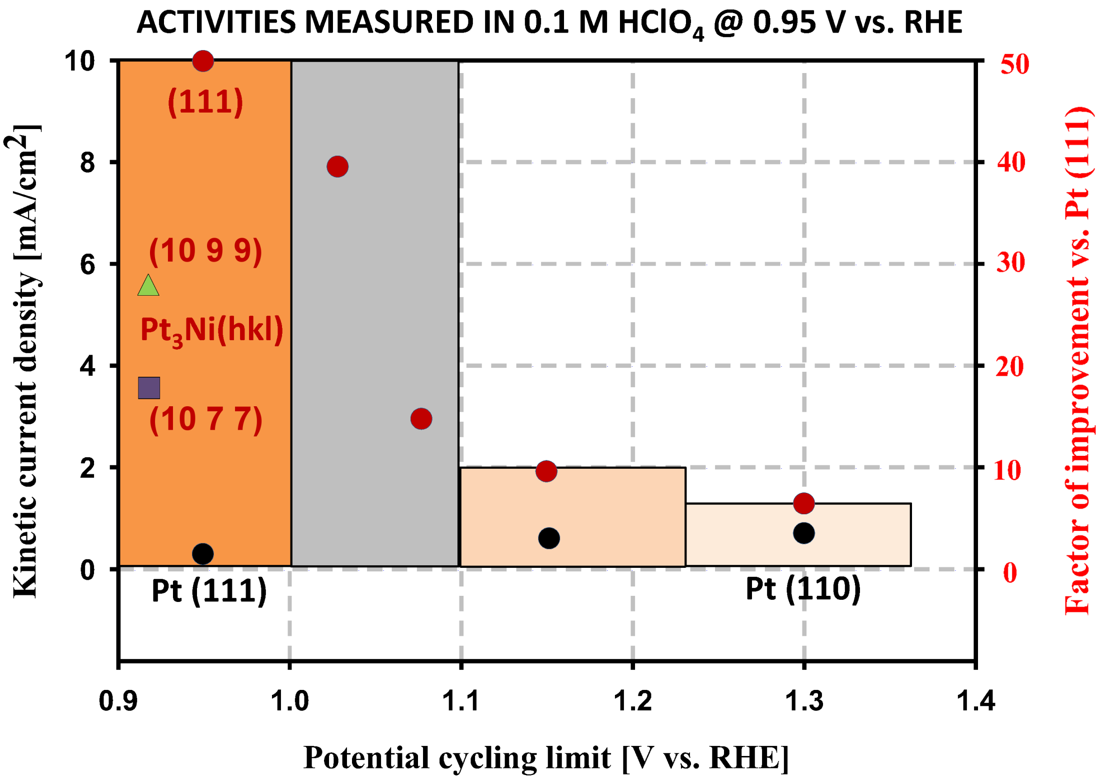

FIGURE 7.1: Summary of the CV measurements for Pt(111) and $Pt_3Ni(111)$ showing the activity vs the potential cycling limit. The red circles show the reactivity of the $Pt_3Ni(111)$ surface which decreases drastically as the potential window opens up to a more positive level. The black circles show the reactivity of Pt(111) which increases slightly at the potenial window is opened up, until the reactivity is more like that of the Pt(110) surface. Included in tis plot are reactivity measurements for the $Pt_3Ni(10\ 9\ 9)$ and $Pt_3Ni(10\ 7\ 7)$ surfaces, with lower (111) terrace sizes. The reduction in reactivity of these surfaces over the $Pt_3Ni(111)$ surface would indicate that Ni is leached from step edges during cycling at low potentials.

Bibliography

[1] D. M. Kolb, “An atomistic view of electrochemistry,” *Surface Science*, vol. 500, no. 1-3, pp. 722–740, 2002.

[2] C. Kittel, *Introduction to Solid State Physics.* Wiley, 8 ed., 2004.

[3] J. Als-Nielsen and D. McMorrow, *Elements of Modern X-Ray Physics.* New York: Wiley, 2000.

[4] I. K. Robinson and D. J. Tweet, “Surface X-ray-Diffraction,” *Reports on Progress in Physics*, vol. 55, no. 5, pp. 599–651, 1992.

[5] C. A. Lucas and N. M. Markovic, “The Encyclopedia of Electrochemistry. vol. 2, section 4.1.2.1.2, Wiley-VCH, 2003,”

[6] R. Feidenhans'l, “Surface structure determination by x-ray diffraction,” *Surface Science Reports*, vol. 10, no. 3, pp. 105 – 188, 1989.

[7] P. H. Fuoss and S. Brennan, “Surface Sensitive X-ray-Scattering,” *Annual Review of Materials Science*, vol. 20, pp. 365–390, 1990.

[8] M. G. Samant, M. F. Toney, G. L. Borges, L. Blum, and O. R. Melroy, “Grazing-Incidence X-ray-Diffraction of Lead Monolayers at a Silver (111) and Gold (111) Electrode-Electrolyte Interface,” *Journal of Physical Chemistry*, vol. 92, no. 1, pp. 220–225, 1988.

[9] M. G. Samant, M. F. Toney, G. L. Borges, L. Blum, and O. R. Melroy, “Insitu Grazing-Incidence X-ray-Diffraction Study of Electrochemically Deposited Pb

Monolayers on Ag(111)," *Surface Science*, vol. 193, no. 1-2, pp. L29–L36, 1988.

[10] C. A. Lucas, "Surface relaxation at the metal/electrolyte interface," *Electrochimica acta*, vol. 47, no. 19, pp. 3065–3074, 2002.

[11] R. Vogel and H. Baltruschat, "Iodine adlattice on pt(100) observed by {STM}," *Surface Science*, vol. 259, no. 3, pp. L739 – L742, 1991.

[12] C. A. Lucas, N. M. Markovic-acute, and P. N. Ross, "Adsorption of halide anions at the pt(111)-solution interfacestudied by in situ surface x-ray scattering," *Phys. Rev. B*, vol. 55, pp. 7964–7971, 1997.

[13] C. A. Lucas, N. M. Markovic, and P. N. Ross, "Observation of an ordered bromide monolayer at the pt(111)-solution interface by in-situ surface x-ray scattering," *Surface Science*, vol. 340, no. 1-2, pp. L949 – L954, 1995.

[14] N. M. Markovic, C. A. Lucas, H. A. Gasteiger, and P. N. Ross, "Bromide adsorption on pt(100): rotating ring-pt(100) disk electrode and surface x-ray scattering measurements," *Surface Science*, vol. 365, pp. 229–240, 1996.

[15] N. M. Markovic, B. N. Grgur, C. A. Lucas, and P. N. Ross, "Underpotential deposition of lead onto pt(100) in acid solutions: Adsorption isotherms and interface structures," *J. Chem. Soc. Faraday Trans.*, vol. 94, pp. 3373–3379, 1998.

[16] C. A. Lucas, N. M. Markovic, and P. N. Ross, "Underpotential deposition of lead onto pt(001): interface structure and the influence of adsorbed bromide," *Langmuir*, vol. 13, no. 21, pp. 5517–5520, 1997.

[17] N. M. Markovic, B. N. Grgur, C. A. Lucas, and P. N. R. Jr., "Underpotential deposition of lead on pt(111) in the presence of bromide: Rrdpt(111)e and x-ray scattering studies," *Journal of Electroanalytical Chemistry*, vol. 448, no. 2, pp. 183 – 188, 1998.

[18] C. A. Lucas, N. M. Markovic, and P. N. Ross, “Underpotential deposition of cu on pt(001): interface structure and the influence of adsorbed bromide,” *Phys. Rev. B*, vol. 57, pp. 13184–13191, 1998.

[19] N. M. Markovic, B. N. Grgur, C. A. Lucas, and P. N. Ross, “Upd of cu on pt(100): effects of anions on adsorption isotherms and interface structures,” *Electrochimica Acta*, vol. 44, no. 6-7, pp. 1009 – 1017, 1998.

[20] N. M. Markovic, C. A. Lucas, H. A. Gasteiger, and P. N. Ross, “The effects of bromide adsorption on the underpotential deposition of copper at the Pt(111)-solution interface,” in *Solid-Liquid Electrochemical Interfaces*, vol. 656 of *ACS Symposium Series*, pp. 87–105, Amer Chemical Soc, 1997.

[21] C. A. Lucas, N. M. Markovic, I. M. Tidswell, and P. N. Ross, “In situ x-ray scattering study of the pt(111)-solution interface: Ordered anion structures and their influence on copper underpotential deposition,” *Physica B: Condensed Matter*, vol. 221, no. 1-4, pp. 245 – 250, 1996.

[22] N. M. Markovic, H. A. Gasteiger, C. A. Lucas, I. M. Tidswell, and P. N. R. Jr., “The effect of chloride on the underpotential deposition of copper on pt(111): Aes, leed, rrde, and x-ray scattering studies,” *Surface Science*, vol. 335, no. 0, pp. 91 – 100, 1995.

[23] I. M. Tidswell, C. A. Lucas, N. M. Markovic, and P. N. Ross, “Surface-structure determination using anomalous x-ray scattering: Underpotential deposition of copper on pt(111),” *Phys. Rev. B*, vol. 51, pp. 10205–10208, 1995.

[24] C. A. Lucas, N. M. Markovic, and P. N. Ross, “Electrochemical deposition of copper onto pt(111) in the presence of (bi)sulfate anions,” *Phys. Rev. B*, vol. 56, pp. 3651–3654, 1997.

[25] C. A. Lucas, N. M. Markovic, and P. N. Ross, “Structural effects induced by CO adsorption on Pt-bimetallic surfaces,” *Surface Review and Letters*, vol. 6, no. 5, pp. 917–922, 1999.

[26] N. M. Markovi, B. N. Grgur, C. A. Lucas, and P. N. Ross, “Surface chemistry of co on pt(100)bimetallic surfaces: displacement effects,” *Langmuir*, vol. 16, no. 4, pp. 1998–2005, 2000.

[27] N. M. Markovic, C. A. Lucas, V. Climent, V. Stamenkovic, and P. N. Ross, “Surface electrochemistry on an epitaxial palladium film on pt(111): surface microstructure and hydrogen electrode kinetics,” *Surface Science*, vol. 465, no. 12, pp. 103 – 114, 2000.

[28] M. J. Ball, C. A. Lucas, N. M. Markovic, V. Stamenkovic, and P. N. Ross, “From sub-monolayer to multilayer an in situ x-ray diffraction study of the growth of pd films on pt(111),” *Surface Science*, vol. 518, no. 3, pp. 201 – 209, 2002.

[29] M. J. Ball, C. A. Lucas, N. M. Markovic, V. Stamenkovic, and P. N. Ross, “Surface x-ray scattering studies of the growth of pd thin films on the pt(111) electrode surface and the effects of the adsorption of co,” *Surface Science*, vol. 540, no. 2-3, pp. 295 – 302, 2003.

[30] C. A. Lucas, N. M. Markovic, M. Ball, V. Stamenkovic, V. Climent, and P. N. Ross, “Surface structure and relaxation during the oxidation of carbon monoxide on ptpd bimetallic surfaces,” *Surface Science*, vol. 479, no. 1-3, pp. 241 – 246, 2001.

[31] M. Ball, C. A. Lucas, N. M. Markovic, B. M. Murphy, P. Steadman, T. J. Schmidt, V. Stamenkovic, and P. N. Ross, “X-ray scattering studies of irreversibly adsorbed bismuth on the Pt(111) electrode surface,” *Langmuir*, vol. 17, no. 19, pp. 5943–5946, 2001.

[32] N. M. Markovi, B. N. Grgur, C. A. Lucas, and P. N. Ross, "Electrooxidation of co and h2/co mixtures on pt(111) in acid solutions," *The Journal of Physical Chemistry B*, vol. 103, no. 3, pp. 487–495, 1999.

[33] N. M. Markovic, C. A. Lucas, A. Rodes, V. Stamenkovi, and P. N. Ross, "Surface electrochemistry of CO on Pt(111): anion effects," *Surface Science*, vol. 499, no. 2-3, pp. L149–L158, 2002.

[34] N. M. Markovic, B. N. Grgur, C. A. Lucas, and P. N. Ross, "Surface electrochemistry of co on pt(110)-(1 x 2) and pt(110)-(1 x 1) surfaces," *Surface Science*, vol. 384, no. 1-3, pp. L805 – L814, 1997.

[35] N. M. Markovi, B. N. Grgur, C. A. Lucas, and P. N. Ross, "Electrooxidation of co and h2/co mixtures on pt(111) in acid solutions," *The Journal of Physical Chemistry B*, vol. 103, no. 3, pp. 487–495, 1999.

[36] C. A. Lucas, N. M. Markovic, and P. N. Ross, "The adsorption and oxidation of carbon monoxide at the pt(111)/electrolyte interface: atomic structure and surface relaxation," *Surface Science*, vol. 425, no. 1, pp. L381 – L386, 1999.

[37] N. M. Markovi, C. A. Lucas, B. N. Grgur, and P. N. Ross, "Surface electrochemistry of co and h2/co mixtures at pt(100) interface: electrode kinetics and interfacial structures," *The Journal of Physical Chemistry B*, vol. 103, no. 44, pp. 9616–9623, 1999.

[38] C. A. Lucas, P. Thompson, M. Cormack, A. Brownrigg, B. Fowler, D. Strmcnik, V. Stamenkovic, J. Greeley, A. Menzel, H. You, and N. M. Markovic, "Temperature-induced ordering of metal/adsorbate structures at electrochemical interfaces," *Journal of the American Chemical Society*, vol. 131, no. 22, pp. 7654–7661, 2009.

[39] M. E. Gallagher, C. A. Lucas, V. Stamenkovic, N. M. Markovic, and P. N. Ross, "Surface structure and relaxation at the pt3sn(111)/electrolyte interface," *Surface Science*, vol. 544, no. 2-3, pp. L729 – L734, 2003.

[40] D. C. Grahame, “The Electrical Double Layer and the Theory of Electrocapillarity,” *Chemical Reviews*, vol. 41, no. 3, pp. 441–501, 1947.

[41] A. C. Fisher, *Electrode Dynamics.* 1996.

[42] P. Paufler, “Complete online set of International tables for crystallography, Vols. A-G.,” *Acta Crystallographica Section A*, vol. 63, no. 6, p. 483, 2007.

[43] J. Clavilier, R. Faure, G. Guinet, and R. Durand, “Preparation of Mono-Crystalline Pt Microelectrodes and Electrochemical Study of the Plane Surfaces Cut in the Direction of the (111) and (110) Planes,” *Journal of Electroanalytical Chemistry*, vol. 107, no. 1, pp. 205–209, 1980.

[44] N. M. Markovic, H. A. Gasteiger, and P. N. Ross, “Oxygen reduction on platinum low-index single-crystal surfaces in sulfuric acid solution: Rotating ring-pt(hkl) disk studies,” *The Journal of Physical Chemistry*, vol. 99, no. 11, pp. 3411–3415, 1995.

[45] J. Wang, B. M. Ocko, A. J. Davenport, and H. S. Isaacs, “InSitu X-ray-Diffraction and X-ray-Reflectivity Studies of the Au(111) Electrolyte Interface - Reconstruction and Anion Adsorption,” *Physical Review B*, vol. 46, no. 16, pp. 10321–10338, 1992.

[46] I. M. Tidswell, N. M. Markovic, C. A. Lucas, and P. N. Ross, “In-Situ X-ray-Scattering Study of the Au(001) Reconstruction in Alkaline and Acidic Electrolytes,” *Physical Review B*, vol. 47, no. 24, pp. 16542–16553, 1993.

[47] “www.aps.anl.gov/Beamlines/Directory/showbeamline.php.”

[48] “www.certif.com/specmanual/idx.html.”

[49] “www.certif.com/specmanual/fourc4.html.”

[50] W. R. Busing and H. A. Levy, “Angle Calculations for 3- and 4- Circle X-ray and Neutron Diffractometers,” *Acta Crystallographica*, vol. 22, no. Part 4, pp. 457+, 1967.

[51] C. A. Lucas, N. M. Markovic, and P. N. Ross, “Structural effects induced by CO adsorption on Pt-bimetallic surfaces,” *Surface Review and Letters*, vol. 6, no. 5, pp. 917–922, 1999.

[52] H. Song, F. Kim, S. Connor, G. A. Somorjai, and P. Yang, “Pt nanocrystals: Shape control and langmuir-blodgett monolayer formation,” *Journal of Physical Chemistry B*, vol. 109, no. 1, pp. 188–193, 2005.

[53] N. Tian, Z. Zhou, S. Sun, Y. Ding, and L. W. Zhong, “Synthesis of tetrahexahedral platinum nanocrystals with high-index facets and high electro-oxidation activity,” *Science*, vol. 316, no. 5825, pp. 732–735, 2007.

[54] J. X. Wang, N. M. Markovic, and R. R. Adzic, “Kinetic analysis of oxygen reduction on pt(111) in acid solutions: Intrinsic kinetic parameters and anion adsorption effects,” *Journal of Physical Chemistry B*, vol. 108, no. 13, pp. 4127–4133, 2004.

[55] V. Stamenkovic, N. M. Markovic, and P. N. Ross Jr., “Structure-relationships in electrocatalysis: Oxygen reduction and hydrogen oxidation reactions on pt(111) and pt(100) in solutions containing chloride ions,” *Journal of Electroanalytical Chemistry*, vol. 500, no. 1-2, pp. 44–51, 2001.

[56] K. F. Blurton, H. R. Kunz, and D. R. Rutt, “Surface area loss of platinum supported on graphite,” *Electrochimica Acta*, vol. 23, no. 3, pp. 183–190, 1978.

[57] Q. Xu, E. Kreidler, D. O. Wipf, and T. He, “In situ electrochemical stm study of potential-induced coarsening and corrosion of platinum nanocrystals,” *Journal of the Electrochemical Society*, vol. 155, no. 3, pp. B228–B231, 2008.

[58] J. L. Gland, B. A. Sexton, and G. B. Fisher, “Oxygen interactions with the pt(111) surface,” *Surface Science*, vol. 95, no. 2-3, pp. 587–602, 1980.

[59] N. R. Avery, "An EELS and TDS Study of Molecular-Oxygen Desorption and Decomposition on Pt(111)," *Chemical Physics Letters*, vol. 96, no. 3, pp. 371–373, 1983.

[60] B. C. Stipe, M. A. Rezaei, and W. Ho, "Atomistic studies of o2 dissociation on pt(111) induced by photons, electrons, and by heating," *Journal of Chemical Physics*, vol. 107, no. 16, pp. 6443–6447, 1997.

[61] C. T. Campbell, G. Ertl, H. Kuipers, and J. Segner, "A Molecular-beam Study of the Adsorption and Desorption of Oxygen from a Pt(111)Surface," *Surface Science*, vol. 107, no. 1, pp. 220–236, 1981.

[62] J. F. Weaver, J. Chen, and A. L. Gerrard, "Oxidation of pt(1 1 1) by gas-phase oxygen atoms," *Surface Science*, vol. 592, no. 1-3, pp. 83–103, 2005.

[63] C. R. Parkinson, M. Walker, and C. F. McConville, "Reaction of atomic oxygen with a pt(1 1 1) surface: Chemical and structural determination using xps, caiciss and leed," *Surface Science*, vol. 545, no. 1-2, pp. 19–33, 2003.

[64] D. I. Jerdev, J. Kim, M. Batzill, and B. E. Koel, "Evidence for slow oxygen exchange between multiple adsorption sites at high oxygen coverages on pt(111)," *Surface Science*, vol. 498, no. 1-2, pp. L91–L96, 2002.

[65] D. H. Parker, M. E. Bartram, and B. E. Koel, "Study of High Coverages of Atomic Oxygen on the Pt(111) Surface," *Surface Science*, vol. 217, no. 3, pp. 489–510, 1989.

[66] N. Saliba, Y. L. Tsai, C. Panja, and B. E. Koel, "Oxidation of Pt(111) by ozone (O-3) under UHV conditions," *Surface Science*, vol. 419, no. 2-3, pp. 79–88, 1999.

[67] D. Friebel, D. J. Miller, C. P. O'Grady, T. Anniyev, J. Bargar, U. Bergmann, H. Ogasawara, K. T. Wikfeldt, L. G. M. Pettersson, and A. Nilsson, "In situ x-ray probing reveals fingerprints of surface platinum oxide," *Physical Chemistry Chemical Physics*, vol. 13, no. 1, pp. 262–266, 2011.

[68] H. You, D. J. Zurawski, Z. Nagy, and R. M. Yonco, "In-situ x-ray reflectivity study of incipient oxidation of pt(111) surface in electrolyte solutions," *The Journal of chemical physics*, vol. 100, no. 6, pp. 4699–4702, 1994.

[69] M. Matsumoto, T. Miyazaki, and H. Imai, "Oxygen-enhanced dissolution of platinum in acidic electrochemical environments," *Journal of Physical Chemistry C*, vol. 115, no. 22, pp. 11163–11169, 2011.

[70] C. Ellinger, A. Stierle, I. K. Robinson, A. Nefedov, and H. Dosch, "Atmospheric pressure oxidation of pt(111)," *Journal of Physics Condensed Matter*, vol. 20, no. 18, 2008.

[71] L. A. Kibler, A. Cuesta, M. Kleinert, and D. M. Kolb, "In-situ STM characterisation of the surface morphology of platinum single crystal electrodes as a function of their preparation," *Journal of Electroanalytical Chemistry*, vol. 484, no. 1, pp. 73–82, 2000.

[72] J. M. Hawkins, J. F. Weaver, and A. Asthagiri, "Density functional theory study of the initial oxidation of the pt(111) surface," *Phys. Rev. B*, vol. 79, pp. 125 – 134, 2009.

[73] C. Wang, H. Daimon, Y. Lee, J. Kim, and S. Sun, "Synthesis of monodisperse pt nanocubes and their enhanced catalysis for oxygen reduction," *Journal of the American Chemical Society*, vol. 129, no. 22, pp. 6974–6975, 2007.

[74] M. L. Sattler and P. N. Ross, "The surface structure of pt crystallites supported on carbon black," *Ultramicroscopy*, vol. 20, no. 1-2, pp. 21–28, 1986.

[75] K. Kinoshita, "Particle-Size Effects for Oxygen Reduction on Highly Dispersed Platinum in Acid Electrolytes," *Journal of the Electrochemical Society*, vol. 137, no. 3, pp. 845–848, 1990.

[76] G. L. Kellogg, "Temperature dependence of surface self-diffusion on pt(001)," *Surface Science*, vol. 246, no. 1-3, pp. 31 – 36, 1991.

[77] G. A. Benesh and L. S. G. Liyanage, “The surface electronic structure of oxygen on pt(001)(1 x 1),” *Surface Science*, vol. 261, no. 1-3, pp. 207 – 216, 1992.

[78] R. Lewis and R. Gomer, “Adsorption of oxygen on platinum,” *Surface Science*, vol. 1-2, no. 2, pp. 157 – 176, 1968.

[79] K. Kuhnke, K. Kern, and G. Comsa, “Preparation and thermal stability of the clean metastable pt(100)(1 x 1) surface: a thermal energy helium scattering study,” *Surface Science*, vol. 343, no. 1-2, pp. 44 – 52, 1995.

[80] A. Baraldi, E. Vesselli, L. Bianchettin, G. Comelli, S. Lizzit, L. Petaccia, S. de Gironcoli, A. Locatelli, T. O. Mentes, L. Aballe, J. Weissenrieder, and J. N. Andersen, “The (11) hexagonal structural transition on pt(100) studied by high-energy resolution core level photoemission.,” *Journal of Chemical Physics*, vol. 127, no. 16, p. 164702, 2007.

[81] N. M. Markovic, H. A. Gasteiger, and P. N. Ross, “Oxygen reduction on platinum low-index single-crystal surfaces in sulfuric acid solution: Rotating ring-pt(hkl) disk studies,” *The Journal of Physical Chemistry*, vol. 99, no. 11, pp. 3411–3415, 1995.

[82] H. A. and Gasteiger and P. N. Ross, “Oxygen reduction on platinum low-index single-crystal surfaces in alkaline solution: rotating ring diskpt(hkl) studies,” *The Journal of Physical Chemistry*, vol. 100, no. 16, pp. 6715–6721, 1996.

[83] D. Strmcnik, D. Tripkovic, D. van der Vliet, V. Stamenkovic, and N. M. Markovic, “Adsorption of hydrogen on pt(111) and pt(100) surfaces and its role in the hor,” *Electrochemistry Communications*, vol. 10, no. 10, pp. 1602 – 1605, 2008.

[84] F. E. Kadiri, R. Faure, and R. Durand, “Electrochemical reduction of molecular oxygen on platinum single crystals,” *Journal of Electroanalytical Chemistry and Interfacial Electrochemistry*, vol. 301, no. 12, pp. 177 – 188, 1991.

[85] D. F. van der Vliet and M. T. M. Koper, “Electrochemistry of pt (100) in alkaline media: A voltammetric study,” *Surface Science*, vol. 604, no. 21-22, pp. 1912 – 1918, 2010.

[86] F. T. Wagner and P. N. R. Jr., “Leed spot profile analysis of the structure of electrochemically treated pt(100) and pt(111) surfaces,” *Surface Science*, vol. 160, no. 1, pp. 305 – 330, 1985.

[87] M. S. Zei and G. Ertl, “On the structural transformation of the reconstructed pt(100) in electrolyte solutions,” *Surface Science*, vol. 442, no. 1, pp. 19 – 26, 1999.

[88] F. McBride, G. R. Darling, K. Pussi, C. A. Lucas, Y. Gruender, M. Darlington, A. Brownrigg, and A. Hodgson, “The Influence of Water and Hydroxyl on a Bimetallic (root 3 x root 3)R30 degrees Sn/Pt Surface Alloy,” *JOURNAL OF PHYSICAL CHEMISTRY C*, vol. 117, pp. 4032–4039, FEB 28 2013.

[89] V. R. Stamenkovic, B. Fowler, B. S. Mun, G. Wang, P. N. Ross, C. A. Lucas, and N. M. Markovic, “Improved oxygen reduction activity on Pt3Ni(111) via increased surface site availability,” *Science*, vol. 315, no. 5811, pp. 493–497, 2007.

[90] V. Stamenkovic, T. J. Schmidt, P. N. Ross, and N. M. Markovic, “Surface composition effects in electrocatalysis: Kinetics of oxygen reduction on well-defined Pt3Ni and Pt3Co alloy surfaces,” *Journal of Physical Chemistry B*, vol. 106, no. 46, pp. 11970–11979, 2002.

[91] V. Stamenkovic, T. J. Schmidt, P. N. Ross, and N. M. Markovic, “Surface segregation effects in electrocatalysis: kinetics of oxygen reduction reaction on polycrystalline pt3ni alloy surfaces,” *Journal of Electroanalytical Chemistry*, vol. 554-555, no. 0, pp. 191 – 199, 2003.

[92] V. Stamenkovic, T. J. Schmidt, P. N. Ross, and N. M. Markovic, “Surface segregation effects in electrocatalysis: kinetics of oxygen reduction reaction on

polycrystalline pt3ni alloy surfaces," *Journal of Electroanalytical Chemistry*, vol. 554 - 555, no. 0, pp. 191 – 199, 2003.

[93] B. S. Mun, M. Watanabe, M. Rossi, V. Stamenkovic, N. M. Markovic, and P. N. Ross, Jr., "The study of surface segregation, structure, and valence band density of states of Pt3Ni(100), (110), and (111) crystals," *Surface Review and Letters*, vol. 13, pp. 697–702, OCT 2006.

[94] V. Stamenkovic, T. J. Schmidt, P. N. Ross, and N. M. Markovic, "Surface segregation effects in electrocatalysis: kinetics of oxygen reduction reaction on polycrystalline pt3ni alloy surfaces," *Journal of Electroanalytical Chemistry*, vol. 554 - 555, no. 0, pp. 191 – 199, 2003.

[95] J. Zhang, H. Yang, J. Fang, and S. Zou, "Synthesis and Oxygen Reduction Activity of Shape-Controlled Pt3Ni Nanopolyhedra," *Nano Letters*, vol. 10, no. 2, pp. 638–644, 2010.

[96] J. Wu, J. Zhang, Z. Peng, S. Yang, F. T. Wagner, and H. Yang, "Truncated Octahedral Pt3Ni Oxygen Reduction Reaction Electrocatalysts," *Journal of the American Chemical Society*, vol. 132, no. 14, pp. 4984+, 2010.

[97] C. Guemeci, Z. Li, D. J. Casadonte, Jr., and C. Korzeniewski, "Pt-Ni Nanoparticles for Oxygen Reduction Prepared by a Sonochemical Method," *Journal of the Electrochemical Society*, vol. 159, no. 3, pp. F35–F41, 2012.

[98] J. Zhang, Z. Luo, Z. Quan, Y. Wang, A. Kumbhar, D. M. Smilgies, and J. Fang, "Low Packing Density Self-Assembled Superstructure of Octahedral Pt3Ni Nanocrystals," *Nano Letters*, vol. 11, no. 7, pp. 2912–2918, 2011.

[99] From unpublished work by Nenad Markovic's group at the Materials Science Division of the Argon National Lab, Chicago.